Programmable stimuli-responsive zwitterionic hydrogels for soft robotic applications

by

Negin Bouzari

A thesis

presented to the University of Waterloo

in fulfillment of the

thesis requirement for the degree of

Master of Applied Science

in

Chemical Engineering

Waterloo, Ontario, Canada, 2023

Author’s Declaration

I hereby declare that I am the sole author of this thesis. This is a true copy of the thesis, including any required final revisions, as accepted by my examiners.

I understand that my thesis may be made electronically available to the public.

Abstract

As a prominent class of actuators, stimuli-responsive hydrogels have attracted significant interest in the soft robotics community for biomedical applications. Key features of hydrogels, including high water content and similar physicochemical properties to that of tissues, make them excellent materials to be used in a wide range of biomedical applications such as drug delivery, and tissue engineering. Particularly, hydrogels with stimuli-responsiveness, self-healing, shape-morphing, low cytotoxicity, and tunable physiochemical properties can be used as functional building blocks in biomedical devices and robots, enabling minimally invasive medical procedures.

Introducing programmability to the shape-morphing of hydrogels opens up new opportunities, especially, in the fabrication of remotely controllable biomedical robots. In this work, we synthesized responsive hydrogel nanocomposites and bilayers with preprogrammed shape transformations that enable desirable robotic functionalities. For this, we used zwitterionic/acrylate chemistries that impart self-healing, stimuli-responsiveness, and biocompatibility to our hydrogel system. Introducing heterogenous physiochemical properties, at the microscale, and employing a multilayering approach, at the macroscale, rendered differential swelling to the hydrogels, which were then employed as a programming strategy to facilitate 2D-to-3D shape-morphing of the hydrogel upon exposure to environmental cues.

As a proof-of-concept, we demonstrated tethered and untethered soft robotic functionalities, such as actuation, magnetic locomotion, and targeted transport of soft and light cargo in confined and flooded media. Our future direction includes developing novel bio-inks from this hydrogel system for extrusion additive manufacturing given their excellent tunability of mechanical properties coupled with the shear-thinning rheology of the hydrogel. We believe that the proposed hydrogel formulation will expand the portfolio of functional materials for fabricating miniaturized soft actuators for biomedical applications.

Acknowledgments

I am truly grateful to my supervisor, Prof. Hamed Shahsavan, for the opportunity he gave me and for his endless support and patience. His mentorship has taught me not only valuable research skills but also what it means to be a compassionate and inspiring mentor. I feel incredibly fortunate to have him as my supervisor and mentor. He has had a profound impact on my life, and I will always be grateful for the opportunity he has given me and the support he has provided along the way. I have much to learn from him, and I am deeply appreciative of his guidance.

I would also like to thank Dr. Rasool Nasseri for his valuable guidance and support throughout my project. His expertise and encouragement have been instrumental in my progress. I am grateful to Professors Xiaowu (Shirley) Tang, Tizazu H. Mekonnen, and Amirreza Aghakhani for their invaluable contributions to my research project. Professor Tang's group provided crucial assistance with experimental biocompatibility and cell viability tests, which were essential components of my project. With Professor Mekonnen's support, I gained access to his lab and equipment, enabling me to conduct experiments and collect data that would have been otherwise unattainable. Lastly, Professor Aghakhani's simulations have expanded my understanding of the theoretical aspects of this research. Without their guidance and support, this project would not have been possible. I am deeply appreciative of their contributions and fortunate to have worked with such remarkable individuals. I am deeply grateful for the financial support provided by Dr. Kaveh Sarikhani and his company.

I am grateful to all my friends and colleagues for their invaluable help, and I want to thank Natalie especially for her assistance with proofreading and for the times we spent over coffee. Her friendly and welcoming nature made me feel at home in Canada. I am lucky to have her as a friend and colleague. Additionally, I am deeply thankful for Junting's enormous help with experiments and data collection.

Lastly, but most importantly, I want to express my heartfelt gratitude to my beloved family. Their endless love and support have been the driving force behind my success, and I owe everything to them. They have been my guiding light, my source of strength, and my biggest cheerleaders throughout my journey. To my dear mom and dad, and to my wonderful sister Negar and my brother-in-law Majd, who is like a brother to me, you have been my pillars of support, and I cannot thank you enough for all that you have done for me. Your love and encouragement have been the greatest gift I could ever ask for.

Dedication

I humbly offer this thesis to my beloved family, who are the color of my life. Thank you for being my constant source of inspiration and for instilling in me the values of hard work, perseverance, and determination.

Table of Contents

List of Figures

List of Tables

Chapter 1
Introduction

Traditional robots are automated machines that are capable of performing particular tasks with a high degree of precision and are typically made of rigid and bulky components, which limits safe human-robot interactions. In the past two decades, the emergence of soft robots has opened up new possibilities for performing delicate tasks that require safe interaction between humans and robots. Developing small-scale soft robots is a growing research direction that aims to shrink the scale of soft robots for applications in confined and tiny environments. These small-scale robots, naturally, show great promise for minimally-invasive medical interventions, such as biopsies, targeted drug delivery, and single-cell transport, particularly in confined environments.[1,2] To develop small-scale robots that could perform predictable functions in tiny environments wirelessly and in a predictable fashion, using materials with onboard sensing, actuation, and processing abilities becomes crucial.[3–6]

Among the material choices for fabricating soft robots, hydrogel actuators have become a popular choice due to their high water content and physicochemical properties that closely resemble biological tissues.[7–13] At the molecular level, hydrogel actuators exhibit a change in their spatial conformation in response to external stimuli such as heat, light, pH, and ionic concentration. These changes result in the macroscopic deformation of the hydrogel material.[7,8,11,14–23], which are typically isotropic. However, effective operation in many real-world scenarios, such as soft robotics, requires predictable anisotropic shape transformations that can be programmed into the hydrogel system. Introducing microstructural and macrostructural heterogeneity are two common techniques to elicit anisotropic shape change, which can be used to achieve programmability.[6,24,25][7,14,16–18,20,21]. For example, local internal stresses generated from differential swelling of hydrogels can result in anisotropic shape transformations, including but not limited to twisting, bending, or folding.[8,26]

Moreover, to unlock the potential of soft robots for various biomedical applications, they need to possess biocompatible properties, such as cell viability, preventing fouling, and eliciting a non-immunogenic response. These characteristics are essential to ensure the safe interaction of soft robots with biological tissues and systems, paving the way for their use in advanced medical procedures and therapies.[27] Creating a soft robot with all the aforementioned functionalities is a challenging task that has been only scarcely explored in literature so far.

Zwitterionic hydrogels are known for their superior anti-fouling and biocompatibility properties.[28,29] Due to their super hydrophilicity, overall neutral charge, and presence of H-bond-accepting functional groups, zwitterionic hydrogels exhibit minimal protein adsorption and cell adhesion, making them highly biocompatible.[30] These properties can potentially reduce the risk of immune responses and adverse reactions in the body, making them an ideal choice for biomedical applications.[31] In addition, the supramolecular chemistry of the zwitterionic component enables the dynamic healing of chains upon scission, thus providing new avenues to develop intrinsic self-healing materials.[18,28] To the best of our knowledge, this class of hydrogel has never been used in stimuli-triggered shape-morphing materials, especially for soft robotic applications.

In this work, we synthesized a novel hydrogel copolymer based on zwitterionic/acrylate chemistry, which offers a host of opportunities for small-scale soft robotics. In chapter 4, we show that microstructural anisotropy can be introduced by synthesizing cellulose nanocrystal (CNC)-based hydrogel nanocomposites, where the alignment of CNC enables hydrogels to undergo programmable stimuli-responsive shape transformation. In chapter 5, we showcase another programming strategy, by which utilizing a cut-and-paste method, enabled by the self-healing properties of the hydrogel, allows for the attachment of hydrogel layers to create programmable bilayer structures. We believe our proposed hydrogel system expands the portfolio of materials for fabricating soft actuators for small-scale biomedical robotics.

Chapter 2
Literature Review

2.1 Soft Materials in Robotic Applications

The field of robotics has emerged as an exciting and rapidly evolving research direction that has significant potential to improve the quality of human life. Particularly, using robots in healthcare applications has garnered considerable attention in the past four decades. The use of robots in healthcare applications provides increased precision during medical procedures and can significantly enhance patient care.[32–36] One of the primary concerns with traditional robots is the use of rigid materials to create robotic components, such as links and joints. Using rigid components in fabricating robots raises safety risks in interactions between humans and robots, such as potential damage to human tissues during robotic operations.[37–41]

To address this concern, soft robotics has emerged as a promising alternative to traditional rigid robotics.[42,43] Soft robotics employs compliant and flexible materials, with similar elastic modulus to the soft tissues found in biological systems, and as such offers safer human-robot interactions.[44,45] In this regard, using compliant materials with a high degree of flexibility as well as onboard sensing, actuation, and processing abilities has become increasingly important for developing soft robots.[46–48] Moreover, the development of small-scale soft robots has opened up new possibilities in minimally-invasive medical interventions, including biopsy, single-cell transport, and drug delivery due to the ability of soft robots to navigate through narrow pathways in the body with minimal damage to healthy tissues.[49–51]

Below, we have listed five prominent classes of soft materials that have been used for designing adaptive robotic functions, namely, dielectric elastomers, shape-memory polymers, liquid crystal elastomers, magnetoactive elastomers, and hydrogels as reported in the literature (**Figure 2-1**).[52]

Dielectric elastomers (DEs) have been developed as electroactive artificial muscles for use in soft robotic systems due to their ability to generate large strains when exposed to external electric fields. Electric fields applied to DEs result in area expansion and thickness shrinkage in the elastomer, allowing for the direct conversion of electric energy into mechanical energy, making them a compliant material choice for designing soft capacitors and artificial muscles.[53–55] The fabrication of DEs with desirable properties, such as low driving electric field, high actuation strain, and repeatable and

programmable actuation, requires in some cases intricate modification of the material's and electrodes' chemistry and mechanical properties. These modifications are necessary to achieve optimal performance and ensure the reliability of the DEs in soft robotic systems.[56–66]

Shape memory polymers (SMPs) are another class of soft materials in robotic applications that can recover their initial shape after being deformed upon exposure to external stimuli.[52] For example, a transitory shape can be induced to temperature-sensitive SMPs above critical temperatures and fixed by cooling. Recovery to the initial shape can then be achieved by elevating the temperature beyond that critical temperature. [67–71] Overcoming hysteresis and slow transition speeds is necessary to fabricate SMPs with high robotic efficiency and low response time.[72]

Liquid crystal elastomers (LCEs) are used in soft robotics thanks to their localized thermal, photothermal, and photochemical actuation abilities. LCEs undergo large deformations when exposed to external stimuli due to the disruption of liquid crystal mesogens' order at the micro-scale, leading to macro-scale shape changes.[73–85] LCEs are particularly suitable for thermal actuation, and researchers have explored the use of photothermal converters, such as dyes, to control the mode of actuation.[52,86,87] However, to expand the use of thermal LCEs in a broader range of robotic applications, improving low energy conversion efficiency is necessary. Additionally, improving the efficiency of actuators in aquatic environments seems to be an important research direction.[58,74,83,88–94]

Magnetoactive elastomers represent another class of materials for robotic applications, due to their ability to deform, navigate, and perform specific tasks under the influence of external magnetic fields. One of the key advantages of these materials is their safe and compliant navigation within the human body, which makes them highly suited for biomedical applications.[52,95,96] Several types of magnetic materials can be used to develop magnetically responsive soft devices, including ferromagnetic, paramagnetic, and superparamagnetic materials. These materials can partially or completely retain their magnetic moments after the magnetic field is removed, enabling them to be actuated using magnetic fields.[97–101] Inducing non-uniform magnetization and non-homogeneous encoding of magnetic particles into the soft base materials are the commonly-used approaches to control the anisotropic magnetic actuation. Despite the potential advantages of magnetic soft robots, there are still challenges to be overcome in terms of fabrication and actuation. For instance, it can be difficult to achieve high levels of non-uniformity in the magnetic field, and the energy required to actuate these materials can be high.[24,102]

Hydrogels represent a class of soft materials that possess properties suitable for use in soft robotics. Thanks to their high water content, hydrogels exhibit softness (with an elastic modulus in the range of 1-100 kPa) that closely resembles that of biological tissues.[103–109] Stimuli-responsive hydrogels have been widely utilized in the development of soft robots.[110–116] These hydrogels can be categorized into two subcategories based on their actuation mode in response to external stimuli: active and passive responsive hydrogels.[52] Active hydrogels are composed of a network of polymer chains that is intrinsically responsive to one or more external physical, chemical, or biological stimuli.[115] In contrast, passive responsive hydrogels are composed of a polymer network incorporated with elements, such as ions, nanofillers, or conductive additives, which respond to external cues.[112,117–123] The interesting properties of hydrogels, including ease of synthesis and modification, reasonable response time, and functional capabilities in aquatic environments, make them a highly desirable material for a wide range of soft robotic applications. In this chapter, we will delve into the exceptional properties of hydrogels that make them the ideal material for soft robotics. Specifically, we will explore two crucial characteristics of hydrogels - self-healing and programmability - that are essential for their effective use in soft robotics.

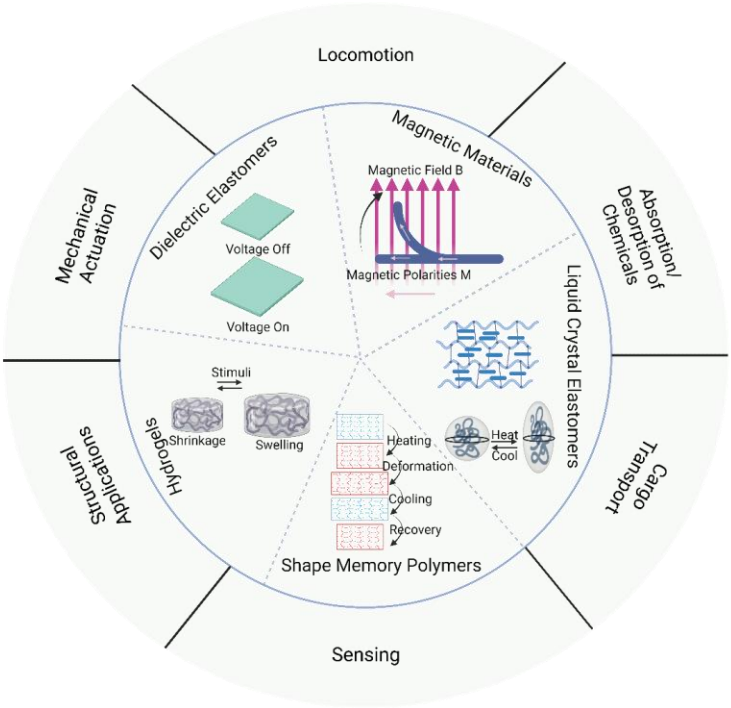

Figure 2-1. Overview of typical stimuli-responsive materials and their applications for soft robotics.

2.2 Responsive Hydrogels and Composites

Hydrogel actuators offer numerous opportunities for designing bioinspired soft robots,[7,10–12,124] and can be used in various applications such as drug delivery, tissue engineering, and artificial muscles due to their high water content and structural similarity to biological tissues.[8,20] Biocompatible and programmable stimuli-responsive self-healing hydrogels possess a combination of characteristics such as low cytotoxicity, tunable physiochemical properties, and predictable shape-changing properties, that make them an ideal material choice for soft robotics.[125] This class of materials undergo spatial swelling or shrinking in response to external cues, which results in macro-scale shape changes.[12] Stimuli responsiveness is a crucial requirement of hydrogels for soft robotic applications, as it enables actuation upon exposure to one or, in some cases, several external stimuli, such as temperature, pH, light, and ion concentration (**Figure 2-2**).[24,126,127]

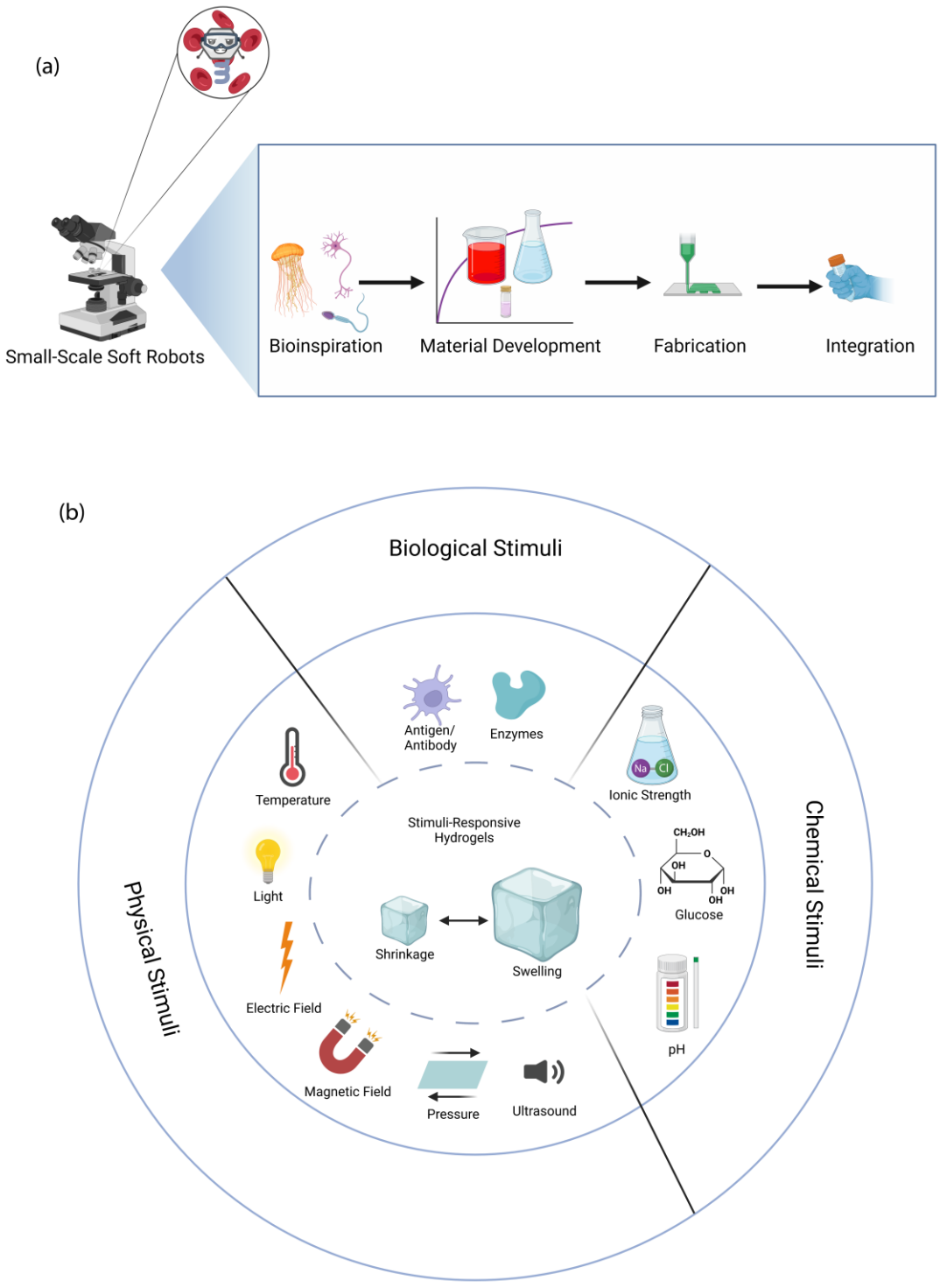

Figure 2-2. a) Schematic representation of fabricating bioinspired small-scale soft robots. b) Schematic illustration of different smart/stimuli-responsive hydrogels.

Changing the chemical composition and morphology of hydrogels, as well as fabricating nanocomposite hydrogels, are commonly reported approaches for fine-tuning the physiochemical and mechanical properties of these materials.[128–131] Copolymerization is a powerful tool for controlling the chemical, physical, and mechanical properties, achieved by changing the type and ratio of the monomers used.[132,133] While copolymerization is an advantageous approach, finding compatible monomers and selecting the appropriate composition can be time-consuming. Furthermore, adjusting the ratio of the monomers alone may not result in significant changes in the physiochemical properties. Therefore, another effective strategy for controlling the properties of hydrogels is to incorporate additional components, such as nanoparticles, to modify their properties.[134,135] Cellulose nanocrystals (CNCs) have gained significant attention as reinforcing agents for hydrogels. CNCs are abundant, bio-sourced, and biodegradable, which offer sustainable and environmentally friendly solutions for developing many soft commodities.[136–139] (**Figure 2-3**)

We believe that incorporating CNCs into stimuli-responsive hydrogels has great potential for developing high-performance soft robotic devices with improved mechanical properties. The incorporation of CNCs into hydrogels can enhance the mechanical strength, stiffness, and toughness of hydrogels while maintaining their high water content and biocompatibility.[140–142] For instance, CNCs are incorporated into a range of hydrogels, such as polyethylene glycol methacrylate (POEGMA), polyvinyl alcohol (PVA), and Polyacrylamide (PAAm), to enhance their mechanical properties.[143–146] The modified hydrogel nanocomposite exhibited up to a 35-fold increase in the storage modulus, faster water uptake, and slower degradation than the pure POEGMA hydrogel.[147]

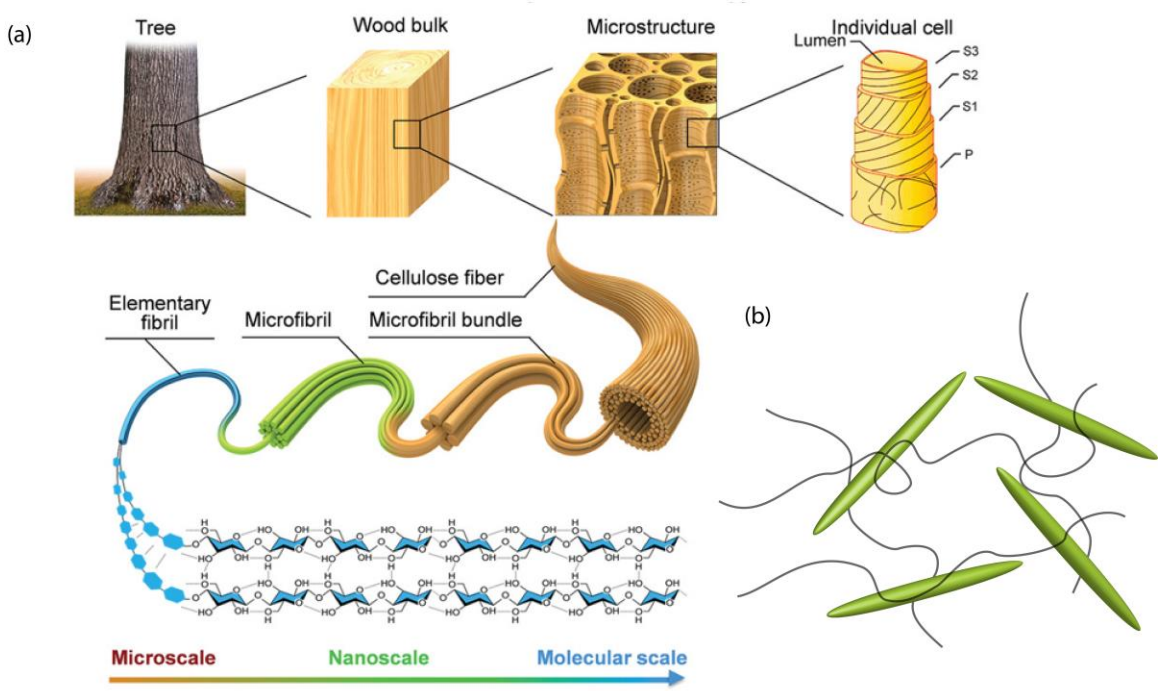

Figure 2-3. a) Schematic representation of the CNC fabrication process. Reproduced with permission.[148] Copyright 2023, Wiley-VCH. b) Schematic representation of the anisotropic CNCs in the hydrogel network.

In addition to possessing desirable physicochemical properties and being able to respond to external stimuli, the development of soft robotic hydrogels for use in biomedical applications necessitates that the hydrogel material be biocompatible. This means that the material should possess cell viability, resist fouling (i.e., the accumulation of unwanted biomolecules on a surface), and should be non-immunogenic, meaning that it should not provoke an immune response that could lead to rejection in the body.[149,150] Polyethylene glycol (PEG)-based materials have been widely used for developing soft robots in biomedical applications due to their biocompatibility. However, recent studies have demonstrated that zwitterionic chemistry (**Figure 2-4**)[151] exhibits even better biocompatibility than PEG-based materials (**Figure 2-5**).[31,152] For instance, sulfobetaine methacrylate is a zwitterionic compound that contains quaternary ammonium and sulfonate side groups. This material has a higher hydration capacity and a lower hydration free energy (-404 to -519 $\frac{kJ}{mol}$) compared to PEG, which has a hydration free energy of -182 ($\frac{kJ}{mol}$). This feature leads to the formation of a dense hydration layer

when exposed to a wet medium. Since most proteins and cells are inherently hydrophobic, they tend to resist adhering to sulfobetaine-based hydrogels, making them an excellent choice for biomedical applications.[153]

Hen et al. confirmed the excellent biocompatibility of sulfobetaine-based hydrogels by co-culturing the hydrogels with cells and bacteria for multiple days. According to their results, the hydrogel resistsed the adhesion of bacteria, cells, and proteins significantly, demonstrating its potential as an anti-fouling material for in-vivo applications. Cell-culturing in the leaching solution of hydrogels also showed excellent cell viability after at least three days, confirming the non-cytotoxicity of the studied hydrogels.[154] Cabanach et al. also demonstrated the biocompatibility of sulfobetaine methacrylate for in-vivo biomedical applications in another study.[31]

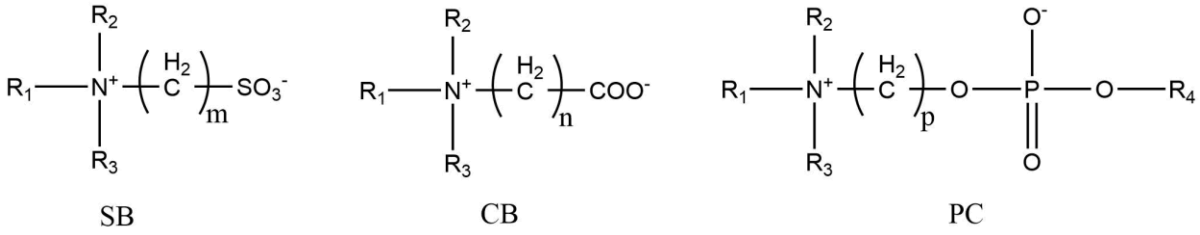

Figure 2-4. Zwitterionic polymers can be classified into sulfobetaine (SB), carboxybetaine (CB), phosphorylcholine (PC) according to anions. Typical cations are quaternized ammonium.

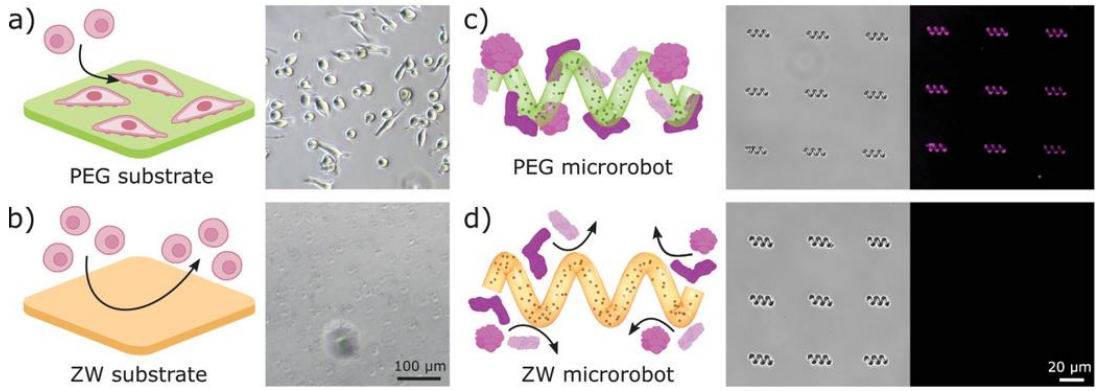

Figure 2-5. Anti-biofouling microrobots. a,b) Cell adhesion on PEG (a) and sulfobetaine-based (b) substrates after 48 hours of culture and rinsing. PEG substrates showed attached cells after rinsing, while cells on ZW substrates were easily washed away. c,d) Protein adsorption on PEG microrobots (c) and sulfobetaine-based microrobots (d). Zwitterionic microrobots did not show protein adsorption on their surface (no fluorescent signal). Reproduced with permission.[31] Copyright 2023, Wiley-VCH.

2.3 Self-Healing Hydrogels

Self-healing hydrogels have been a subject of growing research interest in soft robotic systems, as they offer the potential to repair the damage to the hydrogel in unpredictable environments.[155–158] These hydrogels can be broadly classified into two categories: extrinsic and intrinsic self-healing systems.[159–164] In extrinsic systems, a healing agent is embedded within the material, and upon rupture of the structure, it is released and transferred to the damaged part via osmotic pressure and capillary effect.[165] In intrinsic self-healing systems, dynamic healing of the ruptured chains is promoted by either covalent or non-covalent interactions (**Figure 2-6**).[166–170] These interactions can be triggered by specific external stimuli, such as temperature, pH, and oxidants, or by physical interactions, such as the electrostatic interactions between oppositely charged moieties in the building blocks.

In dynamic covalent systems, the self-healing ability is influenced by the efficiency of bond cleavage and reformation under specific external conditions, including temperature, pH, redox, and oxidants. Disulfide and diselenide bonds are the main focus of research on covalent dynamic systems.[171–177] Non-covalent healing systems, including host-guest interactions, metal coordination, electrostatic interactions, and hydrogen bonding, spontaneously repair the structural damage through physical interactions.[178–183] These self-healing mechanisms may act independently or in combination with each other.[156,184,185] Overall, the development of self-healing hydrogels, particularly intrinsic self-healing hydrogels, offers a promising approach to creating soft robots that can withstand unpredictable environments while maintaining their structural integrity.

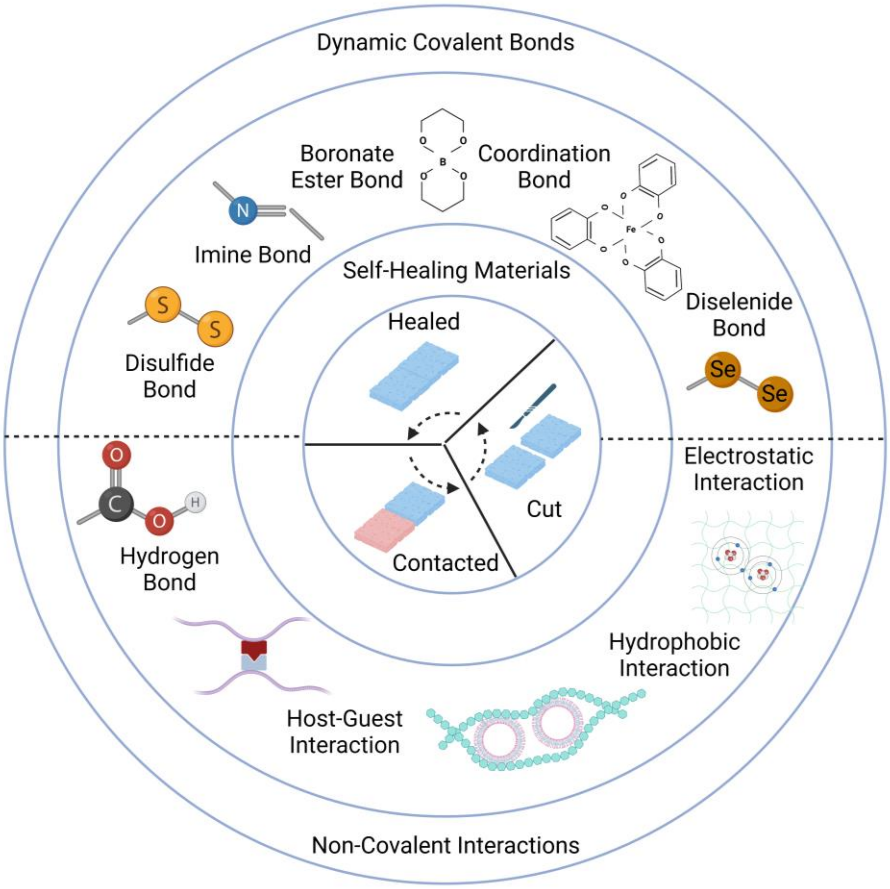

Figure 2-6. Illustration of intrinsic self-healing systems based on different dynamic covalent bonds or/and non-covalent interactions.

The presence of electrostatic interactions between zwitterions provides such hydrogel systems with self-healing abilities due to the physical interactions between oppositely charged building blocks (**Figure 2-7**).[186–189] Hydrogen bond-donating/accepting hydrogels are another type of non-covalent dynamic healable system that use the reversible formation and cleavage of hydrogen bonds to promote self-healing.[190–192] These systems have been found to exhibit high healing efficiencies and rapid healing rates, making them promising candidates for soft robotic applications.[193–198] Incorporating physical interactions has emerged as a straightforward and efficient method for introducing intrinsic self-healing capabilities in soft robotic devices. We believe that these properties facilitate the use of a cut-and-paste technique for joining hydrogel pieces to fabricate functional materials such as end-effectors, which will be further elaborated on in subsequent sections.

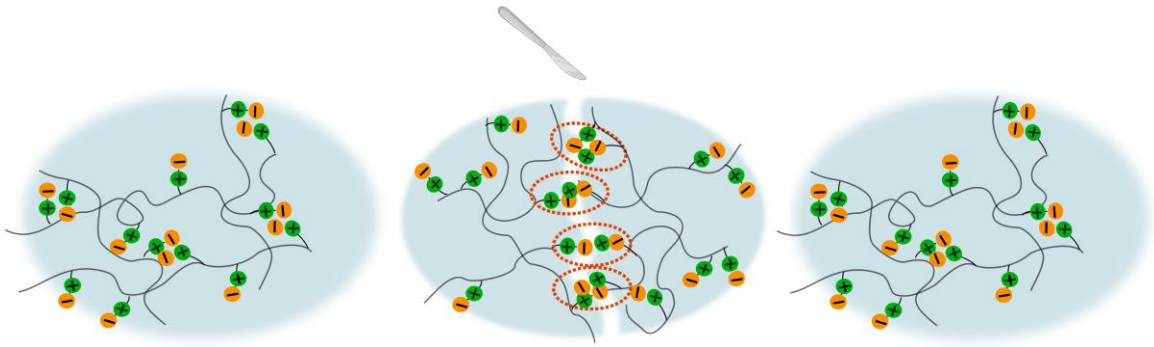

Figure 2-7. Schematic representation of self-healing by the reformation of ionic associations.

2.4 Programmable Actuation of Hydrogels

As discussed in previous sections, stimuli-responsive hydrogels have attracted considerable attention in recent years due to their responsiveness to various external stimuli, including temperature, pH, light, and electric or magnetic fields. These materials have found widespread use in various applications, including sensors, drug delivery systems, and tissue engineering, among others.[199–204] The use of stimuli-responsive hydrogels as actuators in soft robotics requires anisotropic and predictable shape change profiles, such as bending and twisting, [156,205] which allows the device to perform a variety of functions such as locomotion and gripping/releasing. Introducing heterogeneity into the structure of hydrogels results in differential swelling.[17,18,206–211] As a result of this differential swelling, local internal stresses arise, leading to anisotropic shape transformations such as twisting, bending, or folding.[209,211]

The structural heterogeneity can be induced at the micro-scale or macro-scale.[212–218] Microstructural anisotropy can be introduced by the directed assembly of nanofillers, void channels, or liquid crystal domains in pre-polymerized hydrogel precursors, followed by their in-situ polymerization.[17,18,206,207,219,220] Conventional methods for the directional assembly of asymmetric nanofillers, void channels, or the creation of aligned liquid crystalline domains in hydrogels include unidirectional shear flow, exposure to external magnetic and electric fields, and directional freezing (**Figure 2-8**).[219] An outstanding example is the work by Gevorkian et al. who reported shape-change programming of anisotropic CNC-modified gelatin methacryloyl hydrogels, where the anisotropy was induced by applying unidirectional shear flow during fabrication. Obtaining complex morphing profiles

was achieved by changing the CNC orientation and patterning the hydrogel device with the regions of directional- and randomly-oriented strips.[219]

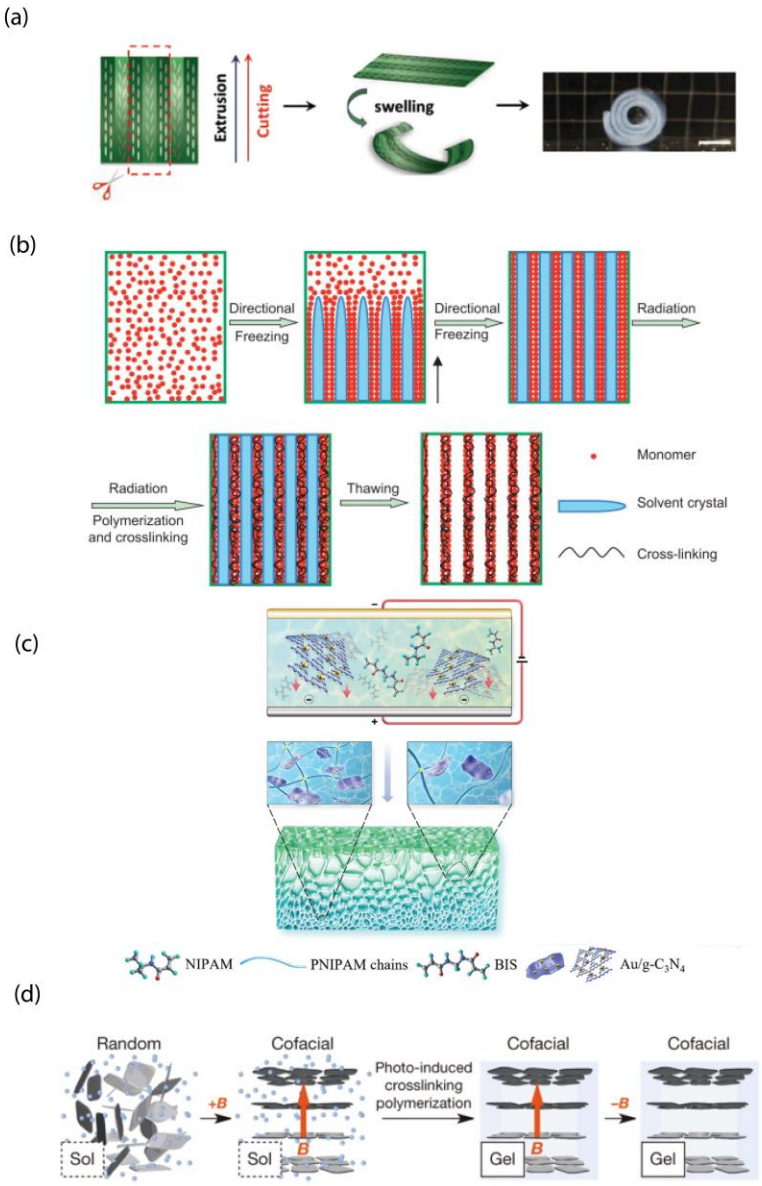

Figure 2-8. a) Relationship between the swelling-induced hydrogel shape and CNC orientation with respect to the long axis of the sheet. Reproduced with permission.[219] Copyright 2023, Wiley-VCH. b) Directional orientation of the hydrogel structure using the directional freezing method. Reproduced with permission.[221] Copyright 2023, Elsevier. c) Electric field-induced alignment of void channels inside the structure of the hydrogel. Reproduced with permission.[222] Copyright 2023, Wiley-VCH. d) Magnetic field-induced structural anisotropy of hydrogels containing co-facially oriented titanium nanosheets. Reproduced with permission.[223] Copyright 2023, Nature Publishing Group.

Another commonly-used method in fabricating programmable hydrogel actuators is utilizing multilayer structures to induce macrostructural anisotropy (**Figure 2-9**).[215] This approach involves integrating several hydrogel layers with different physicochemical and swelling properties to create a single construct. The asymmetrical response of each layer upon exposure to the stimuli results in various modes of shape-change, such as expansion and shrinkage, followed by bending and twisting, which enables the hydrogel to perform a range of potential functions such as gripping and cargo transport.[212–216,218,224] He et al. studied the anisotropic shape-morphing abilities of bilayer hydrogels in response to the saline solution or thermal stimulus. The bilayer hydrogel formed helical structures upon exposure to external stimuli. They also investigated the effect of geometrical parameters, such as the width and thickness of the strips, and environmental conditions, such as the concentration of ions in the saline solution, on the morphology of the morphed hydrogel.[215]

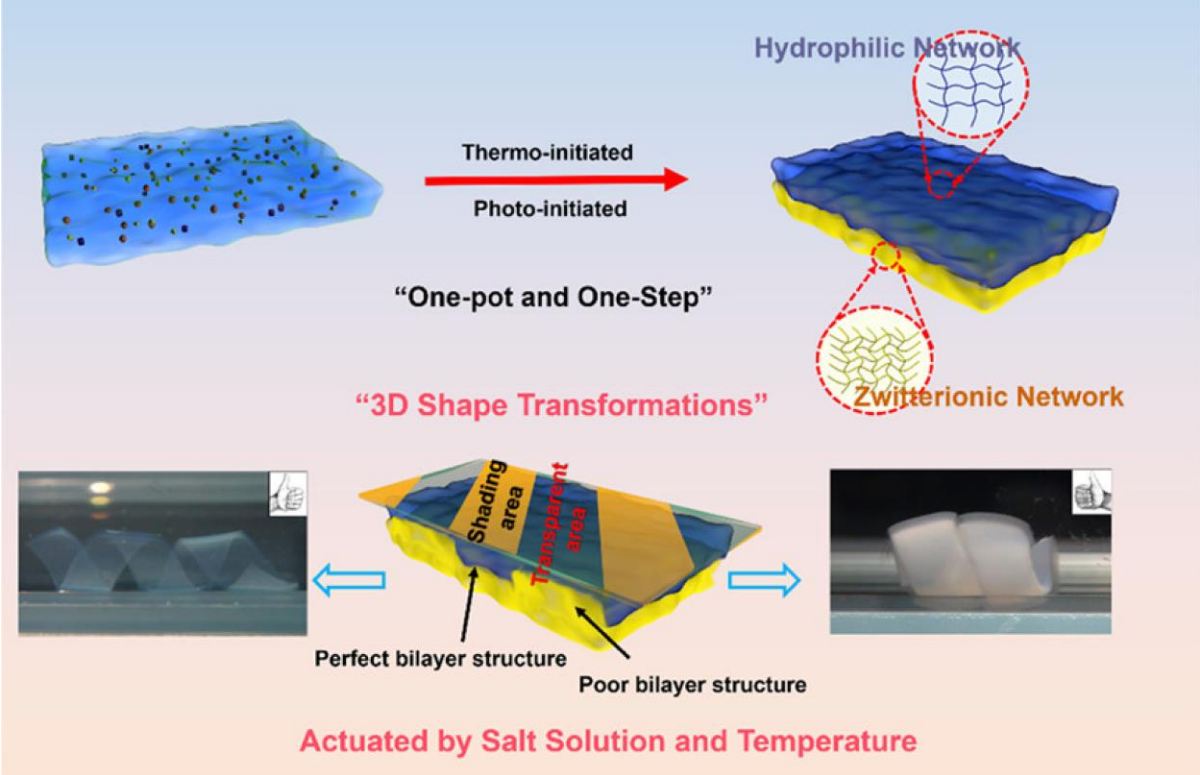

Figure 2-9. Relationship between the swelling-induced bilayer hydrogel shape and layering orientation with respect to the long axis of the substrate sheet. Reproduced with permission.[215] Copyright 2023, ACS.

2.5 Research Objectives

In this research project, we aim to develop a novel hydrogel copolymer using zwitterionic/acrylate chemistry. Our proposed hydrogel system presents numerous opportunities for the development of functional soft robots. To program the anisotropic shape transformation of the hydrogels, two approaches have been employed. The first approach involves developing CNC-based hydrogel nanocomposites, which enables programmability by incorporating microstructural anisotropy thanks to the shear-induced orientation of high aspect ratio CNC nanoparticles. The second approach involves introducing macrostructural anisotropy by integrating hydrogel layers with different physiochemical properties into a single device, which allows for the creation of complex shape changes by changing the geometrical parameters of the bilayer hydrogels.

The proposed hydrogel represents a promising material choice for fabricating biomedical robots. As a proof-of-concept, several tethered and untethered robotic functions, such as locomotion, gripping, and transportation, have been designed and performed by the fabricated robots. **Figure 2-10** demonstrates the main characteristics of the proposed hydrogel system that makes it a good material choice, meeting the qualifications for robotic functionality.

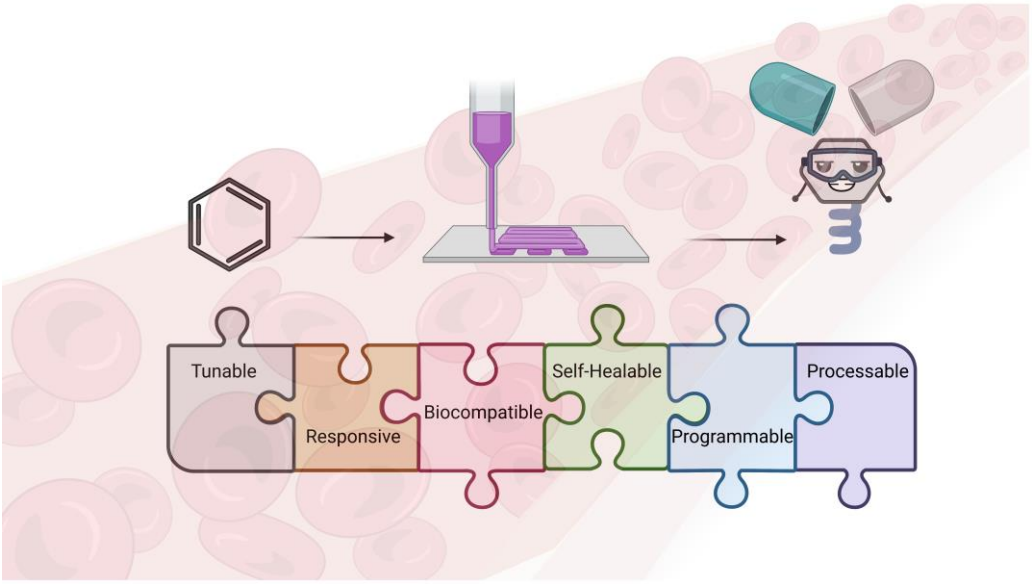

Figure 2-10. Main characteristics of materials for robotic applications.

Chapter 3
Materials and Methods

3.1 Methods

3.1.1 Materials

3-dimethyl(methacryloyloxyethyl)ammonium propanesulfonate (DMAPS, 95%), 2-Hydroxy-2-methylpropiophenone (97%), Iron(II) chloride (FeCl2, 98%), Iron(III) chloride (FeCl3, 97%), Hydrochloric acid (HCl, 37%), Sodium hydroxide pellets (NaOH, ≥ 97%), Ammonium hydroxide solution (NH4OH, ≥ 30%), Ethanol (>98%), N,N'-Methylenebis(acrylamide) (BIS, 99%), and Methacrylic acid (MAA, 99%) were purchased from Sigma-Aldrich Co., Canada. Cellulose nanocrystal (CNC, ≥ 94%) was acquired from CelluForce Inc., Canada. Deionized water (DI water, > 16 MΩ cm resistivity) was used in all of the experiments. All the chemicals were used without further purification.

3.1.2 DMAPS-MAA Hydrogels

Hydrogels were prepared by photopolymerization of an aqueous solution of DMAPS and MAA monomers. The total monomer concentration was kept at 50 wt%, with the DMAPS:MAA weight ratio varying between 1:2 and 3:1 to prepare SBMA1-4 samples, respectively. For each sample, 30 mg of 2-Hydroxy-2-methylpropiophenone was added to 5 g of DI water. The hydrogel precursor was then injected into a cell prepared using two glass slides (5 cm × 5 cm) separated by two strips of 500 μm spacers. After purging with nitrogen for 30 min, UV polymerization was conducted at 60°C in a container also purged with nitrogen. Each side of the cell was exposed to UV light at a wavelength of 365 nm for 45 minutes. Following polymerization, the hydrogels were washed with Milli-Q water to remove residual unreacted chemicals.

3.1.3 DMAPS-MAA-BIS Hydrogels

BIS cross-linker was added to the aqueous solution of DMAPS and MAA monomers at a 1:400 molar ratio. The concentration of the other components was kept constant. All preparation parameters, as well as polymerization conditions, were kept the same as the procedure described in the previous section.

3.1.4 DMAPS-MAA-CNC Hydrogel Nanocomposites

CNC at concentrations of 3-10 wt% was added to the aqueous solution before the addition of other components. The amounts of monomers, cross-linker, and initiators were kept constant. The precursor was then transferred onto a glass slide placed between two strips of 500 μm spacer glued to the edges. The CNCs were aligned by sharing the precursor with the edge of another glass slide. The suspension was then covered with a glass slide and subjected to the same polymerization procedure as described in the previous section.

3.1.5 Synthesis of Magnetic Iron Oxide Nanoparticles (Fe_2O_3 NPs)

Magnetic iron oxide nanoparticles were synthesized using the precipitation method.[225,226] Briefly, 10 g $FeCl_3$, and 4.05 g $FeCl_2$ were dissolved in 550 mL of deionized water under magnetic stirring for 90 ˚C. Then, 30 mL of NH_4OH solution (30 wt.%) was gradually added (10 ml/min) to the stirring iron salt solution to anticipate the redox reaction. The reaction vessel was maintained at 90 ˚C under magnetic stirring for 1 hour. The resulting precipitate was collected, followed by rinsing with deionized water and ethanol and dried in the air.

3.1.6 Synthesis of Magnetic CNCs (MCNCs)

MCNC was synthesized using co-precipitation of iron salts on CNC as described elsewhere.[227–231] A suspension of CNCs (100 ml, 0.2 wt.%) was degassed with N2 for 20 min in a three-neck flask. After that, $FeCl_2$ and $FeCl_3$ were added to the mixture while stirred vigorously for an additional 30 min. The pH was adjusted by slowly adding NH4OH to the suspension (pH~10) which caused it to turn black. After stirring for 30 minutes at 70 °C, the mixture was cooled to room temperature by adding deionized water. MCNC nanoparticles were washed repeatedly with distilled water and ethanol, then separated with an external magnetic field and centrifugation (6000 rpm, Thermo ScientificTM, SorvallTM ST) to remove any impurities. The precipitated MCNC nanoparticles were then preserved in ethanol for further use.

3.1.7 Magnetic DMAPS-MAA Hydrogels

Magnetic iron oxide nanoparticles (5 wt%) were incorporated into the aqueous phase (3 wt.% CNC solution in DI water) before the addition of other components. The amounts of monomers, cross-linker, and initiators were kept constant. The precursor was transferred onto a glass slide between two strips

of 300 μm spacers glued to the edges. The suspension was then covered with another glass slide. The rest of the procedure is similar to the previous section.

3.2 Characterization

Polarized Optical Microscope (POM): POM images were captured by Euromex iScope (Fullerscope) microscope. The samples were placed on a glass slide, and the microscope was calibrated by adjusting the magnification and the sample stage to ensure optimal contrast and clarity of the image. The samples were viewed under both cross-polarized and parallel-polarized light to observe the birefringent properties of the material. The orientation of the sample was also adjusted to observe changes in color and intensity, which revealed important information about the sample's structure.

Transmission Electron Microscope (TEM): The morphology of CNC and synthesized MCNC nanoparticles was investigated by transmission electron microscopy. The powder sample was dispersed in water (1 mg ml^{-1}), and about 10 μl of the dilute dispersion was cast onto the surface of a 300 mesh grid which was then dried at an ambient temperature for 24 hours before taking the images on a Philips CM10 transmission electron microscope.

Rheology: The rheological properties of the precursor and hydrogel were characterized using a rheometer (HAAKE MARS, Thermo Scientific) with a 20 mm parallel plate geometry and a gap of 0.7 mm. Viscosity vs share rate was measured to confirm the shear thinning of the hydrogel precursor. The strain sweep (0.1–100%) was performed at a fixed frequency of 10 rad/s to determine the linear viscoelastic range. Then, a dynamic frequency sweep (0.1 to 100 rad s^{-1}) at a constant strain of 1.0 % was applied. Water evaporation was minimized during the temperature sweep tests using a solvent trap. Finally, the step-strain test was conducted to investigate the self-healing properties of the hydrogel for several cycles.

Mechanical Testing: Tensile testing of hydrogel was performed using a CellScale tensile machine (UniVert, Canada). Before running tensile tests on hydrogel samples that have been swelled in water for 2 hours, the samples were cut into appropriate sizes and shapes using a razor blade, taking care to avoid introducing any damage or defects to the hydrogels. Then, the samples were carefully mounted onto the Cellscale's clamps, ensuring that they were held securely in place without any slipping or sliding.

Scanning Electron Microscope (SEM): The alignment of CNC nanoparticles was investigated by scanning electron microscopy (SEM). Hydrogels were frozen and snapped in the liquid nitrogen and dried in the freeze-dryer for 24 hours. The final samples were mounted on a sample holder and gold-sputtered before taking the images with a Hitachi S-3500N VP SEM.

Fourier-Transform Infrared (FTIR): A Nicolet NEXUS 870 Fourier-transform infrared (FTIR) spectrometer was employed to obtain the FTIR spectra. Samples were mixed with KBr powder and pressed into pellets for the measurements with a wave number range set at 4000-500 cm^{-1} and a resolution of 1 cm^{-1}. A total of 64 scans were accumulated to reduce the spectra noise.

Vibrating Sample Magnetometer (VSM): Magnetization measurements were obtained at room temperature using a vibrating sample magnetometer (VSM, 8600 Series Magnetometer) with a maximum magnetic field of 16 kOe and a step size of 1 kOe. The magnetic hydrogel samples were carefully cut into circular discs with a diameter of 2 mm. For the magnetic nanoparticles, a small amount of powder was mixed with Krazy glue and allowed to dry. Care was taken to avoid introducing any damage or defects to the samples during this process, ensuring that they were prepared appropriately for further analysis.

Chapter 4
Programmable Nanocomposites of Cellulose Nanocrystals and Zwitterionic Hydrogels for Soft Robotics

4.1 Introduction

Programmable nanocomposites of cellulose nanocrystals (CNCs) and zwitterionic hydrogels have unique mechanical and responsive properties, making them great potential to be utilized in constructing soft robotic devices.[30,232–234]. Zwitterionic hydrogels possess stimuli-responsiveness, self-healing, and biocompatibility, rendering them applicable for designing functional actuators, especially for designing shape-morphing robots for biomedical applications.[12,30,235] On the other hand, CNCs, which are extracted from plant cell walls, exhibit remarkable mechanical properties and have been used as rheology modifiers in hydrogel systems.[236–238] In this chapter, we aim to introduce a programmable zwitterionic hydrogel nanocomposite for constructing robotic actuators. We utilize CNCs as high-aspect ratio nanofillers to introduce microstructural anisotropy to the constructs. The microstructural anisotropy is achieved by applying a unidirectional shear force to the hydrogel precursor, which results in the directional orientation of the CNCs and anisotropy in the mechanical and physiochemical properties of the hydrogels. This approach offers an easy method to program the shape-morphing mode of the hydrogel actuators. To the best of our knowledge, Zwitterionic/Acrylate chemistry has never been used in fabricating anisotropic hydrogel nanocomposites for soft robotic applications. In this chapter, we elaborate on the concept of utilizing the unique properties of CNC-modified zwitterionic hydrogel nanocomposites for soft robotic applications by showcasing how we used our fabricated actuators in designing robotic constructs, capable of gripping and transporting objects in confined environments.

4.2 System Concept

To synthesize self-healing hydrogels that undergo programmable, stimuli-responsive shape transformation, we designed a synthetic protocol based on the copolymerization of 3-dimethyl (methacryloyloxyethyl) ammonium propanesulfonate (DMAPS) and methacrylic acid (MAA) in the presence of CNC nanoparticles. It is known that copolymerizing sulfobetaine methacrylates, such as zwitterionic monomers, with a small amount of MAA, improves the mechanical properties of resulting hydrogels due to the hydrophobic associations imposed by CH_3 groups of MAA.[231] Zwitterionic

hydrogels from a random copolymer of DMAPS and MAA have shown self-healing properties as a result of dynamic electrostatic interactions between oppositely charged groups and hydrogen bonding.[31,186,187,239,240] Additionally, DMAPS-MAA copolymers are sensitive to temperature, ionic strength, and pH, making them ideal building blocks for stimuli-responsive shape-morphing soft robots.[188,241–244]

Cellulose nanocrystals are outstanding examples of 1-D nano-reinforcing materials that have gained increasing attention due to their sustainable sources, unique mechanical properties, and surface characteristics.[245] Similar to other 1-D nanoparticles with high aspect ratios, confined CNC nanoparticles could be oriented by external shear forces. This strategy is versatile and compatible with extrusion 3D printing and has been previously used to induce anisotropy in hydrogels.[18,246–248] Inspired by this strategy, the shear-induced alignment of CNCs in our poly(DMAPS-MAA) hydrogel precursors could be utilized to induce structural anisotropy (**Figure 4-1a-b**). The self-healing properties of poly(DMAPS-MAA) would also enable us to employ a cut-and-paste strategy to prepare complex stimuli-triggered shape-morphing systems (**Figure 4-1c**). A combination of programmable stimuli-responsiveness and a cut-and-paste approach could be used to fabricate both tethered and untethered soft grippers (**Figure 4-1d-e**).

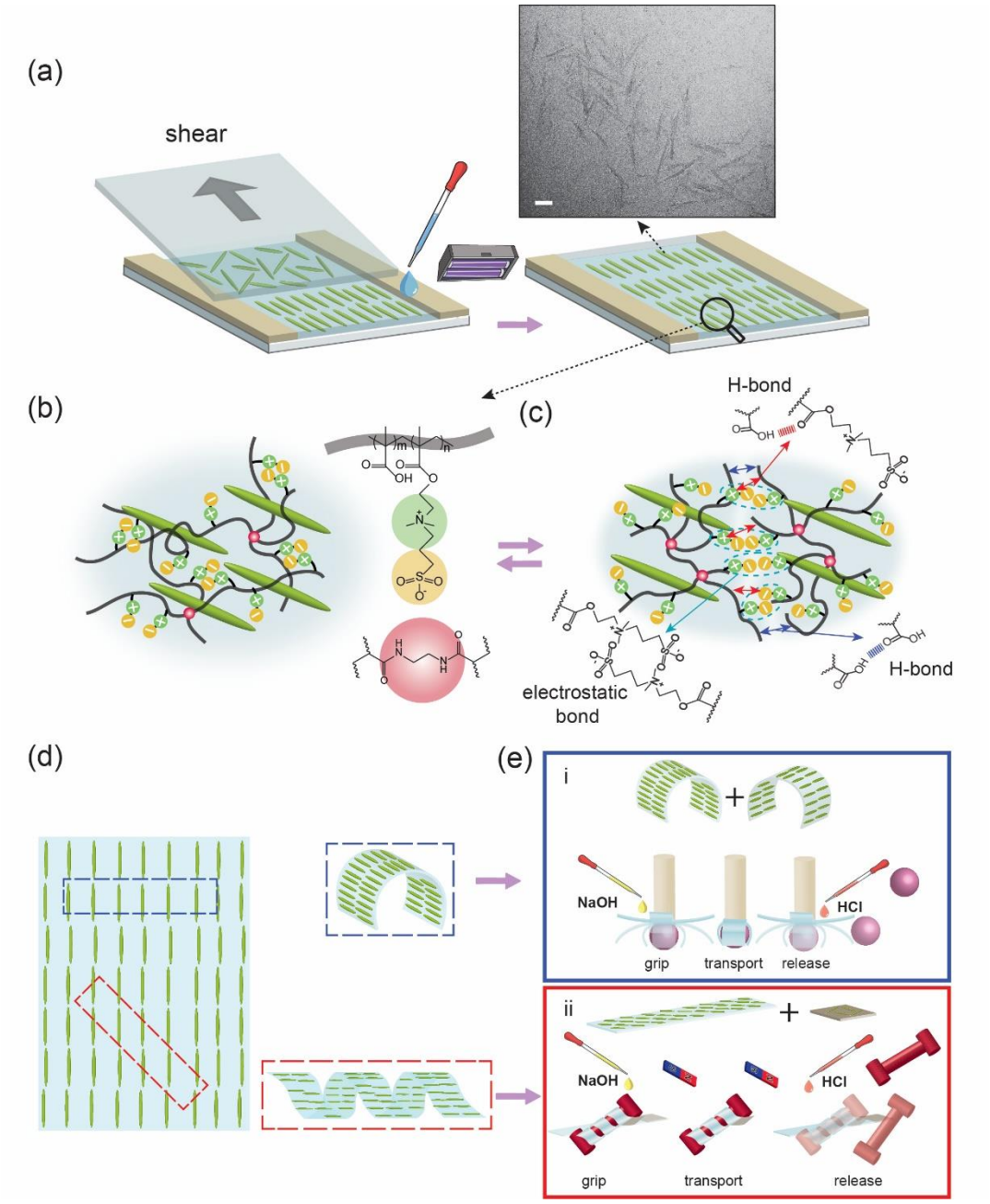

Figure 4-1. Concept of Synthesizing Anisotropic Hydrogels. a) The schematic of the fabrication of the anisotropic stimuli-responsive hydrogel and TEM image of CNCs. The scale bar is 100 nm. b) The chemical structure of the hydrogel components. c) Schematic of the self-healing mechanism of the hydrogel through noncovalent reversible crosslinking. d) Shape-change programming of the anisotropic hydrogel. e) Schematic of the cut-and-paste strategy to design functional (i) tethered and (ii) untethered soft grippers.

To find the soft actuator with optimal self-healing and mechanical properties, responsiveness, and programmability, we prepared a series of hydrogel precursors with different chemical compositions. These precursors were then polymerized between two glass slides separated with spacers of known thickness under UV light at a wavelength of 365 nm. In this systematic work, we first synthesized and studied physically cross-linked hydrogels, modified their formulation by chemical crosslinking, and finally added CNC nanoparticles to achieve programmable soft actuators from hydrogel nanocomposites with desired properties.

4.3 Physically Cross-Linked Hydrogels

At first, we synthesized physically cross-linked hydrogels and systematically studied their self-healing and mechanical properties. In all precursors, DMAPS and MAA were the main comonomers polymerized with different weight ratios ranging from 1:2 to 4:1 (DMAPS: MAA). Results of the tensile test in **Figure 4-2a** demonstrate that the physically cross-linked hydrogel with a 3:1 DMAPS: MAA weight ratio (called GelWC hereafter), although soft, is still mechanically robust and practical for soft robotic applications. In tandem, strips of physically cross-linked hydrogel samples were cut in half, and the two pieces were brought into contact for self-healing experiments. First, we studied the effect of time on the self-healing of GelWC and noticed a gradual enhancement of healing efficiency with time. After about 4 hours, GelWC showed full recovery, as shown in **Figure 4-2b**. The comparison between the results of mechanical testing on the original physically cross-linked hydrogels of different formulations and their self-healed counterparts after 6 hours also revealed the complete recovery of mechanical properties, or self-healing efficiency of 100%, for hydrogels containing at least 75 wt% of DMAPS (**Figure 4-2c**). Given its excellent self-healing and acceptable mechanical properties, the composition of GelWC was chosen for further modification in our study.

Response to external stimuli, such as pH, in the form of reversible shape-morphing triggered by swelling/deswelling, is crucial for the functionality of hydrogels as soft robots. To confirm the stimuli-responsiveness of GelWC samples, we studied their swelling/deswelling mechanism in response to changes in environmental pH, which is schematically depicted in **Figure 4-2d**. **Figure 4-2e** shows the degree of swelling ($(L-L_0)/L_0$, where L_0 and L are the initial and post-swelling lengths of samples, respectively) of a GelWC sample in neutral, high, and low pHs. After about 2 hours, samples reached equilibrium in water (pH ~ 7). By placing the samples in a buffer with pH 12, they started to swell rapidly. Placing the samples in a buffer with pH 3 forced them to lose some water and return to their

original size. To confirm the effect of pH on the swelling/deswelling behavior of the GelWC samples after equilibration in water, they were first placed in a buffer with pH 3 and then in a buffer with pH 12. The size of the samples did not change at pH 3 but increased rapidly at pH 12 (**Figure 4-2f**). At high pH values (greater than 4.7), the -COOH groups of MAA are ionized, and the charged -COO- groups repel each other, leading to the swelling of the hydrogel, while at lower pHs, this process is reversed.[241] However, the swelling/deswelling of GelWC samples with changes in pH was not repeatable, and the hydrogel started to degrade after three consecutive exposures to high and low pHs. This can most likely be attributed to the breaking of the intergroup electrostatic association due to the screening of zwitterionic moieties by oppositely charged ions in the environment.[244]

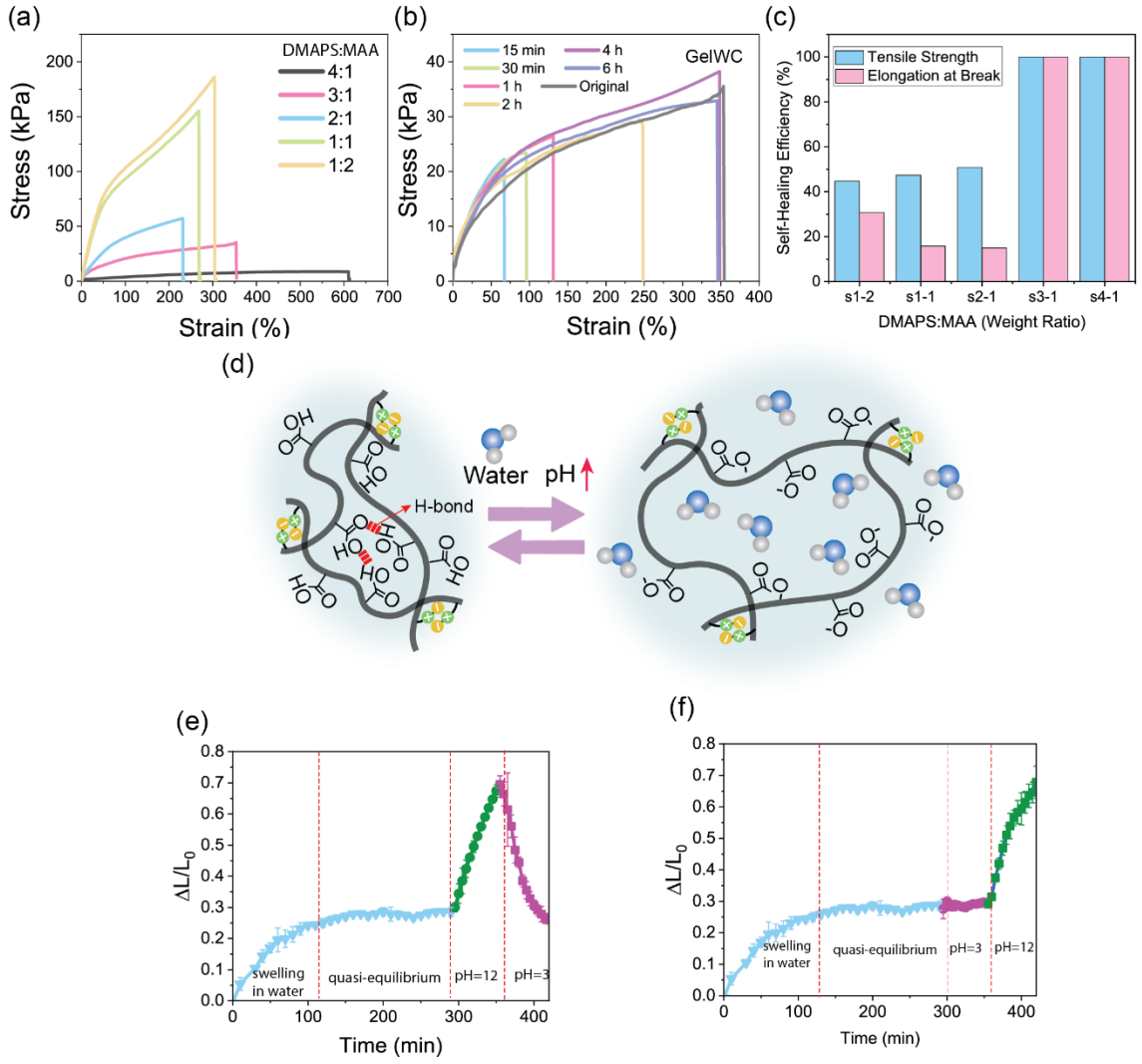

Figure 4-2. Hydrogel behavior. a) Stress-strain behavior of physically-crosslinked DMAPS-MAA hydrogels containing different ratios of comonomers. b) Stress-strain behavior of GelWC after self-healing as a function of time. c) Self-healing efficiency of physically-crosslinked DMAPS-MAA hydrogels samples containing different ratios of comonomers after 6 h of healing. d) Schematic presentation of the swelling/deswelling mechanisms of a GelWC sample in response to pH. e) The degree of swelling of a GelWC sample in water (pH ~ 7) and in buffers with pH 12 and 3. f) The degree of swelling of a GelWC sample in water (pH ~ 7) and in buffers with pH 3 and 12.

4.4 Chemically Cross-Linked Hydrogels

To improve the reversibility of GelWC swelling/deswelling, we introduced a small amount of N, N'-methylene bis (acrylamide) (BIS) as a chemical crosslinker to the hydrogel formulation. Our goal was to enhance the pH-responsive swelling/deswelling by introducing chemical crosslinking to the

hydrogels. After varying the concentration of BIS and conducting swelling/deswelling experiments, we determined that hydrogels with a 167:1 weight ratio of comonomers: BIS (molar ratio 143:1) exhibited reversible swelling/deswelling, and we refer to them as Gel in the subsequent analysis.

4.5 Hydrogel Nanocomposites

Inducing anisotropy into the microstructure of hydrogels has been proven to lead to differential swelling and is an essential step in the fabrication of programmable shape-morphing hydrogels.[7,249–251] The unidirectional shear of 1D nanoparticles, such as CNC, has been employed in a few reports as an effective method of inducing anisotropy in hydrogels' microstructure.[252–254] It is also known that CNC nanoparticles can be aligned by external stress induced by shear, magnetic, and electric fields, especially when they are present in a liquid crystalline phase.[22,255,256] As such, we postulated that the addition of CNC nanoparticles to hydrogel precursors can impart a liquid crystalline phase, and their shear alignment can lead to anisotropy in our DMAPS-MAA hydrogels' microstructure. For this, we modified the formulation of the Gel precursor and replaced water with a 10 wt% CNC suspension (see Materials and Methods for details). In our preliminary experiments, we found that the concentration of CNC in the final hydrogel precursor must be above 4 wt% to ensure the realization of the liquid crystalline phase. Furthermore, we confirmed the shear thinning of Gel precursors containing CNC nanoparticles in rheology tests (**Figure 4-3a**).

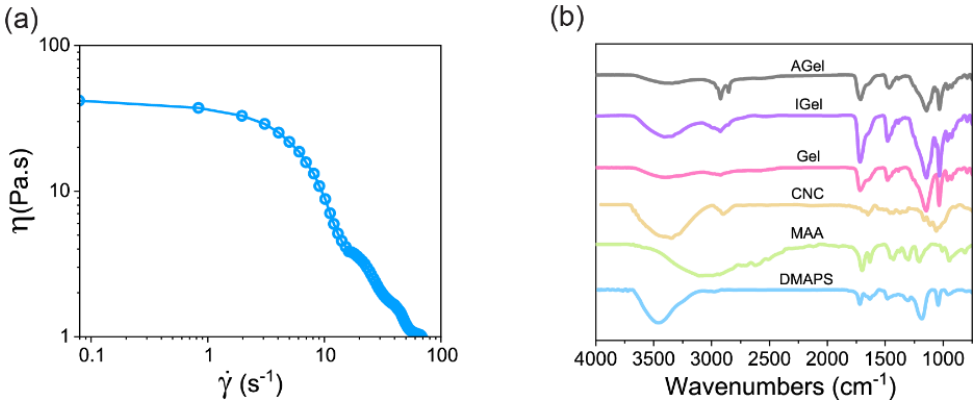

Figure 4-3. a) The viscosity of AGel precursor as a function of shear rate at 25 °C shows the shear thinning behavior. b) FTIR spectra of the hydrogels and their components. The C=C stretching and C-O stretching regions are highlighted in blue and green, respectively.

Gel precursors containing 5 wt% CNC nanoparticles were accordingly polymerized in capillary cells either to anisotropic hydrogels with preferential CNC alignment (AGel) or isotropic counterparts without any preferential CNC alignment (IGel). AGel samples were prepared by casting the precursor on a glass substrate and confined by spacers, followed by applying a unidirectional shear force via moving a glass counter substrate on top several times (**Figure 4-1a**). To prepare IGel samples, the counter substrate was gently placed on the casted precursor without any lateral movement. The photopolymerization was then carried out to fix either the unidirectional or random alignment of the CNCs inside hydrogel precursors.

We performed FTIR tests to confirm that the presence of CNC does not disturb the polymerization reaction (**Figure 4-3b**). The MAA spectrum showed a distinctive peak at approximately 1635 cm^{-1}, corresponding to the stretching of the C=C.[257] The peak at around 1630 cm^{-1} is attributed to the C=C stretching in the structure of DMAPS.[258] After polymerization, the amplitude of the C=C characteristic peak (highlighted in blue) reduced substantially in AGel, IGel, and Gel spectra, suggesting the successful polymerization of the monomers.[259] The small peak at 1060 cm-1 in the IGel and AGel spectra (highlighted in green) is due to the stretching of the C-O bonds of CNC, as it can also be observed in the CNC spectrum.[116]

4.6 Anisotropy of Hydrogel Nanocomposites

Different techniques were used to confirm the anisotropy present in the hydrogel microstructure. Hydrogels that contained CNC (IGel and AGel) were transparent under natural light but exhibited vivid interference colors when viewed through crossed polarizers or a polarized optical microscope (POM) (**Figure 4-4a,b**). Regardless of the orientation with respect to POM's polarizer/analyzer, IGel showed a heterogeneous multicolor transmission pattern, confirming the isotropic microstructure of the hydrogel precursor polymerized in a polydomain liquid crystalline phase. In contrast, AGel showed a uniform monochromatic transmission when observed between crossed polarizers. The highest transmission through the sample was observed when the longer side of the sample (parallel to the shear) was positioned at 45˚ with respect to the polarization axis, and the sample appeared dark when it was parallel to either the polarizer or the analyzer. These results suggested that the CNCs in the hydrogel precursors indeed formed a nematic phase that could be aligned along the shearing direction and retained even after photopolymerization.[230] To investigate the uniformity of the alignment along the thickness, the cross-section of AGel (parallel to the shear) was studied by POM. The POM image of

the AGel cross-section positioned 45˚ with respect to the polarization axis revealed two distinct layers, one bright and one dark, confirming the anisotropy gradient along the thickness (**Figure 4-4c**). The sample appeared dark when it was parallel to the polarization axis. The POM images of the IGel cross-section positioned 45˚ and parallel to the polarization axis appeared similar, confirming the isotropic microstructure (**Figure 4-4c**). These images confirmed that moving a glass slide on the top surface of hydrogel precursors produced a shear stress gradient along the thickness. However, the applied shear was not large enough to induce the alignment of CNCs in the precursor throughout the thickness beyond a certain threshold, leading to a gradient in anisotropy.

To investigate the effect of applied shear on the microstructure of AGel samples, scanning electron microscopy (SEM) images were taken of their surface and cross-sections (**Figure 4-4d**).[245] The SEM image of the AGel surface exposed to shear before polymerization revealed microstructural alignment in the direction of the shear, while SEM images of the cross-section confirmed the POM results, showing an anisotropy gradient along the thickness. For typical AGel samples, the unidirectional microstructural anisotropy was less pronounced for regions closer to the bottom substrate. The larger portion of aligned thickness in the POM image of the AGel cross-section is likely due to the fact that POM images were taken from swollen samples, and the aligned region had higher swelling compared to the isotropic region. To maximize the portion of thickness in which shear force can induce alignment, the gap used for capillary cells was varied from 500 μm to 250 μm. The gradient of microstructural anisotropy was less pronounced for films with a thickness of 250 μm. However, manipulating hydrogels thinner than 500 μm was challenging, so 500 μm was chosen as the initial thickness for the rest of the studies.

We then investigated the effect of CNC alignment on the degree of swelling of Gel, IGel, and AGel hydrogels in water (**Figure 4-4e**). Upon immersion in water, all hydrogels started to swell and after about 1 hour reached a pseudo-equilibrium state in which their swelling rate decreased significantly. While Gel and IGel expanded uniformly in all directions, the expansion of AGel in the direction perpendicular to the alignment was much more pronounced than that in the direction parallel to the alignment. When the pH or ionic strength of the environment was increased, the anisotropic swelling of AGel became even larger and more noticeable.

To study the effect of CNC nanoparticle addition and their alignment on the mechanical properties of the hydrogel at micro and macro scales, we performed rheology and tensile tests on dimensionally

identical circular and rectangular specimens of Gel, IGel, and AGel, respectively. For rheology, we cut circular discs with identical radii and thickness from Gel, IGel, and AGel samples. **Figure 4-5a** demonstrates the rheological behavior of these hydrogels. To confirm the formation of hydrogels at room temperature, frequency-dependent dynamic shear moduli measurements were performed in the linear viscoelastic region (1% strain, 1 Hz) to ensure that the microstructure of the hydrogels was preserved. In the entire frequency range, the storage modulus G′ was greater than the loss modulus G″, suggesting the solid-like behavior of all hydrogels (**Figure 4-5a**).[229] The storage modulus of Gel was the highest among the three hydrogels, followed by IGel and AGel in the entire frequency range. The decrease in the storage modulus of IGel and AGel can be attributed to the drastic enhancement of hydrophilicity and water content of the hydrogels by introducing CNC to their formulation, as shown in **Figure 4-5b**. The strain amplitude sweep test on the hydrogels indicated that the 1% strain at which the frequency-dependent dynamic shear moduli measurements were performed was in the linear viscoelastic region of the hydrogels (**Figure 4-5c**).[260]

For the tensile test, we cut specimens from Gel and IGel samples whose long axes were perpendicular to each other. We also cut specimens from an AGel sample, whose long axis was parallel and perpendicular to the shearing direction. As anticipated, Gel and IGel specimens showed almost identical mechanical properties measured in different directions. AGel showed a higher tensile modulus and tensile strength in both directions compared to Gel (**Figure 4-4f**). The tensile modulus and tensile strength of AGel specimens stretched parallel to the alignment direction are higher than those of AGel specimens stretched perpendicular to the alignment direction. Such a large difference in the mechanical properties of Gel and AGel, and those of AGel measured parallel and perpendicular to the alignment, indicates the key role the presence and alignment of CNC nanoparticles play in the reinforcement of gels and inducing mechanical anisotropy in AGel hydrogel composites, respectively.

We then investigated the influence of CNC alignment on the optical properties of AGel when subjected to elongation. **Figure 4-4g** shows the gradual color changes for specimens of AGel stretched parallel and perpendicular to the direction of CNC alignment. The color change pattern is completely different for these two specimens, confirming the anisotropy in the microstructure. The color change for AGel stretched parallel to the alignment direction is mostly due to the change in specimen thickness, while the alignment of the CNCs is maintained intact.[230] For AGel stretched perpendicular to the alignment direction, elongation of the specimen at first disrupts the orientation of the CNCs, leading to

the loss of birefringence, while with further elongation, the CNCs start to orient in the parallel direction, causing birefringence again.[22]

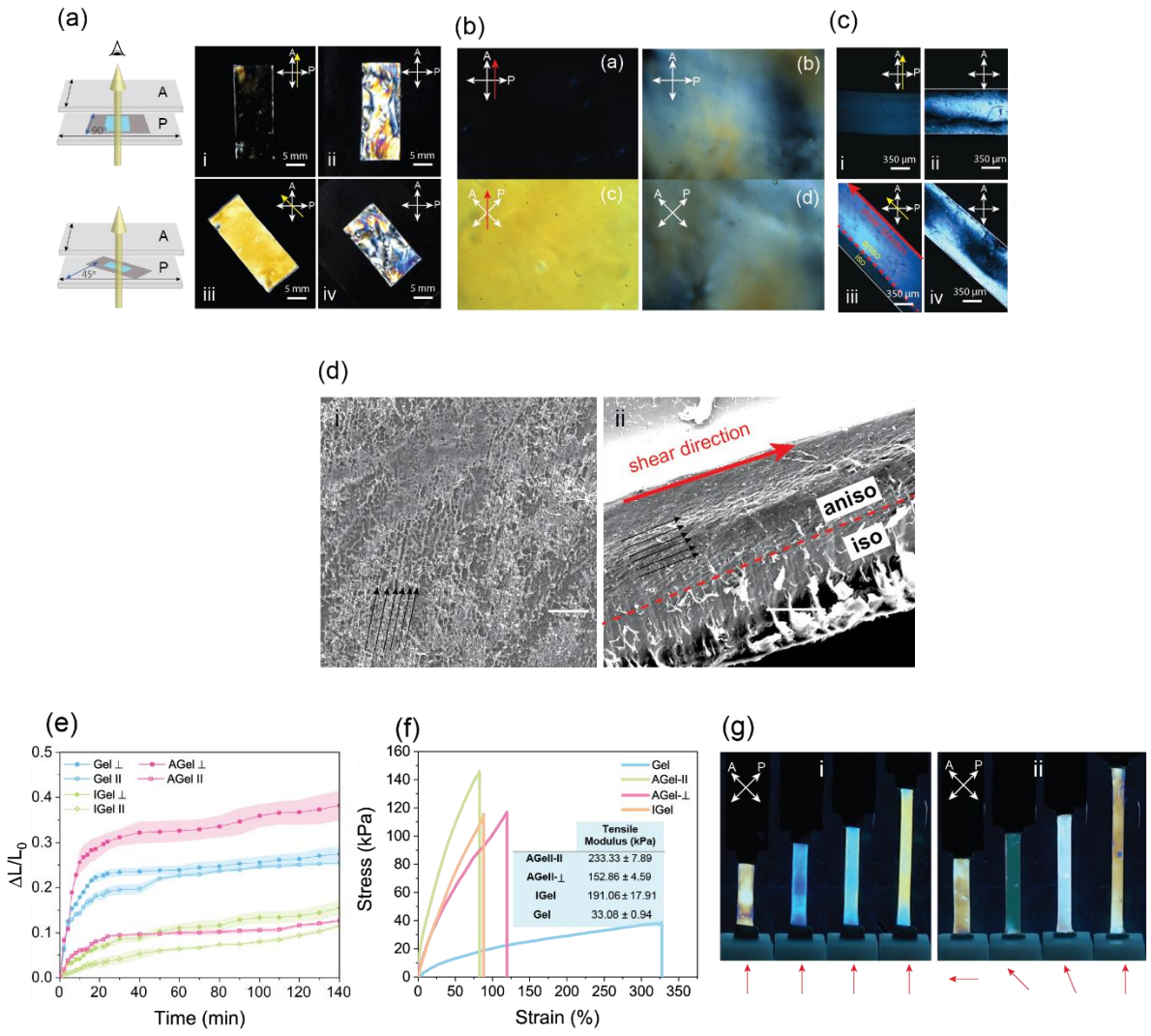

Figure 4-4. Anisotropy of hydrogel nanocomposites. a) Images of AGel (i and iii) and IGel (ii and iv) between crossed-polarizers. CNC alignment direction is shown with a yellow arrow. b) POM images of (a, c) AGel and (b, d) Gel. c) POM images of the cross-section of AGel (i and iii) and IGel (ii and iv). CNC alignment direction is shown with a yellow arrow. The red dashed line separates the regions with and without alignment. d) SEM images of AGel surface exposed to shear (i) and cross-section (ii). Black arrows show the direction of CNC alignment. The red dashed line separates the regions with and without alignment. The size of the error bar is 100 µm and the initial thickness of the sample before freeze-drying was 700 µm. e) Degree of swelling in time for Gel and IGel in two perpendicular directions and that of AGel parallel and perpendicular to the CNC alignment. f) Tensile test results of Gel, IGel, and AGel in parallel and perpendicular directions to CNC alignment along with the tensile modulus values calculated using the tensile testing of at least three replicates. g) The color changes of AGel samples elongated parallel to the direction of CNC alignment. CNC alignment direction was fixed at 45° relative to the polarizer and analyzer while samples were elongated parallel (i) or perpendicular (ii) to the CNC alignment direction. CNC alignment direction is shown with red arrows.

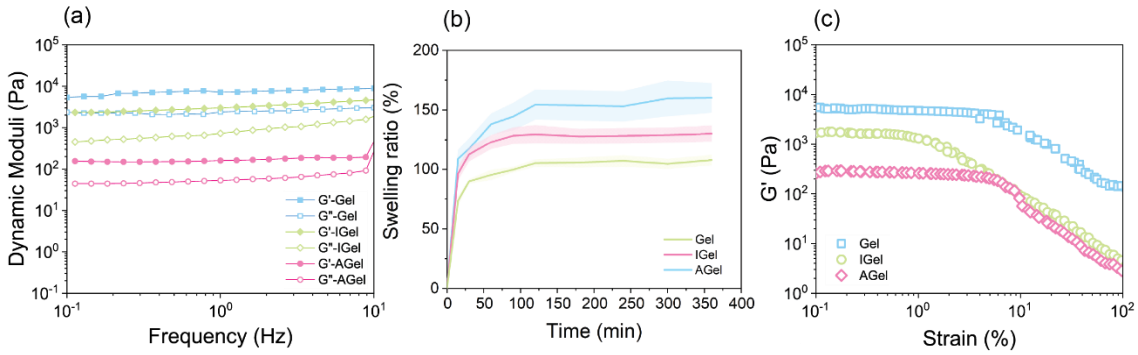

Figure 4-5. a) Frequency-dependent dynamic shear moduli of hydrogels at 1% strain and 1 Hz. b) Swelling behavior of Gel, IGel, and Agel. The swelling ratio is defined as $\frac{m-m_0}{m_0} \times 100$, where m and m_0 are weight at time t and initial weight, respectively. c) Amplitude sweep experiment on Gel, IGel, and AGel showing the linear viscoelastic region.

4.7 Self-Healing of Hydrogel Nanocomposites

To successfully employ the cut-and-paste strategy for creating complex shape-morphing constructs that can be triggered by various stimuli, it is essential to have appropriate self-healing properties. Intrinsic self-healing hydrogels can be broadly categorized into two approaches: dynamic covalent crosslinking and noncovalent physical cross-linking.[261] Our hydrogel belongs to the second category, where dynamic hydrogen bonds and ionic associations enable interdiffusion of the chains across the crack and their engagement in new junctions, as shown in **Figure 4-1c**.[231]

To evaluate the recovery of hydrogel mechanical properties at the microscale following the network rupture at high strain, step-strain measurements were performed.[262] When Gel and AGel were subjected to a small strain in the linear viscoelastic region (1%, **Figure 4-6a**) for 200 s, G′ was greater than G″. By increasing the strain to a value greater than the linear viscoelastic threshold (100%, **Figure 4-6a**) for 200 s, G′ dropped immediately and became smaller than G″, indicating network disruption. After 200 s of rest, the strain was reduced to 1% again and the hydrogel exhibited complete recovery of both G′ and G″. This result was reproducible upon additional strain cycles, as can be seen in **Figure 4-6b-c**. To evaluate the self-healing efficiency of hydrogels at the macroscale, tensile tests were performed on the original and self-healed samples. The self-healing efficiency of the Gel was evaluated after 6 hours of healing, and limited self-healing was observed. In the presence of the cross-linker, the ability of the hydrogel to retain water decreased. The expelled water accumulated on the surface of the Gel samples, interrupting the self-healing process.

Adding CNC to the hydrogel enhances the hydrophilicity of the network which can prevent water accumulation on the surface of the hydrogel by retaining the water inside. Consequently, healing efficiency of ~50% and ~90% was observed for AGel in alignment and perpendicular directions, respectively **(Figure 4-6d**,**e**). Higher swelling of AGel in the perpendicular direction compared to the alignment direction (**Figure 4-4f**) facilitates the chain movements and interdiffusion across the crack resulting in more effective healing in this direction. We also examined the self-healing of Gel and AGel samples with isotropic and anisotropic swelling profiles. **Figure 4-6f** shows a rectangle (5 mm × 25 mm) made of one piece of Gel (lower half) and one piece of AGel cut in the perpendicular direction (upper half) after 6 hours of healing. After around 100% strain, the sample broke but not at the healed area indicating that the healing of AGel and Gel pieces was effective and that the healed region was at least as strong as the pristine hydrogels.

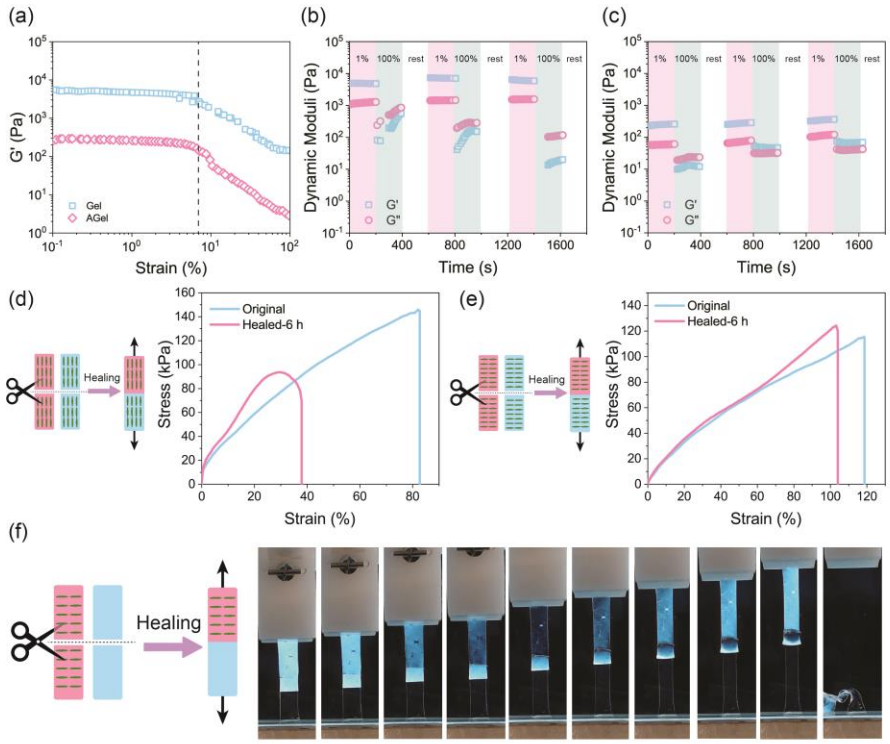

Figure 4-6. Self-healing of hydrogel nanocomposites. a) Amplitude sweep results on Gel and AGel showing the linear viscoelastic region. Step-strain experiment on b) Gel and c) AGel. Large strain (100%) inverted the values of G′ (squares) and G″ (circles), indicating breakage of crosslinks. G′ was recovered under a small strain (1%). Self-healing of AGel in d) alignment and e) perpendicular directions after 6 h. f) Stretching a rectangular sample (5 mm × 25 mm) made of one piece of Gel (lower half) and one piece of AGel cut in the perpendicular direction (upper half) healed for 6 hr. Due to the rotation of CNCs upon extension, the upper half becomes first transparent and then white again.

4.8 Shape-Change Programming

The reversible in-plane and out-of-plane anisotropic swelling triggered by pH, the gradient of microstructural anisotropy along the thickness, and the initial geometry of single-layer AGel samples provide a robust set of adjustable parameters to program the 2D-to-3D shape-morphing. The gradient in microstructural anisotropy along the thickness facilitates bending in a mechanism similar to classical bimorph hydrogels subject to non-identical swelling along their thickness.[263–266] The unidirectional alignment of CNC on the regions closer to the top surface can guide such bending deformation in preferential directions by decoupling the deformation characteristics from the geometry of the initially flat hydrogel.[267] Our system can be deemed as a bimorph with non-identical swelling behavior along the thickness in which CNCs are oriented randomly on one side, with a characteristic thickness of hI (~200 μm), and unidirectionally aligned on the other side, with a characteristic thickness of hA (~600 μm) (**Figure 4-7a**). Similar to the deformation profile of typical bistable bimorphs, straining of the layer with the unidirectionally aligned CNCs (with higher swelling) is constrained by the layer with randomly oriented CNCs (with lower swelling). Therefore, while one layer is loaded with tension, the other layer experiences compressive stresses, and to release those internal stresses, the generated bending moment results in the bending of the flat hydrogel.[268] We have modeled the deformation behavior of the hydrogel bimorphs with finite element simulations. Through anisotropic swelling, if the long axis of strips is either perpendicular or parallel to the dominant swelling direction, the simulations show that the strip will undergo pure bending (**Figure 4-7b i-ii**). Deviation of the strips' long-axis orientation from the dominant swelling direction, in turn, leads to helicity as a result of the balance between forces induced by elastic stretching and bending (**Figure 4-7b iii**).[269–271]

To verify our simulations, we cut different samples from an AGel film whose long axes were perpendicular, parallel, and at a 45° angle with respect to the CNC alignment to investigate how CNC alignment affects the shape-morphing of the hydrogel. To trigger the shape change, we first increased the pH of the hydrogel environment to ~12, and to recover the original shape, we decreased the pH to ~3. **Figure 4-7c i** and **ii** show two strips of AGel in which the CNC alignment is perpendicular and parallel to their long axes, respectively. Both strips showed reversible bending, one parallel (**Figure 4-7c i**) and the other perpendicular (**Figure 4-7c ii**) to their long axis. The bending direction in both strips was dictated by the larger swelling, which occurs perpendicular to the CNC alignment. When the angle between the CNC alignment and the long axis of the strip is 45°, the hydrogel twists and forms a helix (**Figure 4-7c iii**).[272] The pitch of the helix can be adjusted by the angle at which the strip is cut with

respect to the CNC alignment.[118,119,273] The reversibility in shape change and soft actuators' durability are major requirements for the functionality of soft robots over a desirable time. Therefore, we also tested these parameters for AGel strips. **Figure 4-8** shows the reversible bending and unbending of a short strip of AGel for seven cycles in response to pH. The bending angle was defined as the angle between a vertical tangent applied to one edge of the hydrogel and a vector connecting two edges of the hydrogel after bending.[263]

The predictable swelling behaviors of Gel and AGel single layers, as well as their self-healing characteristics, enable the creation of a host of responsive constructs with complex deformation profiles using a cut-and-paste approach. **Figure 4-7d** shows three examples of 2D constructs made by cut-and-paste of a few pieces of single-layer Gel or AGel samples with different CNC alignment and their expected shape change. **Figure 4-7e** shows the POM images of assembled multi-piece constructs from Gel or AGel samples and CNC alignment in them. We predicted the overall shape change of multi-piece constructs using finite element simulations (**Figure 4-7f**). **Figure 4-7g** shows complex reversible 3D shape morphing of the hydrogel construct triggered by increasing and decreasing the pH. In accordance with our prediction, the anisotropic regions bend upon swelling, while the isotropic regions exhibited uniform swelling. The reversibility of the actuation allows the 3D shapes to return to their flat configuration by decreasing the pH.

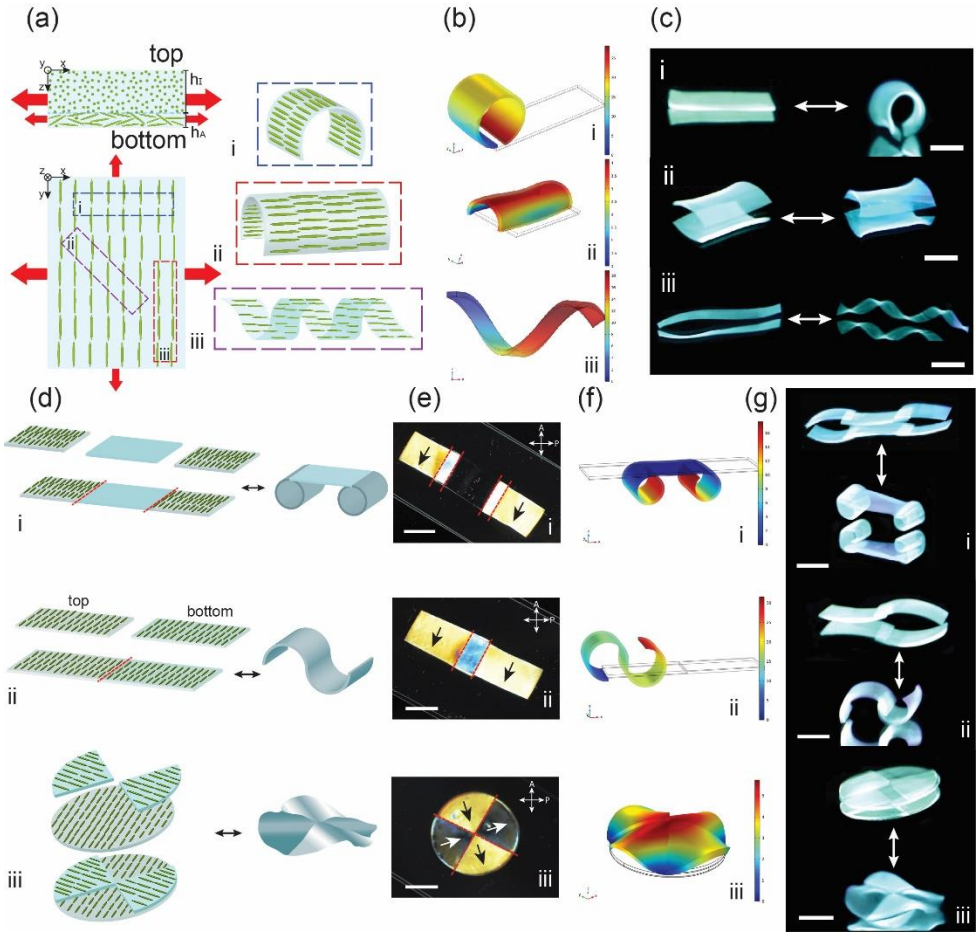

Figure 4-7. Shape-change programming of anisotropic hydrogels. a) Effect of CNC alignment with respect to the long axis of the cut piece in the shape morphing of the piece after swelling. We cut AGel film at different angles to obtain perpendicular (i), parallel (ii), and 45° (iii) CNC alignment with respect to the long axis of the cut piece. The size of the red arrows shows the level of swelling in different directions. b) Results of finite element simulations of shape change of AGel pieces cut with the CNC alignment perpendicular to the long axis (i), parallel to the long axis (ii), and making a 45° angle with the long axis (iii) in response to pH change c) Reversible shape change of AGel pieces cut with the CNC alignment perpendicular to the long axis (i), parallel to the long axis (ii), and making a 45° angle with the long axis (iii) in response to pH change. The scale bars are 10mm. d) The cut-and-paste approach to assemble the AGel and Gel pieces to make a construct with complex shape-morphing. e) Images of the assembled AGel and Gel pieces to make constructs with complex shape-morphing between two perpendicular polarizers. The scale bars are 10mm. Self-healed regions are shown by a red dashed line. CNC alignment is shown by black and wight arrows. f) Results of finite element simulations of hydrogel constructs in response to pH change g) Reversible shape changes of hydrogel constructs in response to pH change. The scale bars are 10mm.

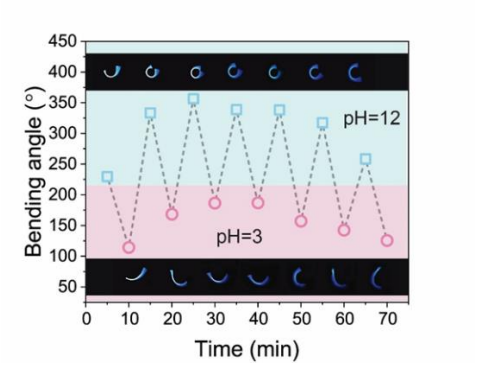

Figure 4-8. Reversible rolling and opening of a short roll for 7 cycles in response to pH. The bending angle was defined as the angle between a vertical tangent applied to one edge of the hydrogel and a vector connecting two edges of the hydrogel after bending.

4.9 Cell-Viability and Degradation of Hydrogel Nanocomposites

To examine the applicability of the fabricated hydrogel in biomedical soft robotics, we investigated the cytotoxicity properties of AGel, IGel, and Gel. To study the effect of the comonomer ratio, we also prepared a hydrogel with a flipped weight ratio of comonomers (DMAPAS:MAA weight ratio 1:3). To study the cytocompatibility of the hydrogels, a live/dead assay was performed, and cell proliferation was monitored by fluorescence microscopy over 5 days (**Figure 4-9a**). For all the hydrogels, cell viability was very high (above 95%) over the 5 days of incubation alongside the hydrogels, confirming their biocompatibility. The hydrogel prepared with the flipped weight ratio of comonomers showed high toxicity, leading to the death of most of the cells on day one of the experiments, confirming the effect of zwitterionic monomer on the biocompatibility of the hydrogel. On-demand degradation of the hydrogel is essential for its sustainability (no waste at the end of its lifetime) and biomedical application (biodegradation in the body). In an aqueous salt solution, the ions break the dipole-dipole attraction and intergroup association between the zwitterionic moieties, thus promoting the swelling and finally degradation of the hydrogel (**Figure 4-9c**).[274] Although the hydrogel without a crosslinker (GelWC) is stable for a long time underwater, it started to dissolve fast in a 10 wt% NaCl solution upon immersion (**Figure 4-9b**). In this work, chemically-crosslinked hydrogels are not fully degradable. However, we anticipate that using a degradable crosslinker such as a zwitterionic carboxybetaine disulfide cross-linker makes them completely degradable.[227]

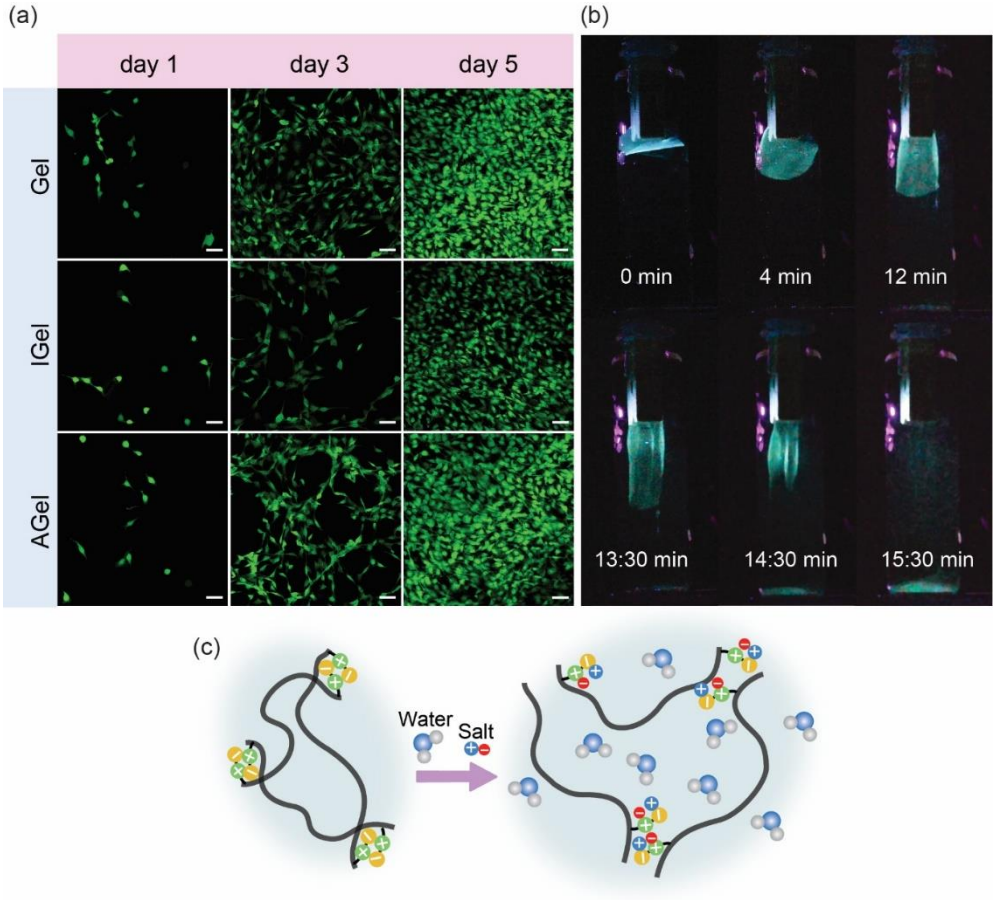

Figure 4-9. Biocompatibility of hydrogel nanocomposites. a) Proliferation of the incubated Fibroblast cells with Gel, IGel, and AGel samples monitored by fluorescent microscopy over 5 days. Scale bars are 50 µm. b) On-demand degradation of GelWC in 10 wt% NaCl solution. c) Schematic of the degradation of GelWC in a salt solution.

4.10 Soft Robotic Applications

After demonstrating programmable shape-morphing, self-healing, and biocompatibility of our hydrogel, we designed a pH-responsive miniature gripper as a proof-of-concept of its tethered robotic applications (**Figure 4-10a**). The gripper was made by applying the cut-and-paste approach to attach two strips (5 mm × 30 mm) of AGel in which the direction of alignment was perpendicular to the long axis. The gripper was used to grab light spherical cargo by rolling the gripper arms around it when triggered by increasing the pH. After transferring the cargo to a new location, the gripper arms were opened by decreasing the pH, and the cargo was released (**Figure 4-10a**). Due to the softness of the gripper arms, they can also wrap around irregular and soft objects. It is important to note that in this

experiment, the hydrogel grippers prevent the lateral movement of soft and light cargo during transport, but do not play a key role in load bearing in the normal direction against gravity.

To test the applicability of our hydrogels in an untethered robotic application, we also fabricated a miniature robot that could be remotely navigated to transfer a very light cargo through a confined flooded space similar to a maze. To benefit from a smaller pitch, or more turns, in a helix, we made our untethered robot from a strip of AGel cut in a way that the angle between the CNC alignment and its long axis is around 60°. To grab the cargo, the soft robot twists around it at high pH, and lowering the pH results in opening the twists and releasing the cargo. We attached a patch of IGel prepared by magnetic CNC (MCNC) instead of CNC (IGelm) to the robot to enable remote navigation (**Figure 4-10b**). MCNCs were prepared by co-precipitation of Fe^{2+} and Fe^{3+} ions on CNC (**Figure 4-11a**). MCNC nanoparticles exhibit a typical superparamagnetic behavior with extremely small hysteresis loops and coercivity (**Figure 4-11b**). IGelm showed a lower magnetization saturation compared to MCNC due to the dilution of the magnetic nanoparticles in hydrogel (**Figure 4-11b**). This patch enables the magnetic navigation of the robot through the maze using a strong permanent magnet from outside of the workspace. When the robot reaches the confined walls, we increase the pH of the environment to twist the robot and grab the cargo. The robot can then be moved through the maze and finally release the cargo by returning to its original shape after increasing the pH, as shown in **Figure 4-10c**.

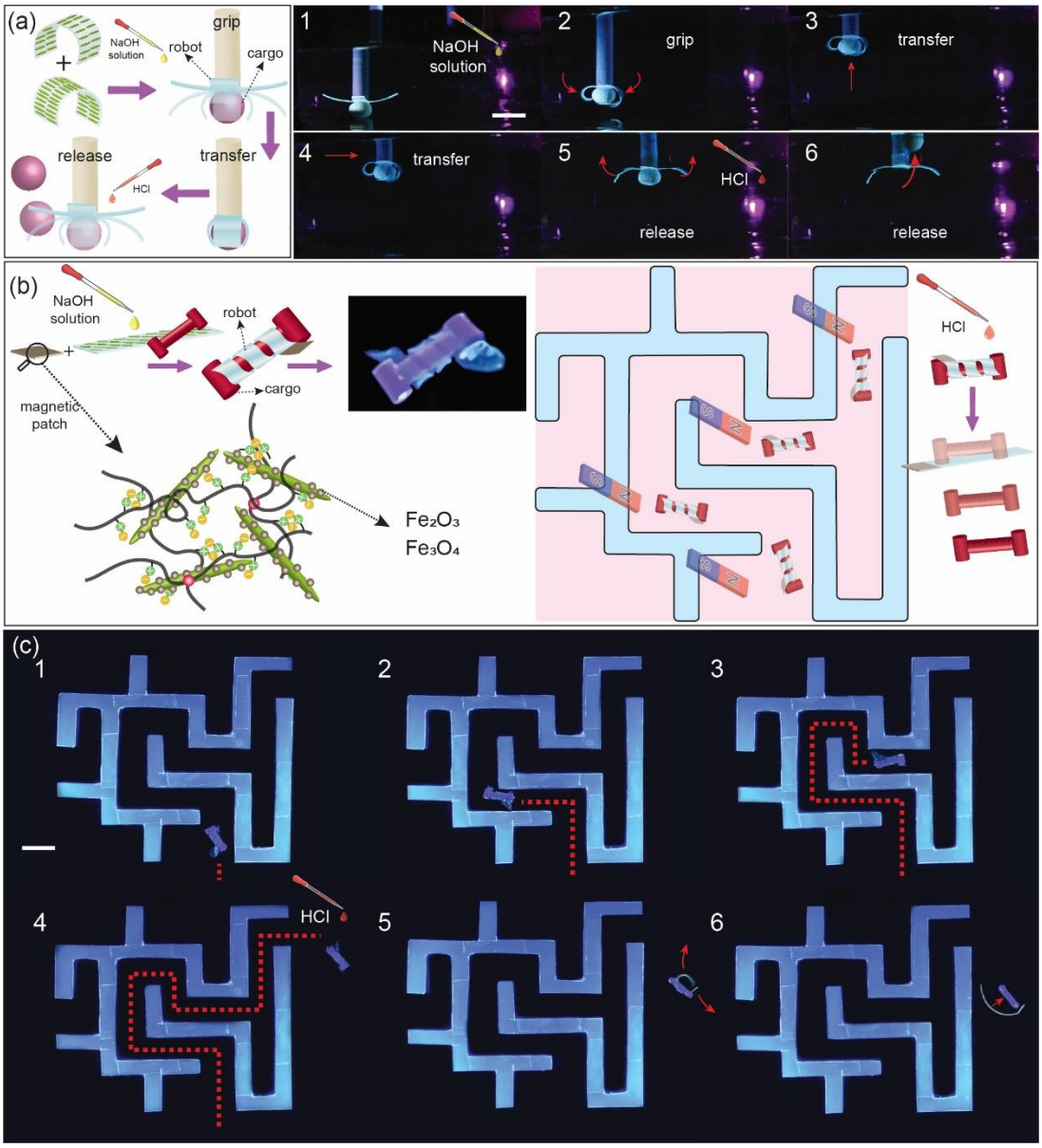

Figure 4-10. Soft robotic applications of anisotropic hydrogel nanocomposites. A micro-gripper developed by a cut-and-paste strategy that grabs a spherical cargo by rolling its arms triggered by increasing the pH. After transferring the cargo to a new location the gripper arms are opened and the cargo is released by decreasing the pH. Scale bar is 10 mm. b) Schematic of a micro-robot transferring a light cargo by twisting around it triggered by increasing the pH. The micro-robot can be remotely navigated and steered by a magnet. c) A micro-robot transferring an I-shaped cargo by twisting around it triggered by increasing the pH. The micro-robot is remotely navigated and steered by a magnet. Decreasing the pH triggers the opening of the micro-robot and the release of the cargo. The scale bar is 10 mm.

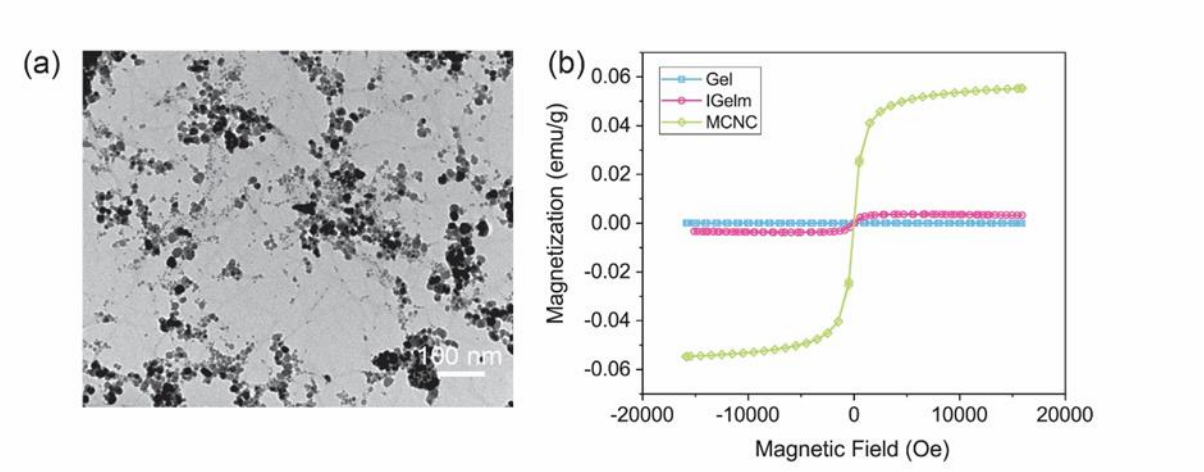

Figure 4-11. a) TEM image of MCNCs. The scale bar is 100 nm. b) VSM of Gel, IGelm, MCNC.

4.11 Concluding Remarks

As a concluding remark, we have successfully synthesized programmable stimuli-responsive zwitterionic hydrogels through a one-step photopolymerization process. By modifying the hydrogel with sustainable high aspect ratio CNC particles, we were able to achieve structural anisotropy under unidirectional shear flow. By changing the environmental pH as an external stimulus, we were able to program the shape-morphing mode of the planar hydrogel strips, providing a wide range of opportunities for shape-changing applications. Furthermore, the hydrogel's outstanding self-healing characteristics allow for complex shape-change profiles using a cut-and-paste approach to attach additional hydrogel strips with differential anisotropic structures.

This all-in-one material, coupled with demonstrated biocompatibility, makes it suitable for soft robotic applications, particularly in the design of intelligent biomedical microrobots. However, the pH-dependent actuation may limit the use of our soft robots in real-world biomedical applications, as changing the environmental pH could be beyond the tolerated physiological conditions of the biological organs. Therefore, we plan to expand the response portfolio of our hydrogel by introducing methods to diversify its applications. Thanks to the zwitterionic moieties, the hydrogel can serve as a bimodal actuator responsive to both pH and ionic strength. We will introduce another approach to program the shape-change behavior of our hydrogels by designing an integrated device that will undergo a

predefined shape change by changing the ionic concentration of the surrounding environment. The next chapter will focus on the methodology and applications of the bilayer hydrogel system.

Chapter 5
Self-Healing Shape-Morphing Zwitterionic Hydrogel Bilayers for Soft Robotics

5.1 Introduction

Responsive zwitterionic hydrogel bilayers possess a variety of properties that make them well-suited to be used in soft robotic devices. Their high flexibility and stimuli-responsive capabilities, which enable them to morph in response to external stimuli such as changes in temperature or pH, make them interesting for use as grippers, locomotives, and other sophisticated shape-morphing constructs.[30,215,275] In this chapter, we aim to introduce a zwitterionic bilayer hydrogel with a combination of desired properties for constructing robotic devices. We utilize a stacking strategy to introduce macrostructural anisotropy to our hydrogel constructs. This strategy offers a versatile method to program the shape-morphing and provides more control for the design of robotic actuators compared to introducing microstructural anisotropy, which was introduced as the shape-change programming tool in the previous chapter. To the best of our knowledge, zwitterionic chemistry has been rarely utilized in developing bilayer constructs for soft robotic applications. In this chapter, we elaborate on the concept of zwitterionic bilayer hydrogels for soft robotic applications by showcasing the use of our fabricated bilayer constructs for simple robotic functions, such as gripping and transporting objects in confined and flooded environments.

5.2 System Concept

The technique we reported in Chapter 4 was mainly based on introducing microstructural anisotropy in hydrogels through the directional orientation of the molecules, voids, or particles at the micro-scale. Introducing macrostructural anisotropy is another approach to programming the shape-morphing of hydrogel actuators. This approach differs from the previous approach, discussed in Chapter 4 since it mainly deals with the introduction of heterogeneity in the physiochemical properties of the construct at the macro-scale. This method relies on the integration of two stimuli-responsive hydrogel layers with different physiochemical and geometrical properties, which could result in more intricate deformation profiles. For example, one layer could exhibit expansion upon exposure to stimuli while the other layer could show shrinkage in the presence of the same stimuli. Integration of such reverse actuation profiles in a single construct result in the more pronounced differential swelling of the construct along the

thickness, which leads to anisotropic out-of-plane shape change. This method is a robust approach to program complex actuation and tailors the morphing mode of soft constructs. Thanks to the inherent self-healing properties of zwitterionic/acrylate hydrogels, they have excellent potential to be used in fabricating such constructs (**Figure 5-1a**). In our design, we will leverage the chemistry of a random copolymer of 3-dimethyl (methacryloyloxyethyl) ammonium propanesulfonate (DMAPS) and methacrylic acid (MAA) in an aqueous environment to achieve self-healing and actuation properties. We expect that the incorporation of MAA improves the mechanical properties of the hydrogel through intra- and inter-molecular hydrogen bonding and hydrophobic associations provided by hydroxyl and methylene groups in the MAA chemical structure (**Figure 5-1b**).[186,187,239,276,277] The zwitterionic network formed by DMAPS should also demonstrate remarkable self-healing properties due to the dynamic electrostatic interactions between oppositely-charged groups. As we reported in Chapter 4, following other reports in the literature, DMAPS-co-MAA has also shown responsiveness to temperature, ionic strength, and pH, making it a promising material for designing multi-modal stimuli-responsive actuators for soft robotic applications.[241–243,278,279] The outstanding self-healing properties of DMAPS-co-MAA make it suitable for a cut-and-paste strategy to program complex stimuli-triggered shape deformations using the bilayer approach. The fabricated bilayer can be used to design functional micro-robots such as grippers and end-applicators for remotely controlled applications. Optimizing the mechanical properties, self-healing, and actuation of the fabricated hydrogel for soft robotic applications requires a systematic investigation of the hydrogel precursors with different chemical compositions. In this chapter, we show the results of our systematic study on the synthesis of different DMAPS-MAA hydrogels and bilayer constructs thereof, with a focus on their applicability in soft robotic applications.

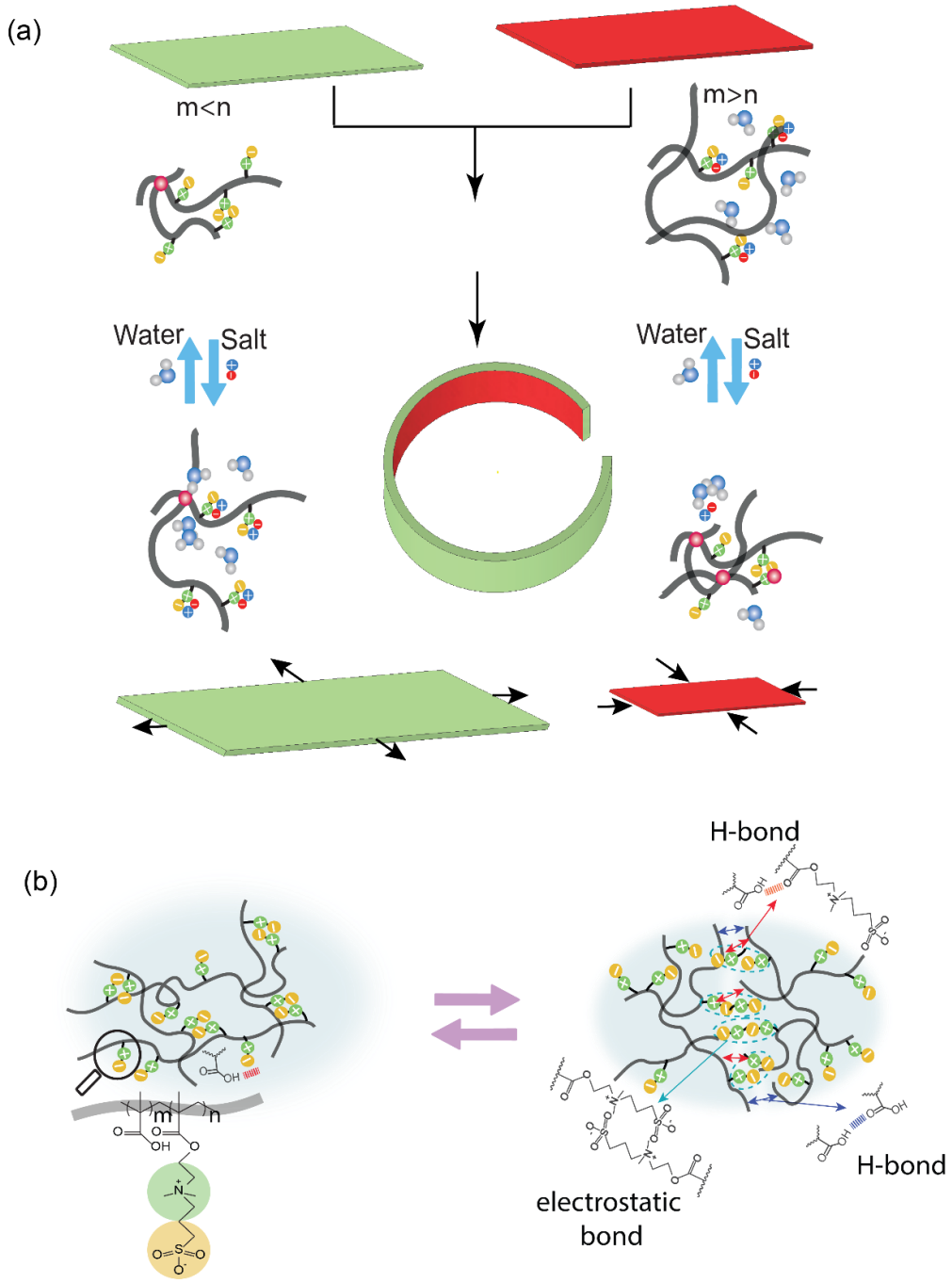

Figure 5-1. Concept of synthesizing bilayer hydrogels. a) Shape-change programming of the hydrogel. Schematic representation of the hydrogels' reversible expansion/shrinkage mechanism. b) The chemical structure of the hydrogel components. Schematic of the electrostatic cross-linking and self-healing mechanism of the hydrogel.

5.3 DMAPS-MAA Hydrogels

The self-healing and mechanical properties of physically cross-linked hydrogels were investigated after polymerizing hydrogel precursors with different DMAPS: MAA weight ratios. The fabricated hydrogels are named SBMA1 to SBMA4, in which the weight ratio of DMAPS to MAA varies from 1:2 to 3:1 (**Table 5-1**). The stress-strain behavior of the hydrogels, **Figure 5-2a**, shows that increasing DMAPS concentration in the formulation reduces Young's modulus and tensile strength monotonically. This is not the case for the elongation at break as it decreases first by increasing DMAPS concentration then it decreases by further increasing the zwitterionic content. The super-hydrophilicity of DMAPS increases the water uptake of the hydrogels with higher DMAPS concentration which causes a reduction of the mechanical properties.[280,281] However, after a critical DMAPS concentration (above 50 wt.% in the monomer mixture), the density of the physical network increases significantly, increasing the elongation at break. Thus, SBMA4 hydrogels are soft yet possess large elongation at break.

Table 5-1. Synthesized hydrogel compositions.

DMAPS: MAA Weight Ratio	Name
1:2	SBMA1
1:1	SBMA2
2:1	SBMA3
3:1	SBMA4

As shown in **Figure 5-2b**, SBMA3, and SBMA4 reach an equilibrium swelling after being exposed to water for about 1 hour; however, SBMA1 and SBMA2 do not exhibit equilibrium swelling. This observation can be attributed to the difference in the network strength of the studied hydrogels. Sulfobetaine, the zwitterionic monomer used in fabricating the hydrogels, is the main contributor to the formation of the hydrogel's physical network due to the electrostatic interaction between the oppositely-charged moieties in its structure. In SBMA3 and SBMA4 hydrogels, sulfobetaine is the dominant component; hence, these hydrogels have a denser and stronger network of physically cross-linked chains. In SBMA1 and SBMA2 hydrogels, methacrylic acid is the dominant component. A lower content of sulfobetaine results in a reduction of electrostatic interactions, which leads to a weak

hydrogel network. Therefore, SBMA1 and SBMA2 hydrogels fail to withstand swelling and start degrading after being exposed to water over time.

We then studied the self-healing properties of the four hydrogel formulations at the macroscale. For that, the self-healing-time-study experiment was conducted to determine the effect of contact time and chemical composition on the self-healing properties of the hydrogels. Strips of different hydrogel compositions were cut in half, followed by bringing the pieces to contact for different periods. The effect of time on the self-healing properties of SBMA1 and SBMA4 samples is shown in **Figure 5-2c**. One can observe a gradual improvement in healing efficiency for both specimens; however, the healing efficiency is significantly higher for the SBMA4 hydrogel, where the broken hydrogel exhibits full recovery of mechanical properties four hours after healing. We attribute this to the higher amount of electrostatic interactions in the SBMA4 hydrogel compared to the SBMA1 counterpart (the results of the self-healing experiment for the SBMA2 and SBMA3 samples are reported in **Figure 5-2d**).

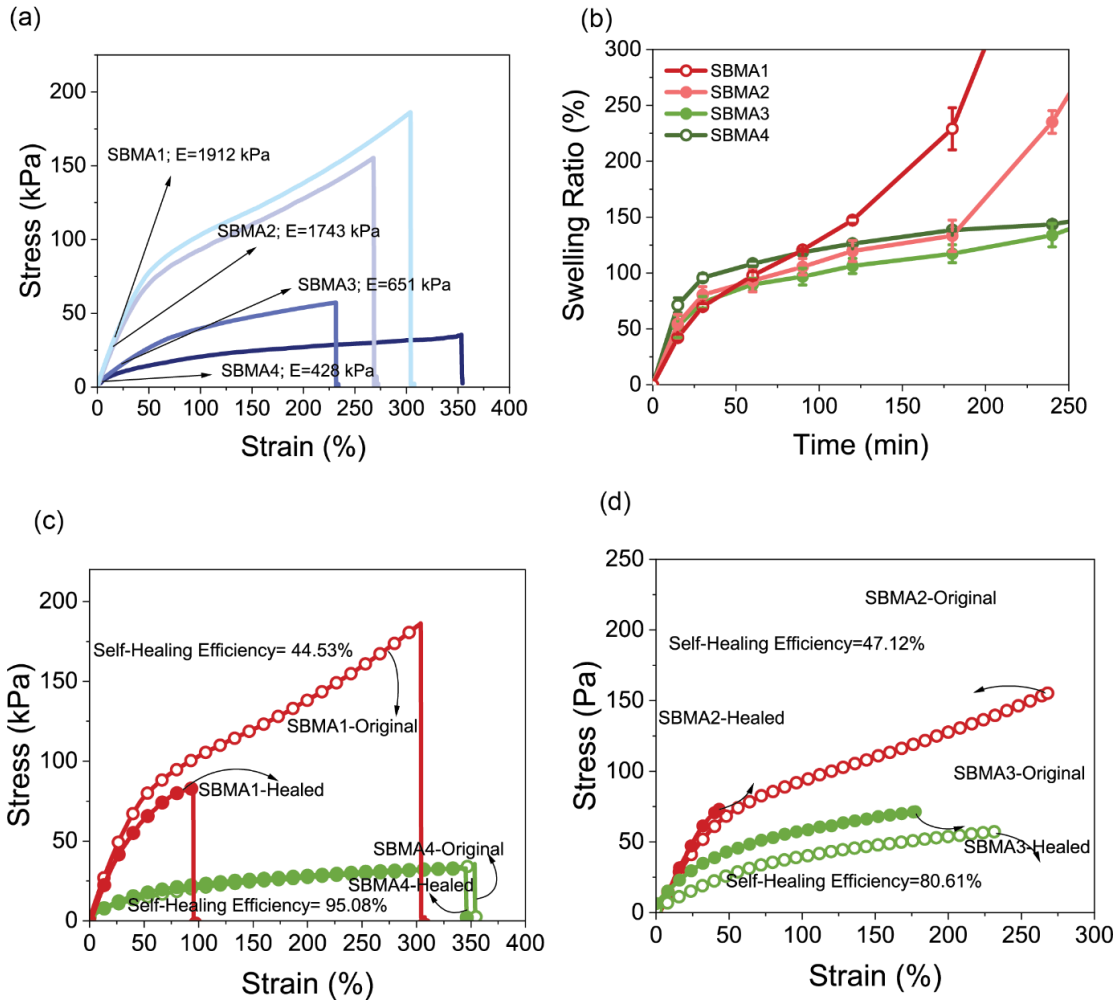

Figure 5-2. Hydrogel selection through characterization. a) Stress-strain behavior of the hydrogels. b) Monitoring the swelling behavior of the hydrogels in water. SBMA1-2 starts degradation after around 1 hour while SBMA3-4 shows stability after 4 hr. c) Self-healing efficiency of SBMA1 and SBMA4 over time. d) Self-healing efficiency of SBMA2 and SBMA3 hydrogels over time.

Cyclic step-strain mechanical testing was used to investigate the self-healing behavior of hydrogels at the microscale and their elastic response under a controlled strain regime. In all studies, we frequently toggled the applied strain between 1% and 100%, corresponding to the linear and non-linear viscoelastic regions obtained from the amplitude sweep test shown in **Figure 5-3a,b**. Both hydrogel compositions exhibit a linear viscoelastic region in which the microstructure of the hydrogels is preserved, and the elastic and loss moduli possess constant values. Additionally, G' is greater than G" in the entire range of applied strains within this region. Through this method, we can evaluate the

recovery of the hydrogels' mechanical properties at the microscale following the network rupture at high strain. As shown in **Figure 5-3c,d**, both SBMA1 and SBMA4 hydrogels demonstrate a gel network (G′ greater than G″) in the range of linear viscoelastic strains (shear strains below 1%). For SBMA1, in shear strains above the linear viscoelastic threshold (shear strains beyond 100%), G′ dropped immediately and became smaller than G″, indicating hydrogel network dissociation. The ruptured network did not recover after the reduction of strain given the lower concentration of DMAPS, which causes the reduction of electrostatic interactions and limits the reconstruction of the hydrogel network. In contrast, SBMA4 exhibits full structural recovery, confirmed by the recovery of the mechanical properties at the beginning of the second cycle.

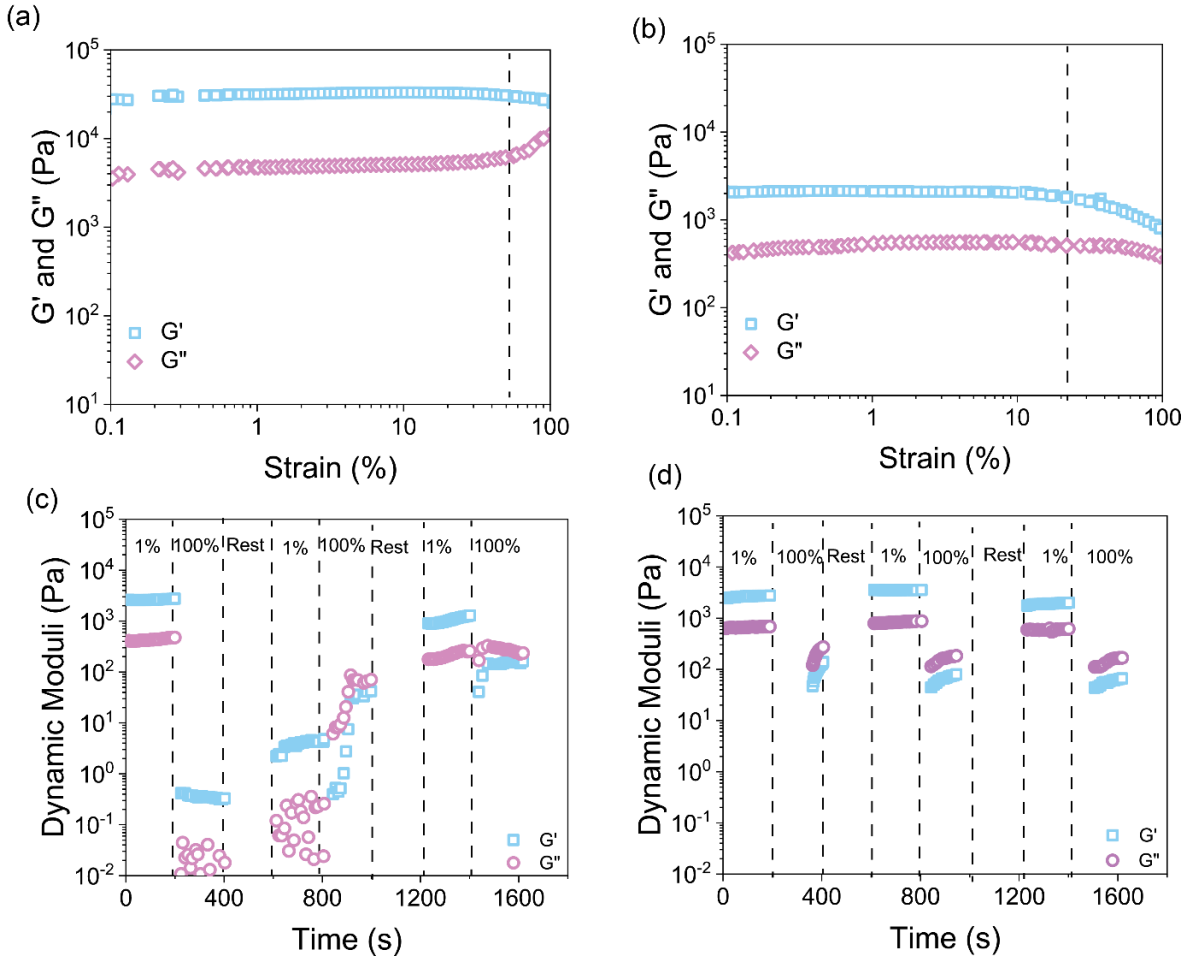

Figure 5-3. Rheology test in the amplitude sweep mode indicates a) The formation of a strong gel and the linear viscoelastic region of the SBMA1 sample. b) The formation of a strong gel and the linear viscoelastic region of the SBMA4 sample. c) Rheological behavior of SBMA1 in the step-strain mode, which shows the lack of self-healing properties. c) Rheological behavior of SBMA4 in the step-strain mode, which shows self-healing properties in a cyclic regime.

A crucial capability of hydrogels for designing functional devices is to exhibit a reversible response to specific external cues, such as a change in ionic strength, in the form of volume changes. In this study, the swelling and deswelling mechanisms of the proposed hydrogels in response to changes in the ionic strength of the environment were investigated. As shown in **Figure 5-1a**, hydrogels with high zwitterionic content expand in saline solution due to charged group neutralization. This leads to increased water absorption. However, hydrogels with high acrylate content shrink as water is expelled to establish osmotic equilibrium.

Figure 5-4 shows the expansion coefficient $((L-L_0))/L_0$, where L_0 and L are the initial and post-swelling lengths of the samples, respectively) of the SBMA1-4 samples in 2M sodium chloride (NaCl) solution. After swelling the samples in DI water for about 2 hours, the hydrogel specimens were placed in the 2M NaCl solution. Among the hydrogels, SBMA1 and SBMA2 showed shrinkage, while SBMA3 and SBMA4 hydrogels showed an immediate expansion upon exposure to the saline solution. The oppositely-charged ions in the surrounding saline neutralize some of the $–NH_4^+$ and $–SO_3^-$ groups of DMAPS, resulting in a loose hydrogel network due to the reduction of the electrostatic interactions, which manifests in increased water uptake. However, for the MAA-rich hydrogels, water expels out from the network to reduce the ionic concentration outside the hydrogel network and to provide an equilibrium through the osmotic effect. This phenomenon overtakes the impact of the partial collapse of the zwitterionic network upon exposure to the saline and results in the volume shrinkage of the SBMA1 and SBMA2 hydrogels.[282–286]

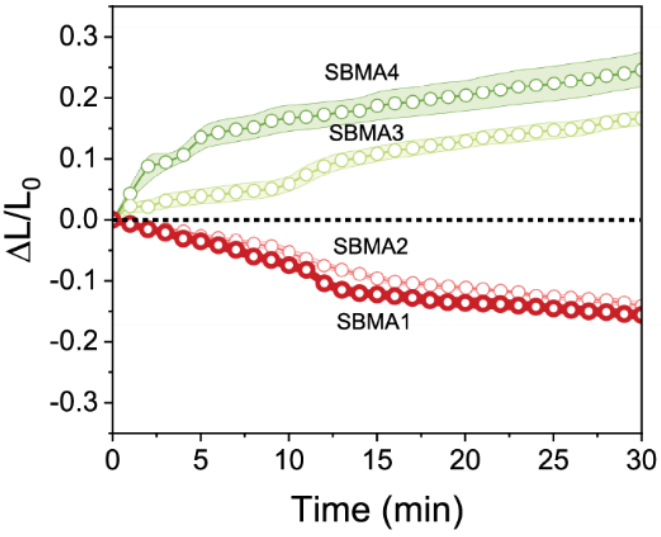

Figure 5-4. Dimensional change of the hydrogels upon exposure to the saline solution over time.

To evaluate the efficiency of self-healing between SBMA1 and SBMA4, which is necessary for the successful fabrication of bilayers, we first made two hydrogel strips of SBMA1 and SBMA4 with dimensions of 25 mm × 10.5 mm, which were equilibrated in water for 2 hours. Then, we cut each strip in two halves and combined them by pressing them laterally with a contact area of 100 mm² under constant pressure (**Figure 5-5a**). After 6 hours of healing, the stress-strain behavior of the healed bilayer hydrogel was evaluated, and remarkable elongation was observed (**Figure 5-5b**). Compared to the stress-strain behavior of the healed SBMA4 hydrogel, the elastic modulus of the bilayer made of SBMA1 and SBMA4 strips has improved slightly (around 4 kPa, see Figure **5-2c**), which can be attributed to the contribution of the stiffer SBMA1 hydrogel. However, the elongation at the break of the bilayer hydrogel decreased by 200% compared to the SBMA4 hydrogel, although it is still significant for simple robotic applications. This drastic decrease can also be attributed to the contribution of the SBMA1 strip, which has considerably less zwitterionic content, leading to reduced chain dynamics and restricted interdiffusion of polymer chains in the contact area.

5.4 Chemically Cross-Linked DMAPS-MAA Hydrogels

Utilizing hydrogels for soft robotics requires long-term underwater stability. During the actuation of constructs in the saline solution, the ions in the surrounding environment disrupt the electrostatic attraction between the zwitterionic moieties, causing the excessive swelling and eventual degradation of the SBMA4 hydrogel after 20 minutes. SBMA1 hydrogels start degrading after being kept in water for 50 minutes. Although both SBMA1 and SBMA4 hydrogels demonstrated the desired mechanical properties and self-healing efficiency, they dissociated upon immersion in water and saline solution after 20 mins, which limits their practical applications (**Figure 5-5c,d**). To address the issue of degradation in physically cross-linked DMAPS-MAA hydrogels, we added small amounts of N, N'-methylene bis (acrylamide) (BIS) as a chemical crosslinker. This approach resulted in hydrogels that could withstand degradation for at least several hours and multiple cycles. One shortcoming of this strategy was the reduction of the elastic modulus and the elongation-at-break of healed chemically-crosslinked hydrogel strips, despite the low BIS: monomer molar ratio (1:400) (**Figure 5-5b)**. This is likely due to the reduced water retention capability of the hydrogels, which causes expelled water to accumulate on the contact surface of the strips and interfere with the adhesion of the layers. Therefore, the amount of chemical cross-linker was kept minimal since it adversely affects the self-healing

efficiency of the hydrogels, which is crucial for integrating hydrogel strips into a bilayer construct by reducing the mobility of the chains.

5.5 Chemically Cross-Linked DMAPS-MAA Nanocomposite Hydrogels

The addition of CNC nanoparticles to the hydrogel formulation could remedy this problem by increasing the hydrophilicity of the chemically-crosslinked hydrogel and enhancing the elastic modulus, elongation, and degradation resistance. The formulation was modified by replacing water with a dilute CNC solution (3 wt.% in water, see Materials and Methods for details). The proposed CNC concentration is below the threshold of the CNC liquid crystalline phase formation (4 wt.%) and the hydrogel precursor is dilute enough to be injected into the cell. The polymerized stripes demonstrated relatively high self-healing efficiency (58.42% for SBMA4 and 36.89% for SBMA1 hydrogels) while still stable in the aquatic environment (**Figure 5-5b-d**). Once CNC is added to the formulation, the hydrophilicity of the hydrogel increases, which prevents surface water accumulation by retaining the moisture inside the structure. Compared to its chemically cross-linked counterpart, the elongation of the modified nanocomposite hydrogel was improved by 40% (**Figure 5-5b**).

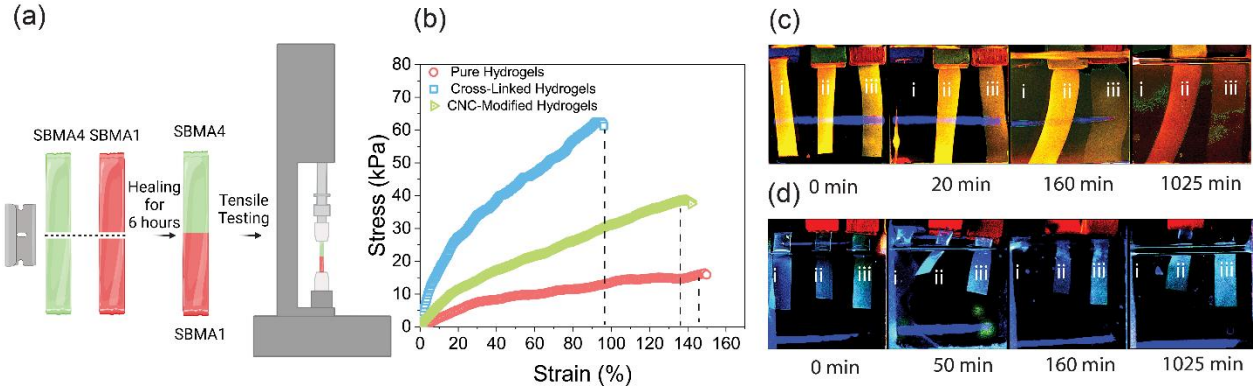

Figure 5-5. a) Schematic representation of the mechanical test procedure. b) Comparison of the mechanical behavior of the unmodified, cross-link-modified, and CNC-modified hydrogels. c)Degradation profile of the SBMA4 hydrogels in saline solution. d) Degradation profile of the SBMA1 hydrogels in water. Stripes labeled with i, ii, and iii represent pure, chemically cross-linked, and chemically cross-linked nanocomposite hydrogels.

5.6 Shape Change Programming

To achieve anisotropic stimuli-triggered shape-morphing, the cut-and-paste strategy has been utilized to fabricate bilayer constructs composed of hydrogel layers with different chemical compositions and thus, actuation behavior.[287–289] The structural gradient along the thickness of the bilayer and the initial geometry of each layer provide a robust toolbox to program shape-morphing. Given the excellent mechanical properties and acceptable degradation resistivity, the bilayer structures in our work were made by integrating chemically cross-linked CNC-containing SBMA1 and SBMA4 nanocomposite hydrogels (called Gel1 and Gel4 afterward). The modified bilayer was used for further investigations in this study.

For a bilayer made from Gel1 and Gel4, we predict that, upon exposure to the saline solution, the gradient in the chemical composition along the thickness will result in the bending of the construct, given the reverse actuation modes of each layer (**Figure 5-6**).[290] In addition to the mechanical properties of each layer, their initial geometry, such as length, thickness, and attachment angle, plays a significant role in tuning the deformation profile.[291] Indeed, the bilayers' deformation is controlled by a combination of macrostructural anisotropy and the balance of internal residual stress resulting from differential swelling along their thickness. For example, if the long axis of the shrinking strip aligns with the direction of the expanding strip, the bilayer will undergo pure bending (**Figure 5-6**). For such a design, self-healing is crucial for maintaining bilayer integrity.

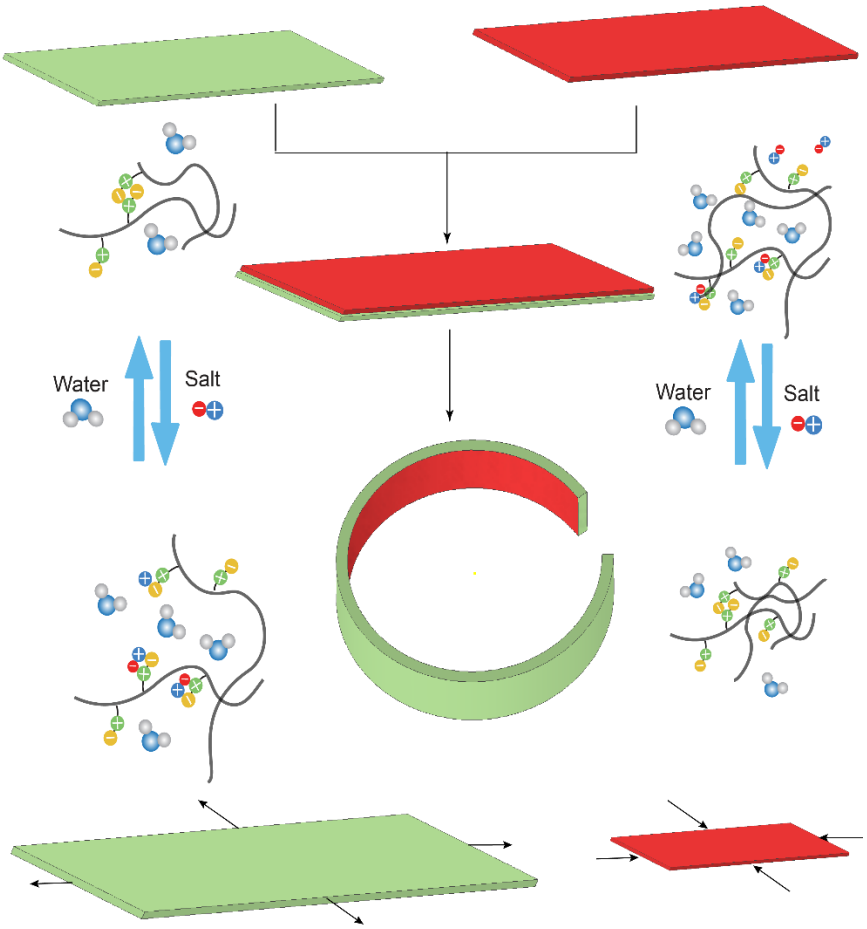

Figure 5-6. Schematic of the expansion and shrinkage mechanisms of the Gel4 and Gel1 hydrogels upon exposure to the saline solution. Differential volume changes along the thickness of the bilayer routs in the predictable deformation.

5.7 Bilayer Actuation

After ensuring the integrity of the bilayer, the controlled shape-morphing was investigated by exposing the bilayer system to a 2M saline solution, followed by swelling in pure DI water to recover the original shape. The predictable swelling and shrinking behaviors of Gel1 and Gel4 provide a host of opportunities for designing devices with complex morphing profiles. To verify this prediction, first, the shape change was triggered by increasing the salinity of the hydrogel environment to 2M, and the pure bending of the initially rectangular bilayer was investigated by monitoring the bending angle over time. Then, the hydrogel was exposed to DI water to recover the original shape, and the releasing angle was monitored over time (**Figure 5-7a**). The bending/releasing angle is the angle between a vertical tangent applied to one edge of the hydrogel and a vector connecting two edges after bending/releasing. The

bilayer demonstrated reversible bending, and the bending direction was controlled by the expanding layer (Gel4). Repeatable shape-changing is another requirement for the functionality of the bilayer for robotic applications. To explore the durability of the hydrogel morphing, the bilayer was exposed to frequent changes in environmental salinity. **Figure 5-7b** shows the reversible bending and unbending of a bilayer of Gel1 and Gel4 for at least five cycles in response to the change in salt concentration.

To further prove the concept of the programmable shape-morphing of bilayers, five bilayer constructs were designed, in which several Gel1 stripes were cut and attached to the Gel4 (substrate layer). The angle between the long axis of Gel1 and Gel4 hydrogels was 0°, 22.5°, 45°, 67.5°, and 90°. Changing the bilayer geometry by increasing the number of attaching layers and altering the attachment angle would introduce further fidelity in tuning the shape-morphing profile of the bilayer. Deviation of the angle of the attaching stripes from the long axis of the substrate strip results in the bilayer twisting and the formation of a helix shape. The pitch of the helix can be adjusted by the angle at which the Gel1 stripes are attached to the Gel4. As shown in **Figure 5-7c-d**, increasing the angle from 22.5° to 67.5° results in an increase in the helical pitch, forming a less compact helix.

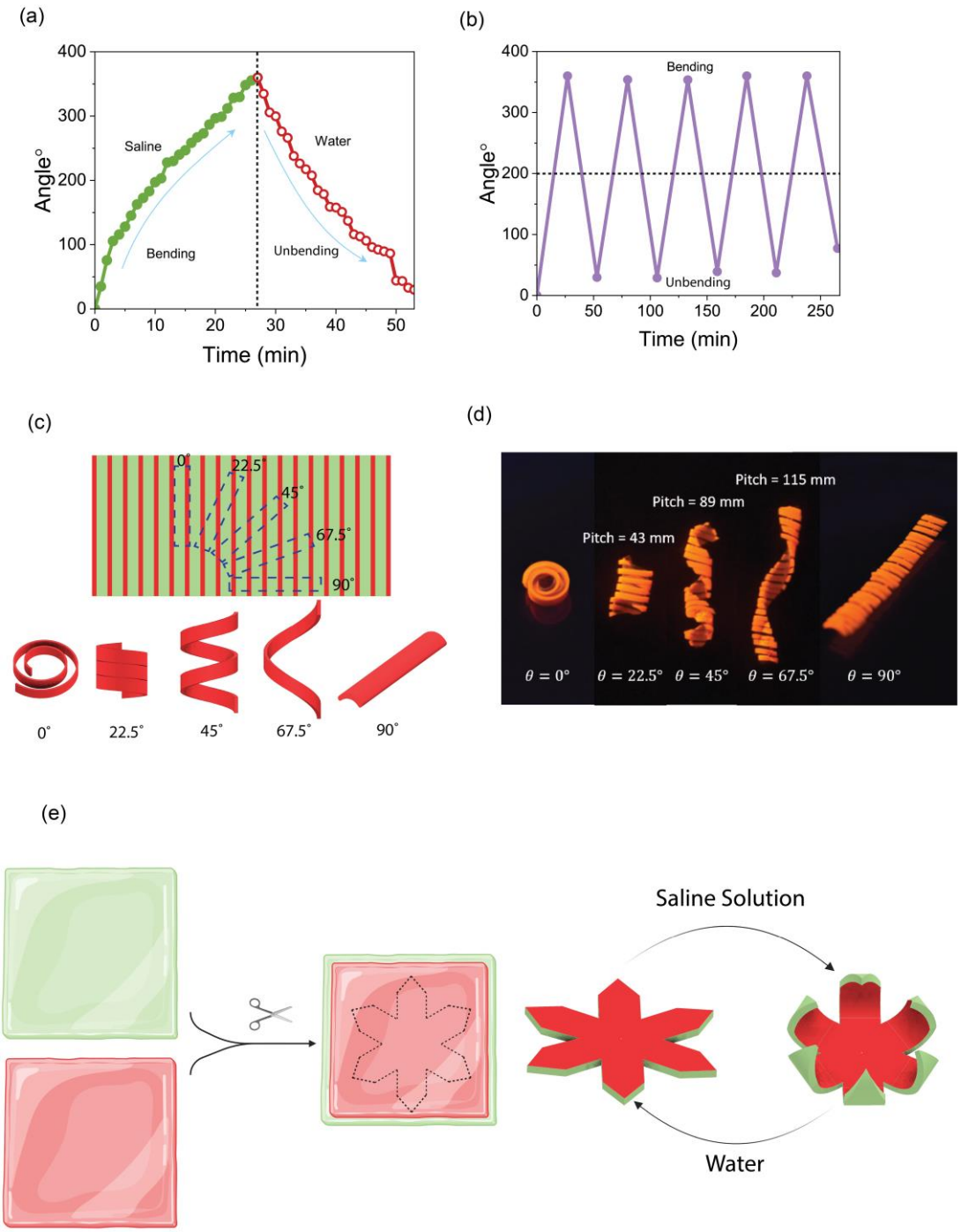

Figure 5-7. Bilayer actuation. a) Quantitative study of the reversible response of the bilayer upon exposure to the saline solution and water. b) Cyclic study of the bilayer's ultimate bending and releasing angles by frequent changes in the environment salinity. c) Schematic representation of controlling the deformation mode by changing the bilayer geometry. d) Obtaining spiral shape-morphing with different pitch sizes by controlling the geometrical parameters of the bilayer hydrogel. e) Schematic representation of the fabrication of end-effectors for robotic applications.

5.8 Robotic Functions

After demonstrating the remarkable properties of our hydrogel bilayer, including programmable shape-morphing, self-healing, and demanded degradation-resistivity, we designed an ionic strength-responsive miniature gripper for untethered robotic applications. The gripper was constructed by joining Gel1 and Gel4 layers, which created arms capable of gripping light, spherical cargo (**Figure 5-7e**). By increasing the salinity, the gripper arms rolled around the cargo, and then we navigated the gripper through the confined paths of a maze, followed by replacing the saline with water to release the cargo (See **Figure 5-8**). We also developed a miniature spiral robot to transport very light cargo through the maze. To achieve a smaller pitch or more turns in the helix, we cut the strips of Gel4 at an angle of around 22.5° between the Gel4 strips and the long axis of the Gel1 substrate. By increasing the salinity, the bilayer twisted around the cargo to pick it up. Then, the designed construct transported the cargo navigated by an external magnetic field, and finally, released the cargo at the end of the path (**Figure 5-9**). In both applications, we incorporated magnetic iron oxide nanoparticles into the precursor to magnetize the Gel1 strips and enable remote navigation.

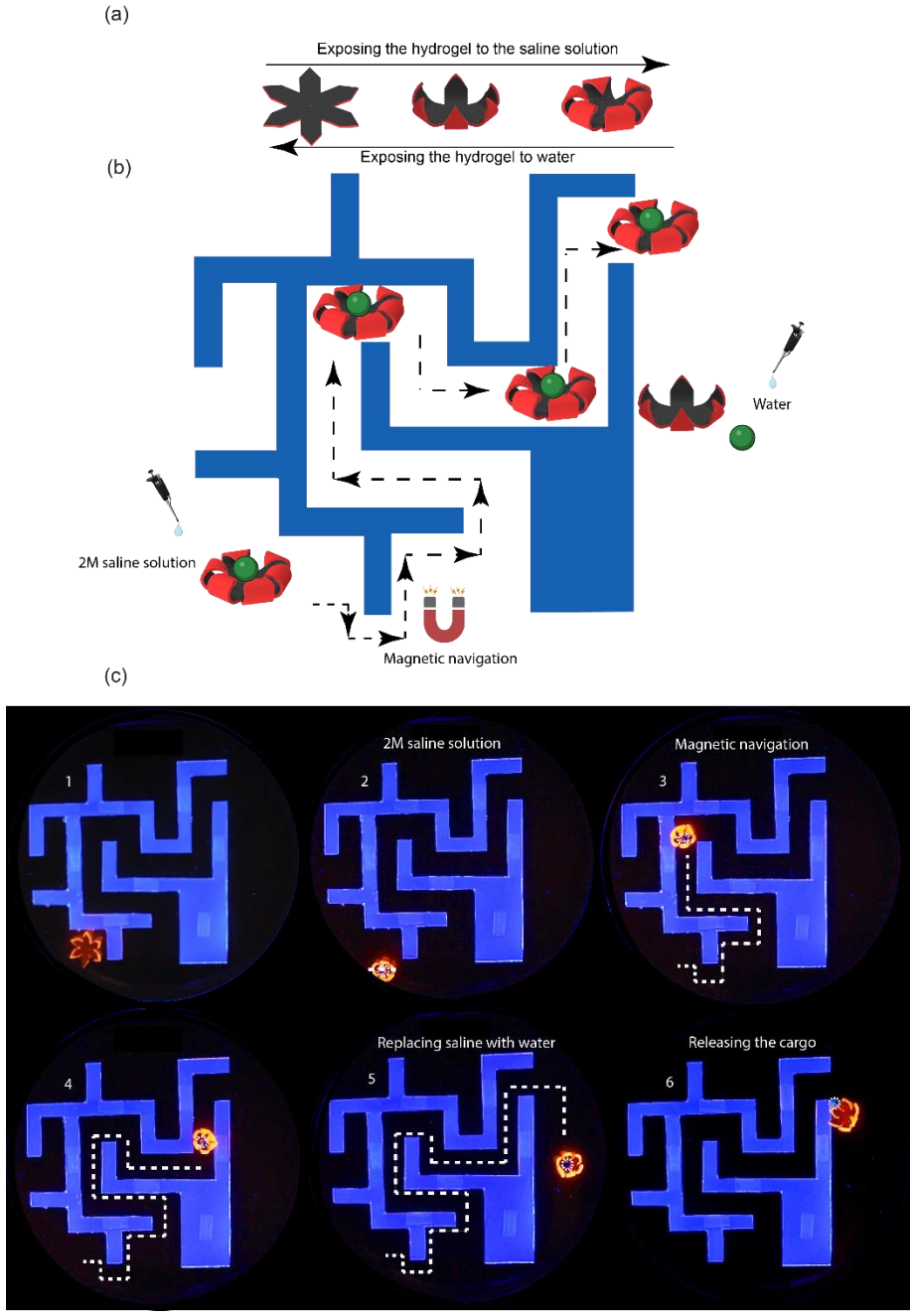

Figure 5-8. a) Schematic of the reversible deformation of a micro-robot triggered by environmental salinity. b) The schematic representation of a micro-robot that can be remotely navigated by a magnet. c) Soft robotic applications of bilayer hydrogels. A micro-gripper developed by a multilayering strategy that grabs a spherical cargo by rolling its arms triggered by increasing the salinity. After transferring the cargo to a new location by magnetic navigation, the gripper arms are opened and the cargo is released by replacing the saline with water.

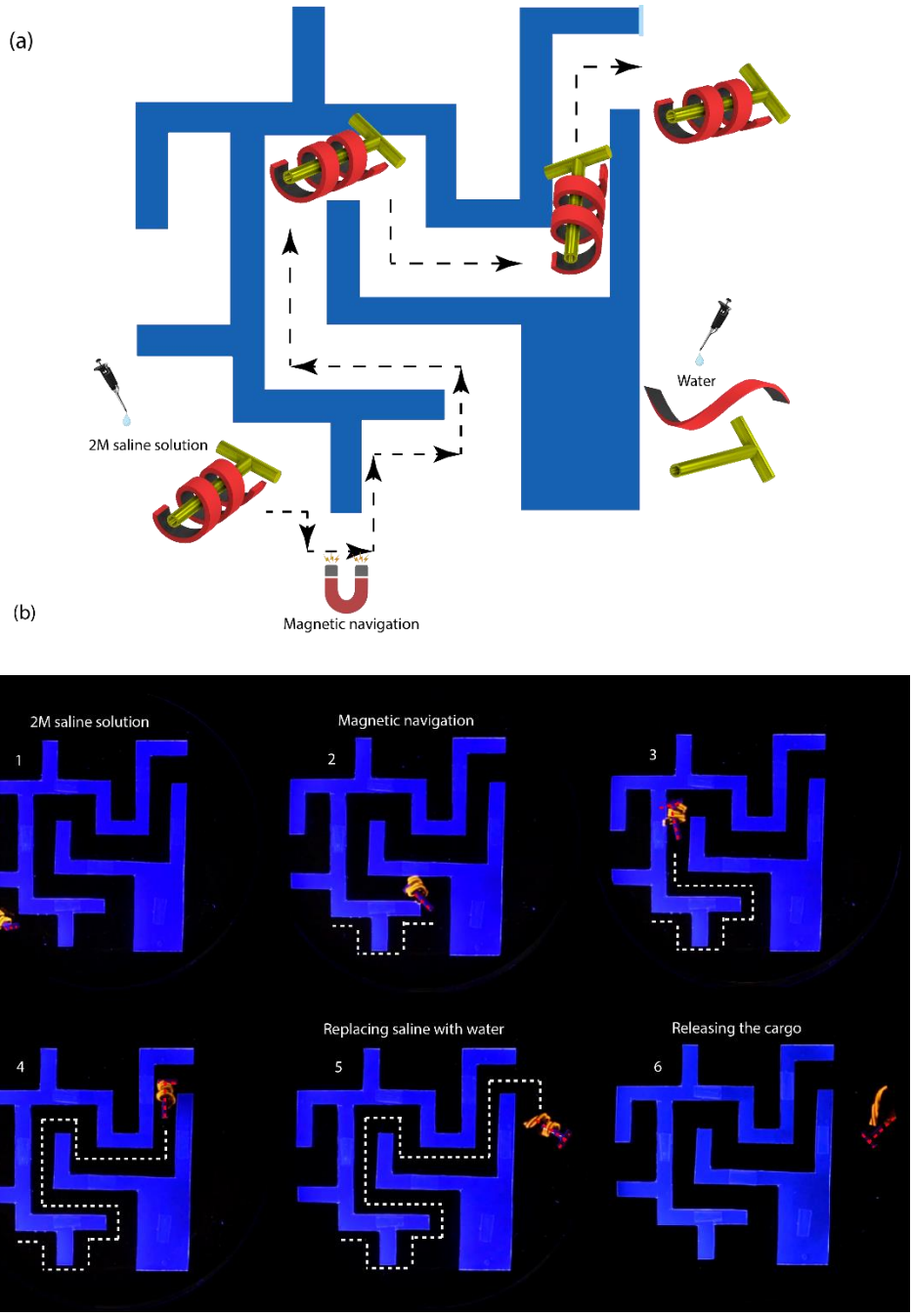

Figure 5-9. a) The schematic representation of a micro spiral swimmer that can be remotely navigated by a magnet. b) The micro-robot rolls around a T-shaped cargo by increasing the salinity. After transferring the cargo to a new location by magnetic navigation, the spiral robot opens up and the cargo is released by replacing the saline with water.

5.9 Concluding Remarks

In summary, we employed a cut-and-paste approach to design bilayer hydrogels with a heterogenous stimuli-response pattern along the thickness, which promotes controllability of the predictable deformation of the soft robot by changing the salinity of the surrounding environment. The bilayer features selective out-of-plane deformations due to the heterogenous physiochemical and mechanical properties and possesses essential requirements for untethered soft robotic applications. To further prove the capability of the designed anisotropic hydrogel for robotic applications, we employed our hydrogel bilayer to fabricate a miniature gripper and a spiral locomotive. These devices enable the transport of lightweight cargo by changing the concentration of the saline environment.

Chapter 6
Challenges and Outlook

6.1 Future Research Direction

Overall, there are several directions for future research to fully realize the potential of our programmable hydrogel systems for advanced robotic applications. One key area is the development of zwitterionic hydrogels with more complex shape-morphing and locomotion modes to enable more sophisticated robotic functions. Another research area is improving the mechanical properties of the hydrogel formulations to support higher load-bearing capacity applications. Furthermore, to enable minimally invasive medical interventions for therapeutic and theranostic applications, there is a need to develop hydrogel-based robotic devices at milli- and micro-scales. This requires the utilization of sophisticated microfabrication techniques. The shear-thinning rheology of the hydrogel precursor, coupled with its photocurable nature, offers opportunities for the development of bio-inks for extrusion additive manufacturing. Stereolithography, direct laser writing, and two-photon polymerization are other additive manufacturing methods at the submillimeter scale that could benefit from a variety of hydrogels, including our system, as inks. The non-cytotoxicity and biocompatibility of the hydrogel precursor offer a host of possibilities for synthesizing cell-laden bio-inks for extrusion and laser-based fabrication. Additionally, the longevity, durability, and on-demand degradability of hydrogel constructs are also important considerations for practical applications. Finally, there is a need to design hydrogel constructs with integrated functions of actuation, sensing, control, and communication to enable multifunctionality in advanced robotic applications. These future research directions will be critical to advancing the field of hydrogel-based soft robotics for biomedical and other applications.

References

[1] G. Z. Yang, J. Bellingham, P. E. Dupont, P. Fischer, L. Floridi, R. Full, N. Jacobstein, V. Kumar, M. McNutt, R. Merrifield, B. J. Nelson, B. Scassellati, M. Taddeo, R. Taylor, M. Veloso, Z. L. Wang, R. Wood, *Sci. Robot.* **2018**, *3*, DOI 10.1126/scirobotics.aar7650.

[2] Y. Dong, L. Wang, N. Xia, Z. Yang, C. Zhang, C. Pan, D. Jin, J. Zhang, C. Majidi, L. Zhang, *Sci. Adv.* **2022**, *8*, DOI 10.1126/sciadv.abn8932.

[3] G.-Z. Yang, J. Bellingham, P. E. Dupont, P. Fischer, L. Floridi, R. Full, N. Jacobstein, V. Kumar, M. McNutt, R. Merrifield, B. J. Nelson, B. Scassellati, M. Taddeo, R. Taylor, M. Veloso, Z. L. Wang, R. Wood, *Sci. Robot.* **2018**, *3*, eaar7650.

[4] S. Robotics, **2018**, *0448*, 2.

[5] P. Sciences, **2009**, *458*, 1121.

[6] S. Palagi, P. Fischer, *Nat. Rev. Mater.* **2018**, *3*, 113.

[7] Y. S. Kim, M. Liu, Y. Ishida, Y. Ebina, M. Osada, T. Sasaki, T. Hikima, M. Takata, T. Aida, *Nat. Mater.* **2015**, *14*, 1002.

[8] A. Nojoomi, H. Arslan, K. Lee, K. Yum, *Nat. Commun.* **2018**, *9*, 3705.

[9] *J. Mater. Chem.* **2022**, *10*.

[10] D. Jiao, Q. L. Zhu, C. Y. Li, Q. Zheng, Z. L. Wu, *Acc. Chem. Res.* **2022**, *55*, 1533.

[11] H. Arslan, A. Nojoomi, J. Jeon, K. Yum, *Adv. Sci.* **2019**, *6*, DOI 10.1002/advs.201800703.

[12] Y. Chang, A. Venault, C. W. Huang, J. Zheng, A. Chinnathambi, S. A. Alharbi, Y. Cheng, *Int. J. Polym. Mater. Polym. Biomater.* **2016**, *65*, 65.

[13] A. Kumar, R. Rajamanickam, J. Hazra, N. R. Mahapatra, P. Ghosh, *ACS Appl. Mater. Interfaces* **2022**, *14*, 56321.

[14] Z. Ding, M. Zhou, Z. Zhou, W. Zhang, X. Jiang, X. Lu, B. Zuo, Q. Lu, D. L. Kaplan, *ACS Biomater. Sci. Eng.* **2019**, *5*, 4077.

[15] J. Ma, S. Lin, Y. Jiang, P. Li, H. Zhang, Z. Xu, H. Wu, P. Lin, J. Breu, W. Gao, C. Gao, *ACS Nano* **2020**, *14*, 2336.

[16] A. Gevorkian, S. M. Morozova, S. Kheiri, N. Khuu, H. Chen, E. Young, N. Yan, E. Kumacheva, *Adv. Funct. Mater.* **2021**, *31*, DOI 10.1002/adfm.202010743.

[17] P. Xue, H. K. Bisoyi, Y. Chen, H. Zeng, J. Yang, X. Yang, P. Lv, X. Zhang, A. Priimagi, L. Wang, X. Xu, Q. Li, *Angew. Chemie - Int. Ed.* **2021**, *60*, 3390.

[18] T. Hiratani, O. Kose, W. Y. Hamad, M. J. Maclachlan, *Mater. Horizons* **2018**, *5*, 1076.

[19] S. Wang, D. P. Maruri, J. M. Boothby, X. Lu, L. K. Rivera-Tarazona, V. D. Varner, T. H. Ware, *J. Mater. Chem. B* **2020**, *8*, 6988.

[20] A. Sydney Gladman, E. A. Matsumoto, R. G. Nuzzo, L. Mahadevan, J. A. Lewis, *Nat. Mater.* **2016**, *15*, 413.

[21] M. Chau, K. J. De France, B. Kopera, V. R. Machado, S. Rosenfeldt, L. Reyes, K. J. W. Chan, S. Fo, E. D. Cranston, T. Hoare, E. Kumacheva, **2016**, DOI 10.1021/acs.chemmater.6b00792.

[22] O. Kose, C. E. Boott, W. Y. Hamad, M. J. Maclachlan, *Macromolecules* **2019**, *52*, 5317.

[23] K. Liu, Y. Zhang, H. Cao, H. Liu, Y. Geng, W. Yuan, J. Zhou, Z. L. Wu, G. Shan, Y. Bao, Q. Zhao, T. Xie, P. Pan, *Adv. Mater.* **2020**, *32*, 1.

[24] W. Hu, G. Z. Lum, M. Mastrangeli, M. Sitti, *Nature* **2018**, *554*, 81.

[25] Z. Ren, W. Hu, X. Dong, M. Sitti, *Nat. Commun.* **2019**, *10*, DOI 10.1038/s41467-019-10549-7.

[26] H. Arslan, A. Nojoomi, J. Jeon, K. Yum, **2019**, *1800703*, DOI 10.1002/advs.201800703.

[27] C. Ma, X. Le, X. Tang, J. He, P. Xiao, J. Zheng, H. Xiao, W. Lu, **2016**, 8670.

[28] W. Zhang, B. Wu, S. Sun, P. Wu, *Nat. Commun.* **2021**, *12*, 4082.

[29] R. Zhou, P. F. Ren, H. C. Yang, Z. K. Xu, *J. Memb. Sci.* **2014**, *466*, 18.

[30] E. SchAnemann, J. Koc, J. F. Karthaüser, O. Ozcan, D. Schanzenbach, L. Schardt, A. Rosenhahn, A. Laschewsky, *Biomacromolecules* **2021**, *22*, 1494.

[31] P. Cabanach, A. Pena-Francesch, D. Sheehan, U. Bozuyuk, O. Yasa, S. Borros, M. Sitti, *Adv. Mater.* **2020**, *32*, 1.

[32] A. W. Feinberg, *Annu. Rev. Biomed. Eng.* **2015**, *17*, 243.

[33] A. Saikia, S. Mazumdar, N. Sahai, S. Paul, D. Bhatia, S. Verma, P. K. Rohilla, *J. Med. Eng. Technol.* **2016**, *40*, 255.

[34] H. Su, X. Hou, X. Zhang, W. Qi, S. Cai, X. Xiong, J. Guo, *Actuators* **2022**, *11*, 1.

[35] N. El-Atab, R. B. Mishra, F. Al-Modaf, L. Joharji, A. A. Alsharif, H. Alamoudi, M. Diaz, N. Qaiser, M. M. Hussain, *Adv. Intell. Syst.* **2020**, *2*, 2000128.

[36] Z. T. H. Tse, Y. Chen, S. Hovet, H. Ren, K. Cleary, S. Xu, B. Wood, R. Monfaredi, *J. Med. Robot. Res.* **2018**, *3*, DOI 10.1142/S2424905X18410064.

[37] C. Heyer, *IEEE/RSJ 2010 Int. Conf. Intell. Robot. Syst. IROS 2010 - Conf. Proc.* **2010**, 4749.

[38] C. Liu, M. Tomizuka, **2018**, 1.

[39] P. A. Lasota, T. Fong, J. A. Shah, *Found. Trends Robot.* **2017**, *5*, 261.

[40] A. N. Sharkawy, P. N. Koustoumpardis, N. Aspragathos, *Soft Comput.* **2020**, *24*, 6687.

[41] T. Fong, I. Nourbakhsh, K. Dautenhahn, *Rob. Auton. Syst.* **2003**, *42*, 143.

[42] C. Majidi, *Soft Robot.* **2014**, *1*, 5.

[43] M. Cianchetti, T. Ranzani, G. Gerboni, T. Nanayakkara, K. Althoefer, P. Dasgupta, A. Menciassi, *Soft Robot.* **2014**, *1*, 122.

[44] F. Connolly, P. Polygerinos, C. J. Walsh, K. Bertoldi, *Soft Robot.* **2015**, *2*, 26.

[45] J. Wang, A. Chortos, **2022**, *2100165*, DOI 10.1002/aisy.202100165.

[46] R. V. Martinez, J. L. Branch, C. R. Fish, L. Jin, R. F. Shepherd, R. M. D. Nunes, Z. Suo, G. M. Whitesides, *Adv. Mater.* **2013**, *25*, 205.

[47] M. Pan, C. Yuan, X. Liang, T. Dong, T. Liu, J. Zhang, J. Zou, H. Yang, C. Bowen, *Adv. Intell. Syst.* **2022**, *4*, 2100140.

[48] S. Kim, C. Laschi, B. Trimmer, *Trends Biotechnol.* **2013**, *31*, 287.

[49] K. W. Kwok, H. Wurdemann, A. Arezzo, A. Menciassi, K. Althoefer, *Proc. IEEE* **2022**, *110*, 871.

[50] M. Runciman, A. Darzi, G. P. Mylonas, *Soft Robot.* **2019**, *6*, 423.

[51] M. W. Gifari, H. Naghibi, S. Stramigioli, M. Abayazid, *Int. J. Med. Robot.* **2019**, *15*, e2010.

[52] Z. Shen, F. Chen, X. Zhu, K. T. Yong, G. Gu, *J. Mater. Chem. B* **2020**, *8*, 8972.

[53] R. Pelrine, R. Kornbluh, Q. Pei, J. Joseph, *Science (80-.).* **2000**, *287*, 836.

[54] G. Y. Gu, J. Zhu, L. M. Zhu, X. Zhu, *Bioinspiration and Biomimetics* **2017**, *12*, DOI 10.1088/1748-3190/12/1/011003.

[55] U. Gupta, L. Qin, Y. Wang, H. Godaba, J. Zhu, *Smart Mater. Struct.* **2019**, *28*, DOI 10.1088/1361-665X/ab3a77.

[56] J. Huang, S. Shian, R. M. Diebold, Z. Suo, D. R. Clarke, *Appl. Phys. Lett.* **2012**, *101*, 122905.

[57] L. An, F. Wang, S. Cheng, T. Lu, T. J. Wang, *Smart Mater. Struct.* **2015**, *24*, 35006.

[58] Z. S. Davidson, H. Shahsavan, A. Aghakhani, Y. Guo, L. Hines, Y. Xia, S. Yang, M. Sitti, *Sci. Adv.* **2019**, *5*, DOI 10.1126/sciadv.aay0855.

[59] A. Poulin, S. Rosset, H. R. Shea, *Appl. Phys. Lett.* **2015**, *107*, 244104.

[60] A. Iannarelli, M. Ghaffarian Niasar, R. Ross, *Appl. Phys. Lett.* **2019**, *115*, DOI 10.1063/1.5115473.

[61] K. Petcharoen, A. Sirivat, *Curr. Appl. Phys.* **2013**, *13*, 1119.

[62] T. Chen, J. Qiu, K. Zhu, J. Wang, J. Li, *Soft Mater.* **2015**, *13*, 210.

[63] J. Zou, G. Gu, *IEEE/ASME Trans. Mechatronics* **2019**, *24*, 36.

[64] F. Chen, K. Liu, Y. Wang, J. Zou, G. Gu, X. Zhu, *IEEE Trans. Robot.* **2019**, *35*, 1150.

[65] F. B. Madsen, A. E. Daugaard, S. Hvilsted, A. L. Skov, *Macromol. Rapid Commun.* **2016**, *37*, 378.

[66] J. Zou, G.-Y. Gu, L.-M. Zhu, *IEEE/ASME Trans. Mechatronics* **2017**, *22*, 51.

[67] B. Bharti, S. Kumar, H.-N. Lee, R. Kumar, *Sci. Rep.* **2016**, *6*, 32355.

[68] B. Jin, H. Song, R. Jiang, J. Song, Q. Zhao, T. Xie, *Sci. Adv.* **2018**, *4*, DOI 10.1126/sciadv.aao3865.

[69] P. Tang, X. Zheng, H. Yang, J. He, Z. Zheng, W. Yang, S. Zhou, *ACS Appl. Mater. Interfaces* **2019**, *11*, 48202.

[70] D. Wang, H. Xu, J. Wang, C. Jiang, X. Zhu, Q. Ge, G. Gu, *ACS Appl. Mater. Interfaces* **2020**,

12, 22146.

[71] T. Xie, *Nature* **2010**, *464*, 267.

[72] T. Xie, *Polymer (Guildf).* **2011**, *52*, 4985.

[73] S. Banisadr, J. Chen, *Sci. Rep.* **2017**, *7*, 17521.

[74] H. Shahsavan, S. M. Salili, A. Jákli, B. Zhao, *Adv. Mater.* **2015**, *27*, 6828.

[75] H. Zeng, P. Wasylczyk, D. S. Wiersma, A. Priimagi, *Adv. Mater.* **2018**, *30*, 1703554.

[76] H. Xing, J. Li, Y. Shi, J. Guo, J. Wei, *ACS Appl. Mater. Interfaces* **2016**, *8*, 9440.

[77] H. Yu, T. Ikeda, *Adv. Mater.* **2011**, *23*, 2149.

[78] M. Rogóż, K. Dradrach, C. Xuan, P. Wasylczyk, *Macromol. Rapid Commun.* **2019**, *40*, 1900279.

[79] H. Zeng, O. M. Wani, P. Wasylczyk, A. Priimagi, *Macromol. Rapid Commun.* **2018**, *39*, 1700224.

[80] C. Ahn, X. Liang, S. Cai, *Adv. Mater. Technol.* **2019**, *4*, 1900185.

[81] T. J. White, D. J. Broer, *Nat. Mater.* **2015**, *14*, 1087.

[82] M. Wang, B.-P. Lin, H. Yang, *Nat. Commun.* **2016**, *7*, 13981.

[83] N. P. Pinchin, C. H. Lin, C. A. Kinane, N. Yamada, A. Pena-Francesch, H. Shahsavan, *Soft Matter* **2022**, *18*, 8063.

[84] L. Dong, Y. Zhao, *Mater. Chem. Front.* **2018**, *2*, 1932.

[85] M. da Cunha, M. G. Debije, A. P. H. J. Schenning, *Chem. Soc. Rev.* **2020**, *49*, 6568.

[86] H. Tian, Z. Wang, Y. Chen, J. Shao, T. Gao, S. Cai, *ACS Appl. Mater. Interfaces* **2018**, *10*, 8307.

[87] H. Jiang, P. Zhang, X. Wang, Y. Gong, *Nano Res.* **2021**, *14*, 1789.

[88] Q. Yang, H. Shahsavan, Z. Deng, H. Guo, H. Zhang, H. Liu, C. Zhang, A. Priimagi, X. Zhang, H. Zeng, *Adv. Funct. Mater.* **2022**, *32*, DOI 10.1002/adfm.202206939.

[89] Y. Guo, H. Shahsavan, M. Sitti, *Adv. Mater.* **2020**, *32*, 1.

[90] M. Zhang, H. Shahsavan, Y. Guo, A. Pena-Francesch, Y. Zhang, M. Sitti, *Adv. Mater.* **2021**, *33*, DOI 10.1002/adma.202008605.

[91] Y. Guo, H. Shahsavan, M. Sitti, *Adv. Opt. Mater.* **2020**, *8*, DOI 10.1002/adom.201902098.

[92] H. Shahsavan, L. Yu, A. Jákli, B. Zhao, *Soft Matter* **2017**, *13*, 8006.

[93] W. Zhang, Y. Nan, Z. Wu, Y. Shen, D. Luo, *Molecules* **2022**, *27*, DOI 10.3390/molecules27144330.

[94] R. A. E. Neufeld, H. Shahsavan, B. Zhao, N. M. Abukhdeir, *Liq. Cryst.* **2018**, *45*, 1010.

[95] J. G. Kim, J. E. Park, S. Won, J. Jeon, J. J. Wie, *Materials (Basel).* **2019**, *12*, DOI 10.3390/ma12193065.

[96] M. Sitti, D. S. Wiersma, *Adv. Mater.* **2020**, *32*, 1906766.

[97] G. Z. Lum, Z. Ye, X. Dong, H. Marvi, O. Erin, W. Hu, M. Sitti, *Proc. Natl. Acad. Sci.* **2016**, *113*, E6007.

[98] M. Li, Y. Wang, A. Chen, A. Naidu, B. S. Napier, W. Li, C. L. Rodriguez, S. A. Crooker, F. G. Omenetto, *Proc. Natl. Acad. Sci.* **2018**, *115*, 8119.

[99] Y. Kim, H. Yuk, R. Zhao, S. A. Chester, X. Zhao, *Nature* **2018**, *558*, 274.

[100] Y. Alapan, O. Yasa, O. Schauer, J. Giltinan, A. F. Tabak, V. Sourjik, M. Sitti, *Sci. Robot.* **2018**, *3*, DOI 10.1126/scirobotics.aar4423.

[101] H. Ceylan, I. C. Yasa, O. Yasa, A. F. Tabak, J. Giltinan, M. Sitti, *ACS Nano* **2019**, *13*, 3353.

[102] J. Rahmer, C. Stehning, B. Gleich, *Sci. Robot.* **2017**, *2*, 1.

[103] D. Rus, M. T. Tolley, *Nature* **2015**, *521*, 467.

[104] X. Liu, J. Liu, S. Lin, X. Zhao, *Mater. Today* **2020**, *36*, 102.

[105] J. Liu, Y. Gao, Y. J. Lee, S. Yang, *Trends Chem.* **2020**, *2*, 107.

[106] Y. Wang, H. Cui, Q. Zhao, X. Du, *Matter* **2019**, *1*, 626.

[107] H. Tan, X. Yu, Y. Tu, L. Zhang, *J. Phys. Chem. Lett.* **2019**, *10*, 5542.

[108] H. Yuk, B. Lu, X. Zhao, *Chem. Soc. Rev.* **2019**, *48*, 1642.

[109] C. Majidi, *Soft Robot.* **2013**, *1*, 5.

[110] F. Wang, B. Chen, L. Wu, Q. Zhao, L. Zhang, *Cell Reports Phys. Sci.* **2020**, *1*, 100011.

[111] Y. Jian, B. Wu, X. Le, Y. Liang, Y. Zhang, D. Zhang, L. Zhang, W. Lu, J. Zhang, T. Chen, *Research* **2023**, *2019*, DOI 10.34133/2019/2384347.

[112] J. Guo, X. Liu, N. Jiang, A. K. Yetisen, H. Yuk, C. Yang, A. Khademhosseini, X. Zhao, S.-H. Yun, *Adv. Mater.* **2016**, *28*, 10244.

[113] Y. Li, Y. Sun, Y. Xiao, G. Gao, S. Liu, J. Zhang, J. Fu, *ACS Appl. Mater. Interfaces* **2016**, *8*, 26326.

[114] M. Elsherif, M. U. Hassan, A. K. Yetisen, H. Butt, *ACS Nano* **2018**, *12*, 5452.

[115] C. Yu, Z. Duan, P. Yuan, Y. Li, Y. Su, X. Zhang, Y. Pan, L. L. Dai, R. G. Nuzzo, Y. Huang, H. Jiang, J. A. Rogers, *Adv. Mater.* **2013**, *25*, 1541.

[116] A. Cherpinski, A. Biswas, J. M. Lagaron, A. Dufresne, S. Kim, M. Buttrum, E. Espinosa, H. N. Cheng, *Cellulose* **2019**, *26*, 7237.

[117] Y. Ahn, H. Lee, D. Lee, Y. Lee, *ACS Appl. Mater. Interfaces* **2014**, *6*, 18401.

[118] D. Kim, S.-K. Ahn, J. Yoon, *Adv. Mater. Technol.* **2019**, *4*, 1800739.

[119] B. Zhang, S. Li, H. Hingorani, A. Serjouei, L. Larush, A. A. Pawar, W. H. Goh, A. H. Sakhaei, M. Hashimoto, K. Kowsari, S. Magdassi, Q. Ge, *J. Mater. Chem. B* **2018**, *6*, 3246.

[120] B. Lu, H. Yuk, S. Lin, N. Jian, K. Qu, J. Xu, X. Zhao, *Nat. Commun.* **2019**, *10*, 1043.

[121] X. Sha, L. Zhao, *J. Nanomater.* **2022**, *2022*, 8503507.

[122] D. Zhang, B. Ren, Y. Zhang, L. Xu, Q. Huang, Y. He, X. Li, J. Wu, J. Yang, Q. Chen, Y. Chang, J. Zheng, *J. Mater. Chem. B* **2020**, *8*, 3171.

[123] Y.-Z. Zhang, K. H. Lee, D. H. Anjum, R. Sougrat, Q. Jiang, H. Kim, H. N. Alshareef, *Sci. Adv.* **2023**, *4*, eaat0098.

[124] M. Krstic, Z. R. Miladinovic, T. Barudzija, A. Mladenovic, E. Suljovrujic, *React. Funct. Polym.* **2022**, *170*, 105140.

[125] Y. Chen, Y. Zhang, H. Li, J. Shen, F. Zhang, J. He, J. Lin, B. Wang, S. Niu, Z. Han, Z. Guo,

Nano Today **2023**, *49*, 101764.

[126] Z. Ren, W. Hu, X. Dong, M. Sitti, *Nat. Commun.* **2019**, *10*, 2703.

[127] H. M. El-Husseiny, E. A. Mady, L. Hamabe, A. Abugomaa, K. Shimada, T. Yoshida, T. Tanaka, A. Yokoi, M. Elbadawy, R. Tanaka, *Mater. Today Bio* **2022**, *13*, 100186.

[128] C. I. Piñón-Balderrama, C. Leyva-Porras, A. S. Conejo-Dávila, E. A. Zaragoza-Contreras, *Polymers (Basel).* **2022**, *14*, DOI 10.3390/polym14235081.

[129] S. Ranganathan, K. Balagangadharan, N. Selvamurugan, *Int. J. Biol. Macromol.* **2019**, *133*, 354.

[130] G. Li, Y. Zhao, L. Zhang, M. Gao, Y. Kong, Y. Yang, *Colloids Surfaces B Biointerfaces* **2016**, *143*, 547.

[131] A. K. Gaharwar, N. A. Peppas, A. Khademhosseini, *Biotechnol. Bioeng.* **2014**, *111*, 441.

[132] F. A. M. M. Gonçalves, A. C. Fonseca, M. Domingos, A. Gloria, A. C. Serra, J. F. J. Coelho, *Prog. Polym. Sci.* **2017**, *68*, 1.

[133] P.-Y. Yeh, P. Kopečková, J. Kopeček, *J. Polym. Sci. Part A Polym. Chem.* **1994**, *32*, 1627.

[134] L. Wu, M. Ohtani, S. Tamesue, Y. Ishida, T. Aida, *J. Polym. Sci. Part A Polym. Chem.* **2014**, *52*, 839.

[135] D. Wang, Y. Tan, L. Yu, Z. Xiao, J. Du, J. Ling, N. Li, J. Wang, S. Xu, **2019**, DOI 10.1002/pc.24754.

[136] M. A. S. Azizi Samir, F. Alloin, A. Dufresne, *Biomacromolecules* **2005**, *6*, 612.

[137] J. A. Pinheiro, N. D. N. Marques, M. A. Villetti, R. D. C. Balaban, *Int. J. Mol. Sci.* **2021**, *22*, 1.

[138] D. Klemm, F. Kramer, S. Moritz, T. Lindström, M. Ankerfors, D. Gray, A. Dorris, *Angew. Chemie Int. Ed.* **2011**, *50*, 5438.

[139] D. Bondeson, A. Mathew, K. Oksman, *Cellulose* **2006**, *13*, 171.

[140] A. H. Tayeb, E. Amini, S. Ghasemi, M. Tajvidi, *Molecules* **2018**, *23*, DOI 10.3390/molecules23102684.

[141] H. Lu, X. Li, M. Zhang, C. Xu, W. Li, L. Wan, *Front. Bioeng. Biotechnol.* **2022**, *10*, 1.

[142] S. Hossain, M. Shahruzzaman, S. F. Kabir, M. S. Rahman, S. Sultana, A. K. Mallik, P. Haque, M. Takafuji, M. M. Rahman, *J. Sci. Adv. Mater. Devices* **2021**, *6*, 254.

[143] T. Jayaramudu, H. U. Ko, H. C. Kim, J. W. Kim, R. M. Muthoka, J. Kim, *Materials (Basel).* **2018**, *11*, 1.

[144] Y. Wu, M. Xia, Q. Fan, M. Zhu, *Chem. Commun.* **2010**, *46*, 7790.

[145] J. Yang, C. R. Han, J. F. Duan, F. Xu, R. C. Sun, *ACS Appl. Mater. Interfaces* **2013**, *5*, 3199.

[146] H. Bai, Z. Li, S. Zhang, W. Wang, W. Dong, *Carbohydr. Polym.* **2018**, *200*, 468.

[147] K. J. De France, K. J. W. Chan, E. D. Cranston, T. Hoare, *Biomacromolecules* **2016**, *17*, 649.

[148] C. Chen, L. Hu, *Adv. Mater.* **2021**, *33*, 1.

[149] D. Zhang, Y. Tang, Y. Zhang, F. Yang, Y. Liu, X. Wang, J. Yang, X. Gong, J. Zheng, *J. Mater. Chem. A* **2020**, *8*, 20474.

[150] M. Jain, R. Fishman, P. Mondal, G. L. Galford, N. Bhattarai, S. Naeem, U. Lall, null Balwinder-Singh, R. S. DeFries, *Sci. Adv.* **2021**, *7*, eabd2849.

[151] L. Zheng, H. S. Sundaram, Z. Wei, C. Li, Z. Yuan, *React. Funct. Polym.* **2017**, *118*, 51.

[152] Y. Zhu, J. Wang, F. Zhang, S. Gao, A. Wang, W. Fang, J. Jin, *Adv. Funct. Mater.* **2018**, *28*, DOI 10.1002/adfm.201804121.

[153] H. Huang, C. Zhang, R. Crisci, T. Lu, H. C. Hung, M. S. J. Sajib, P. Sarker, J. Ma, T. Wei, S. Jiang, Z. Chen, *J. Am. Chem. Soc.* **2021**, *143*, 16786.

[154] Z. Han, S. Chen, L. Deng, Q. Liang, X. Qu, J. Li, B. Wang, H. Wang, *ACS Appl. Mater. Interfaces* **2022**, *14*, 45954.

[155] E. Roels, S. Terryn, F. Iida, A. W. Bosman, S. Norvez, F. Clemens, G. Van Assche, B. Vanderborght, J. Brancart, *Adv. Mater.* **2022**, *34*, 1.

[156] A. Naranjo, C. Martín, A. López-Díaz, A. Martín-Pacheco, A. M. Rodríguez, F. J. Patiño, M. A. Herrero, A. S. Vázquez, E. Vázquez, *Appl. Mater. Today* **2020**, *21*, DOI 10.1016/j.apmt.2020.100806.

[157] M. Liu, S. Zhu, Y. Huang, Z. Lin, W. Liu, L. Yang, D. Ge, *Compos. Part B Eng.* **2021**, *214*, 108748.

[158] S. Terryn, J. Langenbach, E. Roels, J. Brancart, C. Bakkali-Hassani, Q. A. Poutrel, A. Georgopoulou, T. George Thuruthel, A. Safaei, P. Ferrentino, T. Sebastian, S. Norvez, F. Iida, A. W. Bosman, F. Tournilhac, F. Clemens, G. Van Assche, B. Vanderborght, *Mater. Today* **2021**, *47*, 187.

[159] R. Goyal, S. Mitra, *Front. Mater.* **2022**, *9*, 1.

[160] M. Gharakhloo, M. Karbarz, *Eur. Polym. J.* **2022**, *165*, 111004.

[161] F. Mashkoor, S. J. Lee, H. Yi, S. M. Noh, C. Jeong, *Int. J. Mol. Sci.* **2022**, *23*, 1.

[162] D. Y. Zhu, M. Z. Rong, M. Q. Zhang, *Prog. Polym. Sci.* **2015**, *49–50*, 175.

[163] F. Mashkoor, S. J. Lee, H. Yi, S. M. Noh, C. Jeong, *Int. J. Mol. Sci.* **2022**, *23*, DOI 10.3390/ijms23020622.

[164] M. Zhu, J. Liu, L. Gan, M. Long, *Eur. Polym. J.* **2020**, *129*, 109651.

[165] S. R. White, N. R. Sottos, P. H. Geubelle, J. S. Moore, M. R. Kessler, S. R. Sriram, E. N. Brown, S. Viswanathan, *Nature* **2001**, *409*, 794.

[166] F. Fang, Y. Yuan, Y. Wan, J. Li, Y. Song, W.-C. Chen, D. Zhao, Y. Chi, M. Li, C.-S. Lee, J. Zhang, *Small* **2022**, *18*, 2106215.

[167] R. Ke, Z. Lin, H. Zhang, S. Zhou, *J. Phys. Conf. Ser.* **2022**, *2324*, 0.

[168] A.-N. Au-Duong, Y.-C. Hsu, K.-L. Chen, Y.-S. Huang, J.-Y. Lai, Y.-C. Chiu, *Polym. J.* **2022**, *54*, 1331.

[169] Z. Cai, C. Li, D. Zhang, J. Li, L. Gao, *J. Coatings Technol. Res.* **2022**, DOI 10.1007/s11998-022-00703-0.

[170] L. Zhu, Y. Nie, Y. Li, S. Wei, X. Chen, W. Zhao, **n.d.**

[171] Y. Qian, X. An, X. Huang, X. Pan, J. Zhu, X. Zhu, *Polymers (Basel).* **2019**, *11*, DOI 10.3390/polym11050773.

[172] S. Ji, W. Cao, Y. Yu, H. Xu, *Angew. Chemie - Int. Ed.* **2014**, *53*, 6781.

[173] W. Lu, X. Xu, L. Imbernon, J. Zhu, R. Hoogenboom, F. E. Du Prez, X. Pan, *Biomacromolecules* **2020**, *21*, 3308.

[174] R. Guo, Q. Su, J. Zhang, A. Dong, C. Lin, J. Zhang, *Biomacromolecules* **2017**, *18*, 1356.

[175] X.-J. Guo, C.-H. Xue, M. Li, X. Li, J.-Z. Ma, *RSC Adv.* **2017**, *7*, 25560.

[176] J. Canadell, H. Goossens, B. Klumperman, *Macromolecules* **2011**, *44*, 2536.

[177] K. M. Lee, Y. Oh, H. Yoon, M. Chang, H. Kim, *ACS Appl. Mater. Interfaces* **2020**, *12*, 8642.

[178] M. Nakahata, Y. Takashima, A. Harada, *Macromol. Rapid Commun.* **2016**, *37*, 86.

[179] Y. Xu, M. Cui, P. A. Patsis, M. Günther, X. Yang, K. Eckert, Y. Zhang, *ACS Appl. Mater. Interfaces* **2019**, *11*, 7715.

[180] S. Das, P. Martin, G. Vasilyev, R. Nandi, N. Amdursky, E. Zussman, *Macromolecules* **2020**, *53*, 11130.

[181] X. Xu, F. A. Jerca, V. V. Jerca, R. Hoogenboom, *Macromolecules* **2020**, *53*, 6566.

[182] T. Li, X. Hu, Q. Zhang, Y. Zhao, P. Wang, X. Wang, B. Qin, W. Lu, *Polym. Adv. Technol.* **2020**, *31*, 1648.

[183] D. Zhao, M. Feng, L. Zhang, B. He, X. Chen, J. Sun, *Carbohydr. Polym.* **2021**, *256*, 117580.

[184] B. Ye, S. Zhang, R. Li, L. Li, L. Lu, C. Zhou, *Compos. Sci. Technol.* **2018**, *156*, 238.

[185] B. Zhang, J. He, M. Shi, Y. Liang, B. Guo, *Chem. Eng. J.* **2020**, *400*, 125994.

[186] T. Bai, S. Liu, F. Sun, A. Sinclair, L. Zhang, Q. Shao, S. Jiang, *Biomaterials* **2014**, *35*, 3926.

[187] Y. Lin, Z. Zeng, Y. Li, S. Sun, X. Liu, D. He, G. Li, *RSC Adv.* **2019**, *9*, 31806.

[188] X. Sun, S. He, Z. Qin, J. Li, F. Yao, *Compos. Commun.* **2021**, *26*, 100784.

[189] W. Zhang, H. Jiang, Z. Chang, W. Wu, G. Wu, R. Wu, J. Li, *J. Mater. Sci.* **2020**, *55*, 13543.

[190] C. Gao, Y. Gao, S. Wang, Y. Dong, Y. Wu, Y. Liu, C. Wang, *Eur. Polym. J.* **2022**, *175*, 111301.

[191] J. Ma, S. Wen, Z. Yue, *RSC Adv.* **2022**, *12*, 21512.

[192] C. Lu, Z. Ling, C. Wang, J. Wang, Q. Yong, F. Chu, *Compos. Part B Eng.* **2022**, *228*, 109428.

[193] E. Feng, J. Li, G. Zheng, X. Li, J. Wei, Z. Wu, X. Ma, Z. Yang, *Chem. Eng. J.* **2022**, *432*, 134406.

[194] F. Wang, K. Huang, Z. Xu, F. Shi, C. Chen, *Int. J. Biol. Macromol.* **2022**, *203*, 143.

[195] G. Newham, S. D. Evans, Z. Y. Ong, *J. Colloid Interface Sci.* **2022**, *617*, 224.

[196] Y. Liang, Y. Shen, H. Liang, *Mater. Today Commun.* **2022**, *30*, 103067.

[197] J. H. Hwang, J. Shin, J. Han, Y.-S. Choi, S. Park, Y. H. Kim, Y. S. Kim, H. S. Kang, D.-G. Kim, J.-C. Lee, *Adv. Intell. Syst.* **2022**, *4*, 2200051.

[198] X. Li, J. Wang, Y. Lin, Y. Cheng, W. Han, G. Yuan, H. Jia, *Colloids Surfaces A Physicochem. Eng. Asp.* **2022**, *635*, 128091.

[199] B. Singh, R. K. Khurana, B. Garg, S. Saini, R. Kaur, *Crit. Rev. Ther. Drug Carrier Syst.* **2017**, *34*, 209.

[200] S. Chatterjee, P. C. Hui, in *Hydrogels* (Eds.: L. Popa, M. V. Ghica, C.-E. Dinu-Pîrvu), IntechOpen, Rijeka, **2018**.

[201] S. Municoy, M. I. Álvarez Echazú, P. E. Antezana, J. M. Galdopórpora, C. Olivetti, A. M. Mebert, M. L. Foglia, M. V. Tuttolomondo, G. S. Alvarez, J. G. Hardy, M. F. Desimone, *Int. J. Mol. Sci.* **2020**, *21*, 1.

[202] F. Khan, M. Atif, M. Haseen, S. Kamal, M. S. Khan, S. Shahid, S. A. A. Nami, *J. Mater. Chem. B* **2022**, *10*, 170.

[203] N. Sood, A. Bhardwaj, S. Mehta, A. Mehta, *Drug Deliv.* **2016**, *23*, 758.

[204] H. M. El-Husseiny, E. A. Mady, L. Hamabe, A. Abugomaa, K. Shimada, T. Yoshida, T. Tanaka, A. Yokoi, M. Elbadawy, R. Tanaka, *Mater. Today Bio* **2022**, *13*, 100186.

[205] S. Guragain, B. P. Bastakoti, V. Malgras, K. Nakashima, Y. Yamauchi, *Chem. - A Eur. J.* **2015**, *21*, 13164.

[206] A. Sydney Gladman, E. A. Matsumoto, R. G. Nuzzo, L. Mahadevan, J. A. Lewis, *Nat. Mater.* **2016**, *15*, 413.

[207] Y. S. Kim, M. Liu, Y. Ishida, Y. Ebina, M. Osada, T. Sasaki, T. Hikima, M. Takata, T. Aida, *Nat. Mater.* **2015**, *14*, 1002.

[208] S. Wang, D. P. Maruri, J. M. Boothby, X. Lu, L. K. Rivera-Tarazona, V. D. Varner, T. H. Ware, *J. Mater. Chem. B* **2020**, *8*, 6988.

[209] A. Nojoomi, H. Arslan, K. Lee, K. Yum, *Nat. Commun.* **2018**, *9*, 1.

[210] M. Chau, K. J. De France, B. Kopera, V. R. Machado, S. Rosenfeldt, L. Reyes, K. J. W. Chan, S. Förster, E. D. Cranston, T. Hoare, E. Kumacheva, *Chem. Mater.* **2016**, *28*, 3406.

[211] H. Arslan, A. Nojoomi, J. Jeon, K. Yum, *Adv. Sci.* **2019**, *6*, 1800703.

[212] X. He, S. Wang, J. Zhou, D. Zhang, Y. Xue, X. Yang, L. Che, D. Li, S. Xiao, S. Liu, S. Y. Zheng, J. Yang, *ACS Appl. Mater. Interfaces* **2022**, *14*, 4579.

[213] S. Xiao, Y. Yang, M. Zhong, H. Chen, Y. Zhang, J. Yang, J. Zheng, **2017**, DOI 10.1021/acsami.7b04417.

[214] S. Xiao, M. Zhang, X. He, L. Huang, Y. Zhang, B. Ren, M. Zhong, Y. Chang, J. Yang, J. Zheng, *ACS Appl. Mater. Interfaces* **2018**, *10*, 21642.

[215] X. He, D. Zhang, J. Wu, Y. Wang, F. Chen, P. Fan, M. Zhong, S. Xiao, J. Yang, *ACS Appl. Mater. Interfaces* **2019**, *11*, 25417.

[216] L. Wang, Y. Jian, X. Le, W. Lu, C. Ma, J. Zhang, Y. Huang, C.-F. Huang, T. Chen, *Chem. Commun.* **2018**, *54*, 1229.

[217] Q. Zhao, Y. Liang, L. Ren, Z. Yu, Z. Zhang, F. Qiu, L. Ren, *J. Mater. Chem. B* **2018**, *6*, 1260.

[218] J. Zheng, P. Xiao, X. Le, W. Lu, P. Théato, C. Ma, B. Du, J. Zhang, Y. Huang, T. Chen, *J. Mater. Chem. C* **2018**, *6*, 1320.

[219] A. Gevorkian, S. M. Morozova, S. Kheiri, N. Khuu, H. Chen, E. Young, N. Yan, E. Kumacheva, **2021**, *2010743*, 1.

[220] Q. Lu, S. Bai, Z. Ding, H. Guo, Z. Shao, H. Zhu, D. L. Kaplan, **2016**, 1.

[221] M. Chen, J. Zhu, G. Qi, C. He, H. Wang, *Mater. Lett.* **2012**, *89*, 104.

[222] P. Chen, Q. Ruan, R. Nasseri, H. Zhang, X. Xi, H. Xia, G. Xu, Q. Xie, C. Yi, Z. M. Sun, H. Shahsavan, W. Zhang, *Adv. Sci.* **2022**, *9*, 1.

[223] M. Liu, Y. Ishida, Y. Ebina, T. Sasaki, T. Hikima, M. Takata, T. Aida, *Nature* **2015**, *517*, 68.

[224] Q. Zhao, Y. Liang, L. Ren, Z. Yu, Z. Zhang, F. Qiu, L. Ren, *J. Mater. Chem. B* **2018**, *6*, 1260.

[225] A. Lassoued, B. Dkhil, A. Gadri, S. Ammar, *Results Phys.* **2017**, *7*, 3007.

[226] Y. V. Kolen'Ko, M. Bañobre-López, C. Rodríguez-Abreu, E. Carbó-Argibay, A. Sailsman, Y. Piñeiro-Redondo, M. F. Cerqueira, D. Y. Petrovykh, K. Kovnir, O. I. Lebedev, J. Rivas, *J. Phys. Chem. C* **2014**, *118*, 8691.

[227] L. Cao, Z. Cheng, M. Yan, Y. Chen, *Chem. Eng. J.* **2019**, *363*, 203.

[228] R. Nasseri, K. C. Tam, *ACS Sustain. Chem. Eng.* **2021**, *9*, 10424.

[229] R. Nasseri, K. C. Tam, *ACS Appl. Polym. Mater.* **2022**, *4*, 2674.

[230] J. Wang, Q. Cheng, S. Feng, L. Zhang, C. Chang, *J. Mater. Chem. C* **2021**, *9*, 6344.

[231] Z. Lei, P. Wu, *ACS Nano* **2018**, *12*, 12860.

[232] Z. Li, B. Hao, Y. Tang, H. Li, T. C. Lee, A. Feng, L. Zhang, S. H. Thang, *Eur. Polym. J.* **2020**, *132*, 109704.

[233] S. Xiao, J. Yang, **2019**, DOI 10.1021/acsami.9b06691.

[234] Z. Li, B. Hao, Y. Tang, H. Li, T.-C. Lee, A. Feng, L. Zhang, S. H. Thang, *Eur. Polym. J.* **2020**, *132*, 109704.

[235] P. Jain, H. C. Hung, B. Li, J. Ma, D. Dong, X. Lin, A. Sinclair, P. Zhang, M. B. O'Kelly, L. Niu, S. Jiang, *Langmuir* **2019**, *35*, 1864.

[236] I. Erukhimovich, M. O. de la Cruz, **2004**, 1430.

[237] M. Chau, K. J. De France, B. Kopera, V. R. Machado, S. Rosenfeldt, L. Reyes, K. J. W. Chan, S. Förster, E. D. Cranston, T. Hoare, E. Kumacheva, *Chem. Mater.* **2016**, *28*, 3406.

[238] A. Kumar, R. Rajamanickam, J. Hazra, N. R. Mahapatra, P. Ghosh, *ACS Appl. Mater. Interfaces* **2022**, *14*, 56321.

[239] H. Liu, C. Xiong, Z. Tao, Y. Fan, X. Tang, H. Yang, *RSC Adv.* **2015**, *5*, 33083.

[240] Y. Sun, S. Lu, Q. Li, Y. Ren, Y. Ding, H. Wu, X. He, Y. Shang, *Eur. Polym. J.* **2020**, *133*, 109761.

[241] J. Zhang, N. A. Peppas, *Macromolecules* **2000**, *33*, 102.

[242] F. Çalılı, P. Kaner, G. Aro, A. Asatekin, P. Z. Çulfaz-Emecen, *React. Funct. Polym.* **2020**, *156*, 104738.

[243] Z. Li, B. Hao, Y. Tang, H. Li, T. C. Lee, A. Feng, L. Zhang, S. H. Thang, *Eur. Polym. J.* **2020**, *132*, 109704.

[244] T. Xiang, T. Lu, W. F. Zhao, C. S. Zhao, *Langmuir* **2019**, *35*, 1146.

[245] R. Nasseri, C. P. Deutschman, L. Han, M. A. Pope, K. C. Tam, *Mater. Today Adv.* **2020**, *5*, 100055.

[246] E. Prince, M. Alizadehgiashi, M. Campbell, N. Khuu, A. Albulescu, K. De France, D. Ratkov, Y. Li, T. Hoare, E. Kumacheva, *Biomacromolecules* **2018**, *19*, 1276.

[247] H. Bai, A. Polini, B. Delattre, A. P. Tomsia, *Chem. Mater.* **2013**, *25*, 4551.

[248] R. Dai, L. Meng, Q. Fu, S. Hao, J. Yang, *ACS Sustain. Chem. Eng.* **2021**, *9*, 12274.

[249] M. T. McClendon, S. I. Stupp, *Biomaterials* **2012**, *33*, 5713.

[250] Z. Zhu, Y. Li, H. Xu, X. Peng, Y.-N. Chen, C. Shang, Q. Zhang, J. Liu, H. Wang, *ACS Appl. Mater. Interfaces* **2016**, *8*, 15637.

[251] K. M. O. Håkansson, A. B. Fall, F. Lundell, S. Yu, C. Krywka, S. V Roth, G. Santoro, M. Kvick, L. Prahl Wittberg, L. Wågberg, L. D. Söderberg, *Nat. Commun.* **2014**, *5*, 4018.

[252] A. Gevorkian, S. M. Morozova, S. Kheiri, N. Khuu, H. Chen, E. Young, N. Yan, E. Kumacheva, *Adv. Funct. Mater.* **2021**, *31*, 2010743.

[253] Q. Zhu, Y. Jin, W. Wang, G. Sun, D. Wang, *ACS Appl. Mater. Interfaces* **2019**, *11*, 1440.

[254] O. Fourmann, M. K. Hausmann, A. Neels, M. Schubert, G. Nyström, T. Zimmermann, G. Siqueira, *Carbohydr. Polym.* **2021**, *259*, 1.

[255] C. E. Sing, S. L. Perry, *Soft Matter* **2020**, *16*, 2885.

[256] K. J. De France, K. G. Yager, T. Hoare, E. D. Cranston, *Langmuir* **2016**, *32*, 7564.

[257] P. M. Pardeshi, A. A. Mungray, *Environ. Technol. Innov.* **2021**, *23*, 101669.

[258] T. Xu, L. Zhang, B. Song, X. Bai, Z. Huang, X. Bu, T. Chen, H. Fu, P. Guo, *J. Colloid Interface Sci.* **2022**, *620*, 14.

[259] L. S. Lim, N. A. Rosli, I. Ahmad, A. Mat Lazim, M. C. I. Mohd Amin, *Nanomaterials* **2017**, *7*, DOI 10.3390/nano7110399.

[260] R. Nasseri, K. C. Tam, *ACS Sustain. Chem. Eng.* **2021**, *9*, 10424.

[261] D. L. Taylor, M. in het Panhuis, *Adv. Mater.* **2016**, *28*, 9060.

[262] V. Yesilyurt, M. J. Webber, E. A. Appel, C. Godwin, R. Langer, D. G. Anderson, *Adv. Mater.* **2016**, *28*, 86.

[263] Y. Zhang, K. Chen, Y. Li, J. Lan, B. Yan, L. Shi, R. Ran, *ACS Appl. Mater. Interfaces* **2019**, *11*, 47350.

[264] M. S. Oh, Y. S. Song, C. Kim, J. Kim, J. B. You, T. S. Kim, C. S. Lee, S. G. Im, *ACS Appl. Mater. Interfaces* **2016**, *8*, 8782.

[265] G. Stoychev, L. Guiducci, S. Turcaud, J. W. C. Dunlop, L. Ionov, *Adv. Funct. Mater.* **2016**, *26*, 7733.

[266] J. Kim, C. Kim, Y. S. Song, S. G. Jeong, T. S. Kim, C. S. Lee, *Chem. Eng. J.* **2017**, *321*, 384.

[267] Z. Chen, G. Huang, I. Trase, X. Han, Y. Mei, *Phys. Rev. Appl.* **2016**, *5*, 1.

[268] T. van Manen, S. Janbaz, A. A. Zadpoor, *Mater. Today* **2018**, *21*, 144.

[269] Q. Guo, A. K. Mehta, M. A. Grover, W. Chen, D. G. Lynn, Z. Chen, *Appl. Phys. Lett.* **2014**, *104*, 211901.

[270] Z. Chen, C. Majidi, D. J. Srolovitz, M. Haataja, *Appl. Phys. Lett.* **2011**, *98*, 11906.

[271] S. Armon, E. Efrati, R. Kupferman, E. Sharon, *Science (80-.).* **2011**, *333*, 1726.

[272] A. Gevorkian, S. M. Morozova, S. Kheiri, N. Khuu, H. Chen, E. Young, N. Yan, E. Kumacheva, *Adv. Funct. Mater.* **2021**, *31*, 1.

[273] Y. Ahn, H. Lee, D. Lee, Y. Lee, *ACS Appl. Mater. Interfaces* **2014**, *6*, 18401.

[274] T. Xiang, T. Lu, W.-F. Zhao, C.-S. Zhao, *Langmuir* **2019**, *35*, 1146.

[275] T. Bai, S. Liu, F. Sun, A. Sinclair, L. Zhang, Q. Shao, S. Jiang, *Biomaterials* **2014**, *35*, 3926.

[276] P. Cabanach, A. Pena-Francesch, D. Sheehan, U. Bozuyuk, O. Yasa, S. Borros, M. Sitti, *Adv. Mater.* **2020**, *32*, 2070312.

[277] Y. Sun, S. Lu, Q. Li, Y. Ren, Y. Ding, H. Wu, X. He, Y. Shang, *Eur. Polym. J.* **2020**, *133*, 109761.

[278] X. Sun, S. He, Z. Qin, J. Li, F. Yao, *Compos. Commun.* **2021**, *26*, 100784.

[279] T. Xiang, T. Lu, W.-F. Zhao, C.-S. Zhao, *New J. Chem.* **2018**, *42*, 5323.

[280] S. Hashmi, S. Nadeem, A. García-Peñas, R. Ahmed, A. Zahoor, M. Vatankhah-Varnoosfaderani, F. J. Stadler, *Macromol. Chem. Phys.* **2022**, *223*, 2100348.

[281] L. Ni, J. Meng, G. M. Geise, Y. Zhang, J. Zhou, *J. Memb. Sci.* **2015**, *491*, 73.

[282] S. Aleid, M. Wu, R. Li, W. Wang, C. Zhang, L. Zhang, P. Wang, *ACS Mater. Lett.* **2022**, *4*, 511.

[283] S. Dutta, D. Cohn, *J. Mater. Chem. B* **2017**, *5*, 9514.

[284] T. Zhang, M. S. Silverstein, *Polym. Chem.* **2018**, *9*, 3479.

[285] S. Dutta, D. Dey, D. Dhara, *J. Appl. Polym. Sci.* **2014**, *131*, 1.

[286] T. Ono, T. Sugimoto, S. Shinkai, K. Sada, *Nat. Mater.* **2007**, *6*, 429.

[287] Y. Cheng, K. Ren, D. Yang, J. Wei, *Sensors Actuators, B Chem.* **2018**, *255*, 3117.

[288] X. Peng, H. Wang, *J. Polym. Sci. Part B Polym. Phys.* **2018**, *56*, 1314.

[289] J. Yang, W. Yang, X. Wang, M. Dong, H. Liu, E. K. Wujcik, Q. Shao, S. Wu, T. Ding, Z. Guo, *Macromol. Chem. Phys.* **2019**, *220*, 1800567.

[290] X. He, D. Zhang, J. Wu, Y. Wang, F. Chen, P. Fan, M. Zhong, S. Xiao, J. Yang, *ACS Appl. Mater. Interfaces* **2019**, *11*, 25417.

[291] T. van Manen, S. Janbaz, A. A. Zadpoor, *Mater. Today* **2018**, *21*, 144.

Appendix A
Supplementary Information

Finite element simulations

The mechanical deformations of anisotropic hydrogels, shown in **Figure 4-7**, were modeled using the finite element software (COMSOL Multiphysics 6.0). The neo-Hookean hyperelastic model was used to model the swelling behavior of hydrogels, which is capable of describing the mechanical behavior of hydrogels in different regimes of large deformation. The hydrogel elastic modulus of E = 191 kPa was used for the anisotropic gels with an assumed Poisson's ratio of 0.3, typical in most hydrogel materials, with the calculated material density of 1120 kg/m^3. Although the neo-Hookean model is not capable of modeling the anisotropic elasticity of the hyperelastic material, it can lead to correct estimation when the elastic properties of the material in different directions are close to each other. When the elastic properties of hydrogels in different directions differ drastically, anisotropic hyperelastic models such as the Ogden model or Fung model can be used. Both models are more complex than the neo-Hookean model and require more information about the material's properties.

The swelling strain was included in the total strain as $\boldsymbol{\varepsilon^T = \varepsilon^e + \varepsilon^s}$, where $\boldsymbol{\varepsilon^e}$ is the elastic strain tensor and $\boldsymbol{\varepsilon^s}$ is the swelling strain tensor, given by:[206]

$$\boldsymbol{\varepsilon^s} = \begin{bmatrix} \boldsymbol{\alpha_{\parallel}} & \mathbf{0} \\ \mathbf{0} & \boldsymbol{\alpha_{\perp}} \end{bmatrix}$$

where $\boldsymbol{\alpha_{\parallel}}$ and $\boldsymbol{\alpha_{\perp}}$ are swelling in parallel and perpendicular to the alignment direction (adopted from **Figure 4-6d**). The swelling strains were increased by small increments in the simulations to achieve solution convergence.

Cell Viability

Fibroblast cells (NIH/3T3) were cultured in a 37 °C, 5% CO_2 humidified incubator using Dulbecco's modified Eagle's medium (DMEM) supplemented with 10% (v/v) FBS and 1% (v/v) penicillin/streptomycin. The cytotoxicity of the hydrogels was evaluated using a Live/Dead assay kit (Invitrogen). Circular films of different hydrogels were prepared and washed with 1 wt% NaCl solution, DI water, and ethanol for 7 days to remove unreacted materials. The prepared films were also sterilized via UV exposure for 2 hours. Cells were cultured in 6-well plates at an initial density of 5x10^4 cells

per well and incubated with sterilized films for 5 days. On days one, three, and five, cells were stained with Calcein AM (0.5 μL/mL in PBS) and ethidium homodimer-1 (2 μL/mL in PBS) to visualize live and dead cells, respectively, according to the manufacturer's protocol. Stained samples were imaged using a Zeiss LSM 700 confocal microscope (Carl Zeiss AG, Germany).